Wall turbulence over acoustic liners

An aerodynamic perspective

Shahzad, H.

DOI
10.4233/uuid:f241401a-5468-473f-8587-ccd04a11272b

Publication date
2026

Document Version
Final published version

Citation (APA)
Shahzad, H. (2026). *Wall turbulence over acoustic liners: An aerodynamic perspective*. [Dissertation (TU Delft), Delft University of Technology]. https://doi.org/10.4233/uuid:f241401a-5468-473f-8587-ccd04a11272b

WALL TURBULENCE OVER ACOUSTIC LINERS: AN AERODYNAMIC PERSPECTIVE

HARIS SHAHZAD

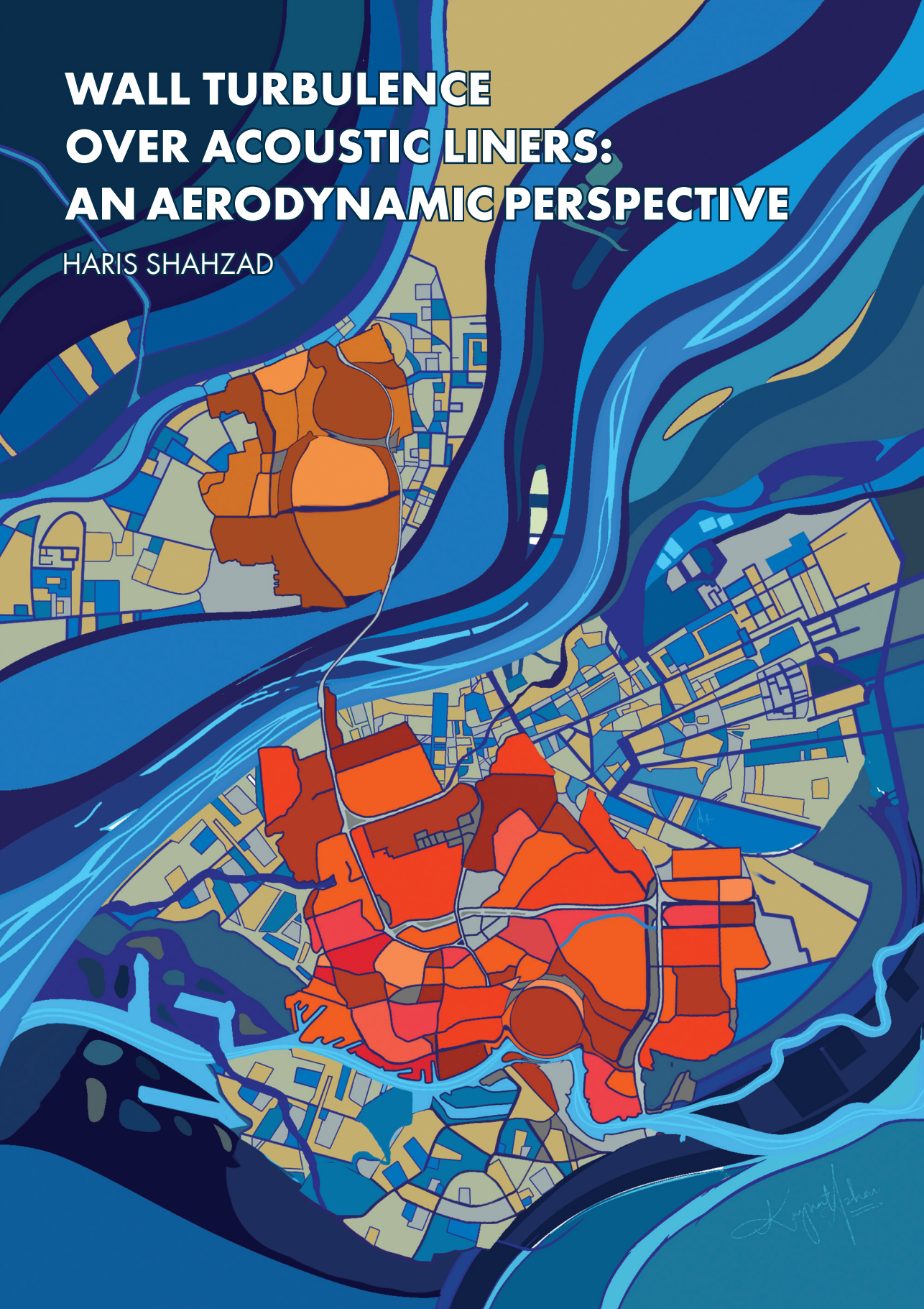

Wall turbulence over acoustic liners: An aerodynamic perspective

Wall turbulence over acoustic liners: An aerodynamic perspective

Dissertation

for the purpose of obtaining the degree of doctor
at Delft University of Technology,
by the authority of the Rector Magnificus prof. dr. ir. T.H.J.J. van der Hagen,
Chair of the Board for Doctorates,
to be defended publicly on
Wednesday 14 January 2026 at 10:00 hours.

by

Haris SHAHZAD

Master of Science in Aerospace Engineering,
Delft University of Technology, Nederland,
born in Rawalpindi, Pakistan.

This dissertation has been approved by the promotors.

Composition of the doctoral committee:

Rector Magnificus,	voorzitter
Prof. Dr.-Ing. habil. S. Hickel,	promotor, Delft University of Technology
Dr. D. Modesti	copromotor, Delft University of Technology/ Gran Sasso Science Institute, Italy
Independent members:	
Prof. Dr. Ir. B.J. Boersma,	Delft University of Technology
Prof. Dr. F. Avallone,	Politecnico di Torino, Italy
Prof. Dr. S. Bagheri,	KTH Royal Institute of Technology, Sweden
Prof. Dr. B. Ganapathisubramani	University of Southampton, UK
Reserve member:	
Prof. Dr. M. Kotsonis	Delft University of Technology

Keywords: Acoustic liners, Wall turbulence, Permeable walls, Forchheimer permeability, Compressible turbulence, Direct numerical simulation.

Printed by:

Cover: Designed by Kaynat Azhar and Aimen Abbas

ISBN …

An electronic version of this dissertation is available at
`http://repository.tudelft.nl/`.

You miss 100% of the shots you don't take -Wayne Gretzky.

Michael Scott

Contents

Summary

This dissertation studies the aerodynamic behavior of turbulent flow over acoustic liners—permeable surfaces installed inside aircraft engine nacelles to reduce noise. While these liners are highly effective at attenuating sound, they are also known to increase drag. Most prior research has focused on their acoustic performance, often simplifying or overlooking their aerodynamic impact. This work shifts that focus, using fully resolved, high-fidelity direct numerical simulations (DNS) to study flow over realistic liner geometries. Unlike many earlier studies that rely on simplifying assumptions such as impedance boundary models, this study avoids those simplifications by directly resolving the geometry of the acoustic liners.

The study explores key questions: which geometric features of acoustic liners most influence their aerodynamic behavior, how do these surfaces compare to traditional rough walls surfaces, and what additional effects are introduced by acoustic excitation. Although acoustic liners are flush with the surface and lack protrusions, we find that they still behave like canonical rough surfaces due to their permeability. The aerodynamic impact is governed by the non-linear Forchheimer permeability—a parameter that we show is closely linked to strong wall-normal velocity fluctuations in the near-wall region. These fluctuations are the primary driver of the drag penalty: the higher the wall-normal velocity fluctutations, the higher is the drag penalty compared to the reference smooth wall case. Importantly, the findings show that by limiting these wall-normal motions through geometric modifications—such as tapered orifices, or alternative shapes like elliptical orifices—it is possible to reduce drag. Tapered holes in particular show potential, as they decrease permeability without significantly affecting sound absorption. More aggressive changes, like parallel slots, tend to degrade acoustic performance, highlighting a necessary trade-off. However, certain designs, such as perpendicular slots, appear to offer a favorable balance.

Using the first fully resolved spatially developing turbulent boundary layer simulation over an acoustic liner array, this dissertation further shows that, for the conditions studied, acoustic excitation—modeled as a planar upstream-propagating monochromatic wave—does not significantly affect aerodynamic behavior. However, this does not rule out more complex interactions under realistic engine conditions, where acoustic fields are broadband and multidirectional. Limitations in the numerical setup, particularly in acoustic modeling, mean that the full impact of sound waves remains an open question.

The work also touches on broadband acoustic liner geometries, which are becoming increasingly relevant. These designs are more permeable—not just in the wall-normal direction—but across multiple directions. Higher permeability typically correlates with higher drag, and this trend holds for acoustic liners as well. Still, the study shows that with careful design, broadband liners can be engineered to avoid additional drag penalties, achieving comparable aerodynamic performance to conventional designs.

In summary, this dissertation offers a detailed aerodynamic analysis of flow over acoustic liners, explaining the mechanisms behind drag increase and establishing the

central role of permeability. It shows that aerodynamic optimization is possible without compromising acoustic effectiveness and highlights the need for fully resolved simulations when studying such complex surfaces. The findings lay the groundwork for the design of next-generation acoustic liners that better balance noise control and aerodynamic efficiency.

Samenvatting

Dit proefschrift bestudeert het aerodynamische gedrag van turbulente stroming over akoestische liners—doorlatende oppervlakken die in de motorbehuizing van vliegtuigen worden geplaatst om geluid te reduceren. Hoewel deze liners zeer effectief zijn in geluidsdemping, is ook bekend dat zij de weerstand (drag) verhogen. De meeste eerdere onderzoeken richtten zich primair op de akoestische prestaties, vaak met vereenvoudigingen of zonder aandacht voor het aerodynamische effect. Dit werk verschuift de focus door gebruik te maken van volledig opgeloste, hoge-resolutie directe numerieke simulaties (DNS) om de stroming over realistische linergeometrieën te bestuderen. In tegenstelling tot veel eerdere studies, waarin vereenvoudigende aannames zoals impedantieboundarymodellen gebruiken, vermijdt deze studie dergelijke simplificaties door de geometrie van de akoestische liners direct te resolveren.

De studie onderzoekt enkele kernvragen: welke geometrische kenmerken van akoestische liners hebben de grootste invloed op hun aerodynamisch gedrag, hoe verhouden deze oppervlakken zich tot traditionele ruwe oppervlakken, en welke aanvullende effecten worden geïntroduceerd door akoestische excitatie. Hoewel akoestische liners vlak zijn en geen uitstekende structuren hebben, blijkt uit onze resultaten dat ze zich door hun doorlatendheid nog steeds gedragen als klassieke ruwe oppervlakken. Het aerodynamische effect wordt voornamelijk bepaald door de niet-lineaire Forchheimer-doorlatendheid—aangetoond als sterk gerelateerd aan de wandnormale snelheidsfluctuaties in de nabij-wandzone. Deze fluctuaties vormen de belangrijkste oorzaak van de toename van de weerstand: hoe groter de wandnormale fluctuaties, hoe hoger de weerstand ten opzichte van een referentie gladwandcase. De resultaten tonen aan dat het beperken van deze wandnormale bewegingen door geometrische aanpassingen—zoals taps toelopende openingen of alternatieve vormen zoals elliptische openingen-kan leiden tot een vermindering van de weerstand. Vooral taps toelopende gaten tonen potentieel, omdat ze de doorlatendheid verminderen zonder het geluidabsorberend vermogen significant aan te tasten. Meer ingrijpende wijzigingen, zoals parallelle sleuven, leiden vaak tot een verslechtering van de akoestische prestaties, wat een noodzakelijke afweging benadrukt. Sommige ontwerpen, zoals loodrechte sleuven, lijken echter een gunstig compromis te bieden.

Door gebruik te maken van de eerste volledig opgeloste, ruimtelijk ontwikkelende turbulente grenslaag-simulatie over een array van akoestische liners, toont dit proefschrift bovendien aan dat, voor de bestudeerde condities, akoestische excitatie—gemodelleerd als een vlakke, stroomopwaarts voortplantende monofrequente golf—geen significante invloed heeft op het aerodynamisch gedrag. Dit sluit echter niet uit dat complexere interacties kunnen optreden onder realistische motorcondities, waarin de akoestische velden breedbandig en multidirectioneel zijn. Beperkingen in de numerieke opzet, met name in de akoestische modellering, betekenen dat het volledige effect van geluidsgolven vooralsnog een open vraag blijft.

Het werk behandelt tevens breedbandige akoestische linergeometrieën, die steeds relevanter worden. Deze ontwerpen zijn doorgaans doorlatender—niet alleen in de wandnormale richting-maar in meerdere richtingen. Een hogere doorlatendheid correleert meestal met hogere weerstand, en deze trend geldt ook voor akoestische liners. Toch toont de studie aan dat, met zorgvuldige ontwerpkeuzes, breedbandige liners zo kunnen worden geconstrueerd dat extra weerstand wordt vermeden, terwijl de aerodynamische prestaties vergelijkbaar blijven met conventionele ontwerpen.

Samenvattend biedt dit proefschrift een gedetailleerde aerodynamische analyse van stroming over akoestische liners, legt het de mechanismen achter de toename van weerstand uit en benadrukt het centrale belang van doorlatendheid. Het toont aan dat aerodynamische optimalisatie mogelijk is zonder concessies te doen aan de akoestische effectiviteit en onderstreept de noodzaak van volledig opgeloste simulaties bij het bestuderen van dergelijke complexe oppervlakken. De bevindingen vormen een basis voor het ontwerp van volgende-generatie akoestische liners die een betere balans bieden tussen geluidsreductie en aerodynamische efficiëntie.

Acknowledgments

While the cover and title page may suggest that this thesis was a purely solitary endeavor, this accomplishment is, in reality, a result of the collective support of my family and the community I built here in Delft. Had this journey relied solely on my own capacity, I doubt I would have reached this defense. I am here today not because I am, by any definition of the word, capable, but because I was incredibly fortunate to be surrounded by people who, knowingly or unknowingly, professionally or personally, offered the essential support, patience, and guidance that sustained this work. This thesis is truly a product of their faith and assistance.

I would like to express my deepest gratitude to my parents, whose unconditional love and encouragement have been the foundation of my success. I vividly remember receiving my acceptance to the Aerodynamics Master's program at TU Delft in January 2018; despite the significant financial commitment, my parents never once hesitated. My father's only concern was whether this was my dream, and that was enough for him. While I lost my grandparents during my PhD, I continue to carry their unwavering belief with me. My heartfelt thanks also go to my brother and sister for being my lifelong confidants. Additionally, I am profoundly grateful to Alia Auntie, Zubair Uncle, and Ahmad for their love, and to my family in the Netherlands—Shirin Auntie and JP Uncle—for their constant support and for always making me feel at home.

My deepest and most profound gratitude belongs to my wife, Aiman. You have not only lived through this entire doctoral journey with me but have shouldered far more of its burden than any acknowledgment could ever capture. Thank you for being so patient with me, for all the late nights, your unwavering belief in me and thank you for being my hype-man. Thank you for all the illustrations you made and all the posters you made. Some of the illustrations you made were so good that I see them everywhere now: being used in posters, conference papers and journal papers to introduce the work, with many people passing it off as their own. This achievement is as much yours as it is mine. I would also like to thank Bilal for had he not made an appearance, I might not have found the motivation to finally graduate.

I would also like to extend my gratitude to the two greatest supervisors an aspiring PhD candidate could ask for: Davide and Stefan. Stefan's CFD course was amongst the first lectures I attended here in Delft and they hold a special place in my heart. He subsequently supervised my Master's thesis and I blame Marios, Stefan and how much I enjoyed working with them during my master thesis, that drove me towards the insane idea that I could possibly do a PhD. I still remember the day towards the end of my master thesis when Stefan took me to Davide's office and told him that I would be a good candidate for his PhD position. Stefan's belief in my abilities has been a cornerstone of my academic development and he has been my mentor and a source of inspiration for me. Despite being one of the most brilliant people I know, he possesses the rare quality of making his students feel valued. Thank you for always fostering an environment where my perspective mattered,

and I am particularly grateful for your patience in listening to my imperfect, often just straight up stupid, ideas. I deeply appreciate the encouragement you provided, which made those most challenging periods of my PhD manageable.

Equally deserving of my deepest gratitude is Davide. On paper he was my supervisor but really he was a friend and a confidant who I could share my struggles with and I knew he would understand. Thank you for offering me this PhD opportunity in the first place. If I regret leaving the academia, its only because I loved working with you these past few years and would have loved to continue to do so. You believed in me, often much more than I believed in myself and you were always available, day or night. Thank you for helping out with all the last minute revisions, proofreading my careless work, knowing I need a bit of a push sometimes, and just being an overall great supervisor. My PhD journey was tough, both mentally and physically, and I am eternally grateful that you were so understanding. Thank you for your support and for always having my best interest at heart. I am also grateful that you realised that leaving when I did and moving on was the right thing for me. That you supported my decision is a demonstration of your unparalleled care and mentorship. I hold a deep, profound respect for you.

My PhD journey would have been incomplete without my fellow PhD colleagues. Without exaggeration, the time I spent with them has been some of the most fun I have ever had. A large part of that joy came from Ata, Tyler, and Thomas—the three people around whom I could unapologetically be my most crude, brash, and dark self. Ata is one of my oldest friends here in Delft, and despite our long-standing love–hate relationship, our ~~b~~romance has only continued to flourish over the years. Tyler is living proof that not all patriotic Republican voters are terrible people, and I sincerely hope that, many years from now, you will still text me out of the blue to say you have made a restaurant reservation for the two of us—I will be there. Thank you, Thomas, for being the posh and proper one and for keeping me (somewhat) in check. Wandering the streets of Rome with you remains one of the highlights of the past four years.

From the moment I joined the HSL, I felt welcomed and I owe that to my colleagues at the time. Thank you Ale and Luis for not only welcoming me when I joined but being a constant source of support over the years. I never hesitated to walk into your office if I had a question and I am glad that you two are doing well. Thank you Varun, Gabriel and Edo for making the HSL a cheerful and nice place to work even though I joined mid-Corona. Thank you Christoph for listening to my rants and complaints. Thank you Constantin for leaving behind a legacy of complaining that I tried to keep up after you left. Thank you Jordi (you were still in HSL when I joined) for being an amazing supervisor, a great friend and someone I can look up to.

The people who have joined HSL over the years have also been amazing. Thank you Jane for being the greatest "desk-neighbor" I could have asked for and being the only person who I could relate to. Thank you Wencan for being one of the nicest sweetest people I have met. Thank you Luuk for gezellig christmas dinners at your place, the coffee talks and the overall positivity you brought to the lab. Thank you Michele for sharing my frustrations about STREAmS, being the person who understood best my work and the effort you put in to stay in contact after leaving. Thank you Max for the enthusiasm you brought about your work to the group. Thank you Adrian for the time we spent in Boekelo and for being the voice of rhyme and reason in the lab. Thank you Suyash for bearing my obnoxious

self during board games. Despite being the smartest among us, your humility makes you someone I deeply admire. Thank you Kherlen for the interesting conversations, the way you brought everyone together with your energy and the time you beat Luuk with a stick, the memory of which is ingrained in my mind no matter how hard I try to forget. Thank you Renzhi for being really funny in chinese. Thank you Abdoo for the coffee and opening my eyes to what I was missing. I bought my own espresso machine because of you.

Beyond these wonderful colleagues, I am also deeply grateful to the other lab mates, Giulio, Giulia, Beto, Theo, Babak, Marina, Sven and Parisa, and the professors who have been a part of this journey. Thank you, Anh Khoa, for the lunch conversations and for making me realize that I am not alone in the lab when it comes to unconventional, mostly controversial ideas. Thank you, Richard, for your support and for our conversation in Barcelona during ETMM—that talk helped during a difficult phase in my life.

I would like to extend my gratitude to my community outside the lab. Thank you Ozaif and Ajlal for helping me settle down here in Delft. It was through you two that I built my community here and for that, I am deeply indebted. Thank you Samad, Muneeb, Hassan and Hamza for all the time we have spent together the past couple years, and here is to hoping that Samad never wins our fantasy league so we have an excuse for keeping it going despite the mental trauma that it inflicts upon us every week. I would have left a long time ago had it not been for all of you. Thank you to the rest of the weekend squad: Kaynat, Hafsah, Hafsa and Sana. Thank you Mohsan and Aitazaz for effectively baby-sitting me for long periods of time. Thank you all for being the closest thing to a family I have here.

Finally, thank you Martijn for the jokes and the taunts that motivated me enough to finish my PhD.

Haris
Eindhoven, December 2025

1

Introduction

1

1.1 Acoustic liners: A brief overview

Aircraft design is a compromise with many competing constraints. Although aircrafts are designed to maximise, as much as possible, the lift-to-drag ratio, aerodynamically optimised geometries that reduce drag may not necessarily be structurally sound, acoustically optimised, economically feasible or even possible to manufacture and maintain. Acoustic liners are a prime example. Acoustic liners are small passive devices (i.e. no energy input required) that are installed on the inside of an engine nacelle. They are panels with a sandwich structure, consisting of a honeycomb core, bounded by a perforated facesheet and a solid backplate , and cover the nacelle inner surface, both in front of the fan and in the by-pass duct (see figures 1.1 and 1.2). Acoustic liners are the state of the art in engine noise reduction. Unfortunately, however, they increase total aircraft drag and reduce fuel efficiency.

Acoustic liners are based on the idea of a Helmholtz resonator. Helmholtz resonators are acoustic resonators that consist of a large cavity with a small opening, see figure 1.1. Helmholtz resonators exhibit a resonant frequency that is a function of their geometry/dimensions,

$$\omega_r = c\frac{\sqrt{A_o}}{t_o V_c}, \tag{1.1}$$

where ω_r is the angular resonance frequency, c is the speed of sound, A_o is the cross-sectional area of the opening/orifice, t_o is the facesheet thickness, and V_c is the volume of the cavity of the resonator. Helmholtz resonators are extensively used in automotive applications to reduce noise from a car's exhaust and as acoustic liners in engine nacelles.

Acoustic liners are a large array of Helmholtz resonators. The honeycomb core acts as a large cavity and the perforated plate provides orifices for the cavities. Acoustic liners can theoretically absorb all incoming sound if the resonant frequency of the liner is tuned to the frequency of the incoming acoustic wave [1, 2, 3]. In realistic conditions, several studies have shown that acoustic liners reduce fan noise as much as 3–6 dB [4, 5]. Due to the passive nature of these devices, that they can be tuned to absorb any form of tonal noise, and the tightening noise regulations behind aircraft, acoustic liners are an essential

Figure 1.1: Turbofan engine of a civil aircraft with acoustic liners on the air intake..

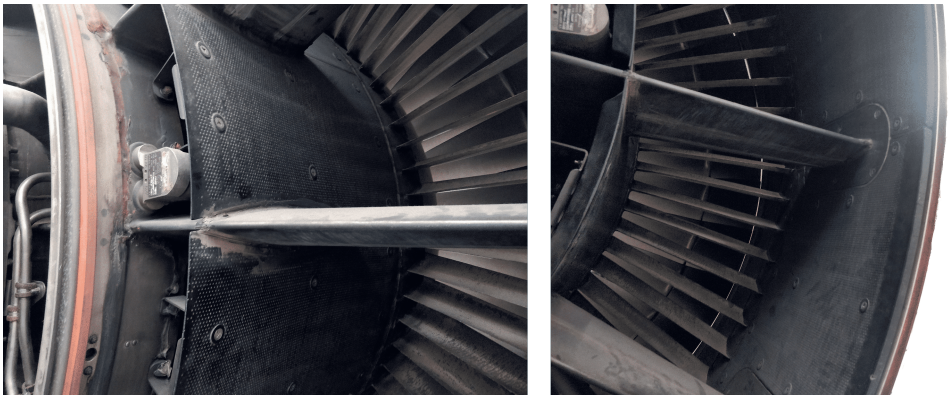

Figure 1.2: Acoustic liners around the fan of a turbofan engine.

part of aircraft engines. Unfortunately, though, acoustic liners act as a rough surface to the incoming turbulent flow and like most rough surfaces, acoustic liners have been known to increase drag [6, 7].

Due to their effectiveness in engine noise control, the added drag has largely been ignored and acoustic liners have primarily been studied and optimised from an acoustic perspective [8, 9]. Although the sound attenuation mechanism is well understood, the aerodynamic characteristics of these surfaces are less clear. Several authors agree that liners increase aerodynamic drag as compared to a hydraulically smooth wall [10, 11, 12]. However, it is very difficult and computationally expensive to faithfully reproduce the operating conditions of acoustic liners, whether experimentally or numerically. The studies that have looked into acoustic liners and their aerodynamic impact, therefore, are subject, either to experimental uncertainty or critical numerical assumptions that make the computational cost much more tractable, but reduce the accuracy of the predictions. As a result, at present, we lack a theory for the prediction of the aerodynamic drag over acoustic liners and there is a large discrepancy in the amount of drag increase, with some estimates being as high as 500% per plane area.

1.2 Objectives and achievements of this thesis

Although the flow over different rough surfaces has been studied extensively, acoustic liners are unique in that unlike canonical rough surfaces, they do not protrude into the flow. Instead, the facesheet perforations act as a permeable surface to the flow. Permeable surfaces interact differently compared to canonical rough surfaces. Our work represents the first ever high-fidelity fully resolved simulation of acoustic liner arrays, such that our simulations are not plagued by the critical modelling assumptions that prior work has relied on. With our work, we hope to highlight the influence of acoustic liners on turbulent flow and, therefore, provide a building block towards developing aerodynamically and acoustically optimised acoustic liners. We hope to provide a complete picture of how acoustic liners behave and of the flow dynamics of such surfaces. Based on our fully resolved simulations, we answer the following critical questions:

1. What is the percentage drag increase over acoustic liner-type surfaces?
2. Can acoustic liner surfaces be optimised aerodynamically while maintaining or improving their acoustic noise attenuation?
3. How do acoustic liners interact with a growing boundary layer?
4. What is the influence of external acoustic forcing on the interaction between acoustic liners and the background turbulent flow?

2

Flow over rough and permeable surfaces

The previous chapter gave an overview of acoustic liners, why they are important and why we wish to optimise them. The following chapter provides a more general introduction to rough and permeable surfaces and their relation to acoustic liners. We begin first by looking at canonical rough surfaces and what we know about them. We then explore how rough surfaces differ from permeable ones, and how acoustic liners fit into this comparison. Finally, we will touch on the latest research in acoustic liners.

2.1 Rough Wall-Bounded Turbulent Flow

Rough surfaces are ubiquitous in nature and no surface can be completely smooth. Small imperfections or undulations in a surface are a natural byproduct of manufacturing processes. Imperfections such as steps and gaps arise as a result of mismatch between panels that make up an aircraft. Such imperfections typically can be characterised by a length scale, for example the height of a step, the depth or width of a gap or the average height of randomly distributed roughness. Whether a surface is considered rough or smooth from a fluid mechanics perspective depends, then, upon how this characteristic roughness length scale compares to the length scales of the flow. If the relevant roughness length scale is much smaller than the relevant flow length scale, the roughness is imperceptible to the flow and the flow behaves as if it was interacting with a smooth wall. The larger the relevant roughness length scale with respect to the flow length scales, the more profound is the influence of the roughness on the flow. In that regards, roughness, at least from a fluid mechanics perspective, is a property of the flow and not of the surface.

So omnipresent is the nature of rough surfaces, that their influence on wall-bounded flows has been an active area of research for a very long time, and continues to be so as different roughness topographies interact differently with the flow. The effort, therefore, is to understand how different roughness geometries, common in different applications, interact with the flow and to either maximise possible benefits of rough surfaces such as enhanced heat transfer or acoustic noise dissipation or minimise the detrimental impacts of roughness, such as the likely increase of skin friction.

The increased drag due to most rough surfaces is a well-known phenomena, dating back to the seminal work of Nikuradse [13] and Colebrook [14], with their data consolidated by Moody [15] into the Moody diagram. The Moody diagram, see figure 2.1, correlates the head loss, or pressure loss, represented by the non-dimensional friction factor f, required to force a particular mass flow rate, represented by the non-dimensional Reynolds number based on the pipe diameter, Re_D, through a pipe, at a range of roughness heights, k/D, where k is the roughness height and D is the diameter of the pipe. Although the Moody diagram is based on experiments of pipe flows, the results are equally valid for other wall-bounded turbulent flows such as channel flows and boundary layer flows. Together with the work of Nikuradse [13] and Colebrook [14], the Moody diagram has formed the basis for further research into wall-bounded turbulence. The initial work of Nikuradse [13], Colebrook [14] and Moody [15] focused primarily on sand-grain type roughness. Since then, a very large parameter space of roughness geometries, covering regularly shaped [16], irregularly shaped [17], streamwise invariant [18], spanwise invariant [19], impermeable [20], permeable [21], have been studied but the primary observations one can make from the Moody chart, still, by and large, hold true:

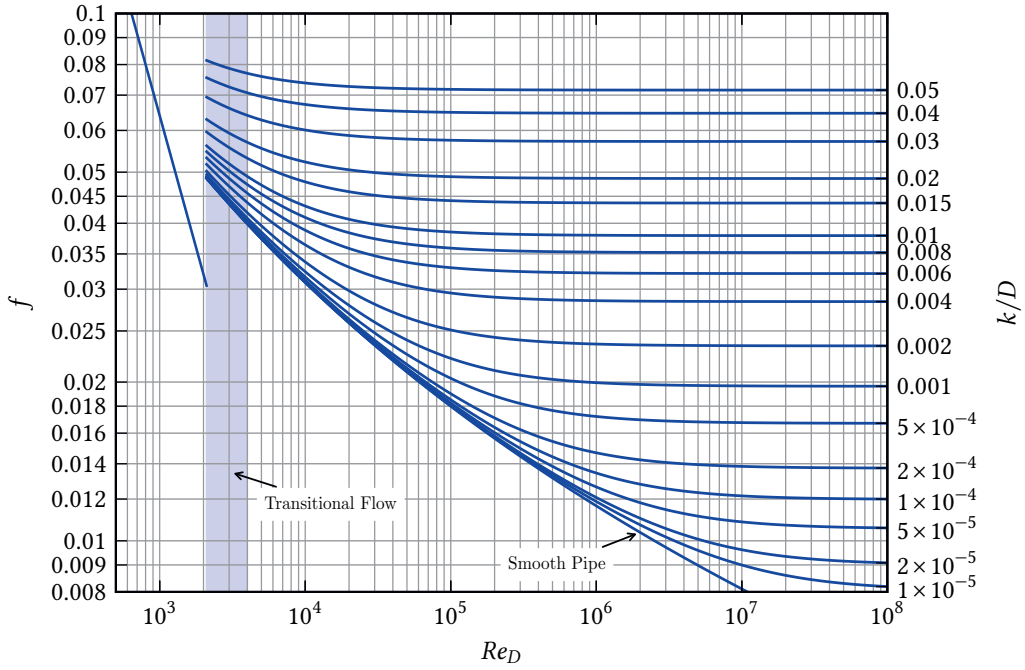

Figure 2.1: Moody's diagram that shows the friction factor, f, as a function of the Reynolds number based on pipe diameter, Re_D. For laminar flow, the friction factor follows the relationship $f = 64/Re$. For turbulent flow, the friction factor over a rough wall is higher than a smooth wall and increases with increasing roughness height k/D. For very high Reynolds numbers, the friction factor becomes constant and it depends only on the pipe roughness flow height. This 'fully-rough' regime is reached earlier for higher roughness heights.

- In the presence of roughness, higher drag is observed.
- As the Reynolds number is increased, eventually a point is reached where the friction factor is no longer a function of the Reynolds number in what is referred to as the fully-rough regime. The roughness alone determines the friction factor.

Moody's diagram is a very useful engineering tool. Given a known Reynolds number and roughness height, it is trivial to calculate the expected drag increase with respect to a smooth wall. However, therein lies its inherent weakness: the drag increase depends on the Reynolds numbers. Rough-wall flows often find applications within a wide range of Reynolds numbers, and the exact conditions may not be feasible to faithfully replicate with numerical and/or experimental studies, due to the associated cost. Often, therefore, the Hama roughness function ΔU^+ is used to characterise the drag increase over rough surfaces. The Hama roughness function is a Reynolds-independent measure of drag increase and represents the upwards/downwards shift, corresponding to a drag decrease/increase with respect to the logarithmic region in a typical smooth wall turbulent velocity profile, see figure 2.2 (*a*), and is generally a function of the viscous-scaled roughness height and the roughness type. By matching the viscous-scaled roughness height at lower Reynolds

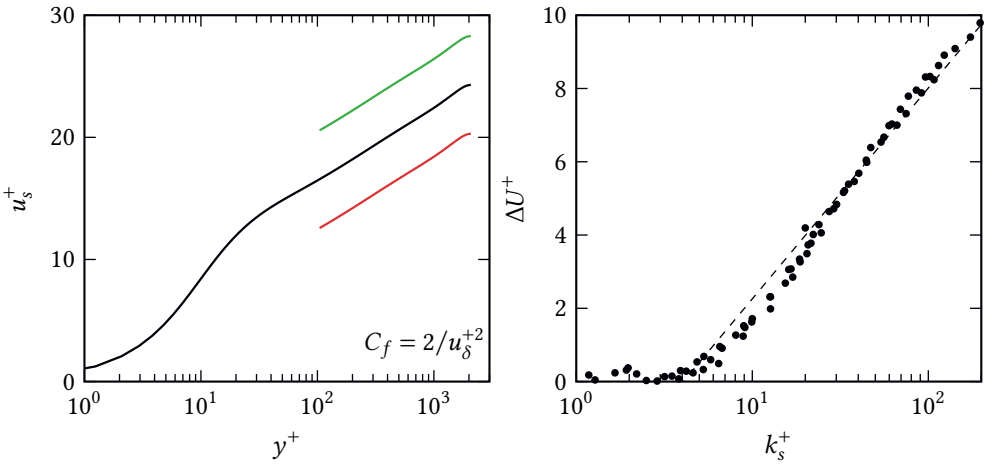

Figure 2.2: (*a*) A typical smooth wall turbulent streamwise velocity profile u as a function of the wall-normal distance, y, along with a depiction of the ΔU^+. The upward shift (negative $\Delta U+$) represents a drag decrease and a downward shift (positive ΔU^+) represents a drag increase. (*b*) ΔU^+ of sand-grain roughness of Nikuradse [13], where k_s is the sand-grain roughness length. Quantities normalised by the viscous length scale and the friction velocity are shown with the superscript $^+$.

numbers, the Hama Roughness function can be used to quantify drag at the expected Reynolds numbers while using lower Reynolds numbers. A smooth wall turbulent velocity profile exhibits a region with a logarithmic velocity profile, of the form,

$$u_s^+ = \frac{1}{\kappa}\ln(y^+) + B, \tag{2.1}$$

where $B \approx 5$, $u_s^+ = u_s/u_\tau$ is the streamwise velocity normalised by the friction velocity and $y^+ = y/\delta_v$ is the viscous-scaled wall-normal distance from the wall. Here, $\delta_v = \nu_w/u_\tau$ and $u_\tau = \sqrt{\tau_w/\rho_w}$ the friction velocity, τ_w is the drag per plane area and the subscript w denotes quantities evaluated at the wall. The ΔU^+ is an alternative and equivalent way of expressing the friction factor of the Moody diagram, and it is directly related to the added drag, ΔD, through the relation [22],

$$\Delta D = 1 - \frac{C_f}{C_{f,s}} = 1 - \frac{1}{\left(1 - \dfrac{\Delta U^+}{\sqrt{2/C_{f,s}}}\right)^2}, \tag{2.2}$$

where C_f is the friction coefficient and the subscript 's' denotes smooth wall values. The effect of Reynolds number on ΔD is embedded in $C_{f,s}$, which can be easily estimated using smooth-wall formulas, allowing one to use low Reynolds number data to estimate the drag variation in operating conditions. A positive ΔU^+ is correlated with a drag increase and represents a downward shift of the velocity profile with respect to the smooth wall and vice versa, see figure 2.2 (*a*). By employing the ΔU^+ to characterise drag, all curves of

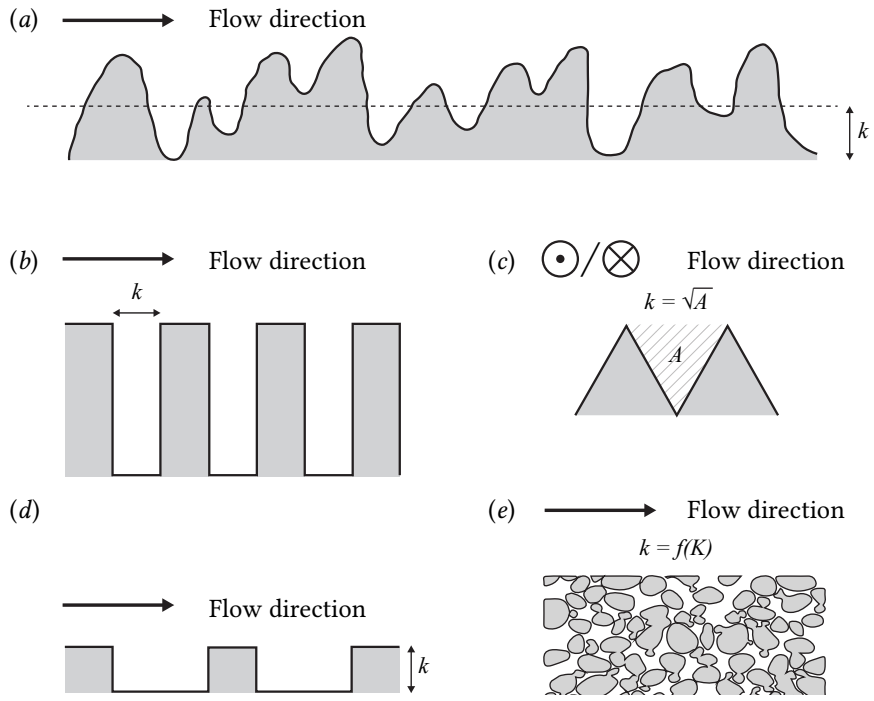

Figure 2.3: Different roughness geometries such as randomly distributed roughness (*a*), spanwise invariant bars (*b*), riblets (*c*), cubical roughness (*d*) and permeable roughness (*e*). k shows the effective roughness length scale that represents the most representative roughness length scale that captures the influence of the roughness on the flow. K is the Darcy permeability. Arrows show direction of the flow. Riblets are aligned with the flow direction and flow is into/out of the page.

the Moody diagram collapse on to the same curve, as in the work of Nikuradse [13], and the ΔU^+ approaches the asymptotic fully rough regime as the characteristic length scale of the roughness becomes large, see figure 2.2 (*b*).

Different families of roughness topographies follow essentially the same trends, and the data tends to collapse onto a the asymptote, $\Delta U^+ = 1/\kappa \ln(k^+) + C(k^+)$, where $C(k^+)$ is a function of the roughness geometry and the roughness Reynolds number. The question then becomes one of finding the correct characteristic length scale of roughness, and for the purposes of uniformity, determining how the characteristic length scale correlates with the sand-grain roughness of Nikuradse [13], i.e to find a ratio between the sand-grain roughness length scale and the relevant roughness length scale, $k_s/k = \exp\{\kappa[C_s(\infty) - C(\infty)]\}$.

The task to come up with a single characteristic length scale for roughness is not a trivial mater. The characteristic length scale of roughness is meant to, within a reasonable

degree of accuracy, reduce the influence of roughness on to a single characteristic of the surface that determines primarily how the surface interacts with the turbulent flow. The protrusion height of sand-grain roughness was used in the seminal work of Nikuradse [13], such as in the work of Choi [23], Jiménez et al. [24] and Flack and Schultz [25]. Different length scales have been investigated for a wide range of geometries. In the case of riblets, as an example, Garcia-Mayoral and Jiménez [26] proposed the square root of the cross-sectional area between the riblets. For square roughness, the height of the roughness is commonly taken as the characteristic roughness length scale [27]. In the case of very deep spanwise bars, the width instead of the height, however, was shown to perhaps better characterise the drag [19]. Figure 2.3 shows some of these configurations and the different roughness length scales that characterise them.

Such canonical rough surfaces have been studied and well-documented. For cases such as permeable surfaces, their relevant characteristic length scales are still not known. The protrusion height of sand-grain roughness no longer makes sense for permeable surfaces. A plate with multiple holes drilled into it, as in the case of an acoustic liner facesheet, does not protrude into the flow. It is not known, therefore, whether the trends that we seem to take for granted for canonical rough wall surfaces would also apply to such non-canonical cases.

2.2 Permeable Rough Surfaces and Acoustic Liners

2.2.1 Permeable surfaces in normal flow

Permeable surfaces represent a special kind of rough surface in that they allow fluid to penetrate though them, such as in the case of metal foams and gravel. They have been studied far less than canonical rough surfaces, although they are very common in engineering. Perforated plates, in particular, are used for flow conditioning [28], enhancing heat transfer in heat exchangers [29], flame control in combustion chambers [30], aircraft trailing edge noise abatement [31] and acoustic liners in aircraft engines [32, 33].

More specifically, the 'permeability' of a medium represents the ease with which fluid passes through a medium, i.e the pressure drop experienced for a particular mass flow rate,

$$\frac{\partial P}{\partial x_j} = \mu\sigma(u_j)^f K_{ij}^{-1} + \mu\sigma K_{ij}^{-1} F_{jk}(u_k)^f, \tag{2.3}$$

where $\partial P/\partial x_j$ is the pressure gradient across the permeable layer, K_{ij} is the Darcy permeability tensor, F_{jk} is the Forchheimer permeability tensor, and μ is the dynamic viscosity of the fluid, σ is the porosity or open area ratio of the medium and $(u)^f$ is the fluid-phase average velocity of the medium. The more permeable a surface is, the more easily fluid can pass through it and the lower the pressure drop that is experienced.

The Darcy and Forchheimer permeability coefficients represent the linear and non-linear permeability of the medium. The Darcy law (2.4) stems from the momentum balance of the Navier–Stokes equations, and it is usually considered an accurate model of canonical porous surfaces, at least when the Reynolds number based on the pore diameter is small enough that the underlying Stokes approximation remains valid,

$$U_{ci} = -\frac{K_{ij}}{\mu}\frac{\partial P}{\partial x_j}, \tag{2.4}$$

where, $U_{c_i} = \sigma(u_i)^f$ is the characteristic velocity component in i direction. The Forchheimer permeability is a correction to the apparent departure from Darcy's law beyond the limit of creeping flow. Equation (2.4) has been proven to be accurate for many canonical porous surfaces within the limit of Stokes flow, namely for small values of the pore Reynolds number $Re_p = \rho d U_p/\mu$, where U_p is the velocity inside the pore and ρ is the fluid density.

2.2.2 Permeable surfaces in grazing flow

Many applications of permeable surfaces feature turbulent grazing boundary layers over perforated plates, which, similar to canonical rough surfaces, result in higher drag than the baseline smooth wall. These surfaces have typically been characterised, modelled and studied using their permeability. Typical permeable surfaces such as metal foams and gravel are characterized by large porosity, $\sigma > 0.8$, but very small pore diameters, $d/\delta < 0.01$ and $d^+ = d/\delta_v < 20$ for common applications [34, 21], where δ is the boundary layer thickness and δ_v is the viscous length scale. These small pore sizes allow us to accurately model this type of surfaces using simplified models that consider only the Darcy permeability. Several authors have used Darcy boundary conditions to model the turbulent flow over porous substrates [35, 36] and reported accurate results as compared to pore-resolved simulations [37].

With the exception of some particular configurations [38], porous surfaces tend to increase drag, similar to surface roughness/topography. Similar to canonical rough surfaces, effort has been towards finding a universal length scale for permeable surfaces that represents the influence of the permeable surface on the flow, in a similar vein to the equivalent sand-grain roughness height. For porous surfaces, two types of length scales have generally been considered, namely the pore size d and the square root of the permeabilities $\sqrt{K_{ij}}$, but several authors have shown that drag depends on the dominant viscous-scaled permeability component, or a combination of $\sqrt{K_{ij}}^+ = \sqrt{K_{ij}}/\delta_v$ [38, 35, 39]. More recently, the work of Esteban et al. [40] showed that the relevant length scale is a combination of the pore geometry, or roughness, and its permeability. Esteban et al. [40] carried out experiments of permeable surfaces and delineated the effects of roughness and permeability by considering permeable surfaces with constant permeability but different thicknesses. They found that changing the thickness altered the added drag and such an effect could be attributed to the 'roughness' component of the geometry. In essence, permeable surface have both a roughness component and a permeable component and the two are, often, inseperable.

An important finding of Esteban et al. [40] was that permeable surfaces do indeed approach a fully rough regime, in a similar way as canonical rough surfaces, providing some confidence that our knowledge of canonical rough surfaces can also be extrapolated to permeable surfaces. However, their results were in contrast to those of Manes et al. [41], who studied permeable beds and noted that permeable surfaces did not in fact reach a fully rough regime, hinting perhaps that the way that permeable surfaces interact with the turbulent flow could be very dependent on the exact permeability tensor, or perhaps the influence depends on the 'roughness' component of a permeable surfaces.

Some authors attempted to separate these two concurring effects. Breugem et al. [39] carried out direct numerical simulation (DNS) of porous surfaces by modelling the substrate with a Darcy boundary condition. The authors pointed out that the duality between 'rough' and 'porous' surface is reflected in the presence of three concurring length scales, namely

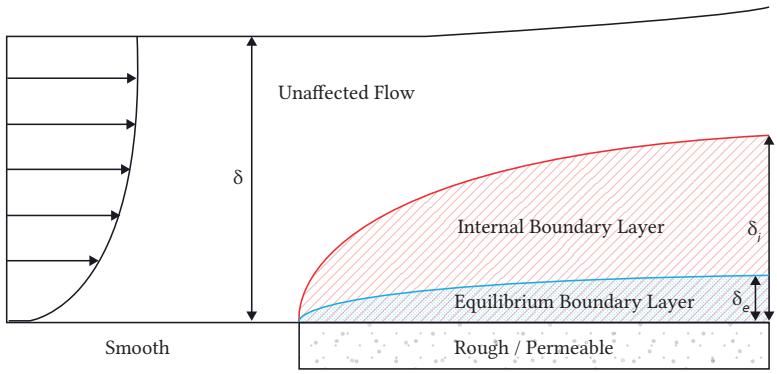

Figure 2.4: Schematic depicting the development of the internal boundary layer after a smooth-to-rough transition. The red line depicts the height of the internal boundary layer and its development in the streamwise direction and the blue line indicates the extent of the equilibrium boundary layer.

the boundary layer thickness δ, the pore diameter d, and the square root of the permeability $\sqrt{K_{ij}}$. These length scales can be converted into the friction Reynolds number $Re_\tau = \delta/\delta_v$, the viscous-scaled pore diameter $d^+ = d/\delta_v$ and the viscous-scaled square root of the permeability $\sqrt{K_{ij}}^+ = \sqrt{K_{ij}}/\delta_v$. The authors reason that the effect of the 'roughness' and 'porous' components are separated if there is enough separation between d^+ and $\sqrt{K_{ij}}^+$ while having $d << \delta$.

Another aspect that is not very well understood for permeable surfaces is how the flow would interact to a step change in permeability and whether it would interact in a similar manner to canonical roughness. As changes in surface roughness are commonplace, the study of how the flow reacts to a step change in surface roughness has been studied and documented for canonical rough surfaces [42, 43, 44]. Canonical rough wall surfaces have been studied to understand how these sudden changes in surface roughness influence flow development. Following a smooth-to-rough transition, the entirety of the boundary layer does not immediately feel the effects of the new surface condition. An internal boundary layer (IBL) begins to develop and the height of the IBL demarcates how far the influence of the new surface extends, growing to engulf the entire boundary layer, see figure 2.4.

In order to demarcate the height of the IBL, changes in the mean streamwise velocity and/or the mean Reynolds stress are used. The seminal work of Elliott [42] identified that following a step change in surface roughness, two logarithmic regions exist in the mean streamwise velocity profile, and identified the height of the IBL as the intersection of the two logarithmic regions in the velocity profile. Cheng and Castro [43] studied two dimensional rib-type roughness also opted to use changes in the streamwise velocity to identify the height of the IBL and identified the height of the IBL as the point where the downstream velocity reaches 99% of the upstream velocity at the same height. Efros and Krogstad [45],

opted instead to identify how the streamwise Reynolds stress reacts to the new surface geometry and identified the height of the IBL by tracking the wall-normal extent to which the streamwise Reynolds stress had been altered by the new surface roughness. Alternative definitions of the height of the IBL employ similar techniques to identify changes in the mean streamwise velocity or the mean streamwise Reynolds stress, and depending upon the exact definition used, the resulting growth rate, θ differs [44] and there is, in general, no real consensus on the exact definition to be used. Efros and Krogstad [45] noted a growth rate of $\theta \approx 0.7$, compared to $\theta \approx 0.8$ for Elliott [42] and $\theta \approx 0.33$ for Cheng and Castro [43], with the difference in growth rate primarily down to the different definitions employed [44].

Regardless of the defintion employed to calculate the height of the IBL and the geometry considered, the growth rates for canonical surfaces have generally ranged between $\theta \approx 0.2$–0.8. However, while canonical rough surfaces have been investigated, it is not clear that permeable surfaces behave in a similar manner and whether the growth rate of the IBL over permeable surfaces follows similar trends as rough canonical surfaces. Efstathiou and Luhar [34] observed that the IBL over their porous surface grew rapidly to the edge of the boundary layer within 10δ in a similar manner to canonical rough surfaces. However, the exact growth rates of the IBL were not measured and a more qualitative comparison was done with canonical rough surfaces. A more quantitative description of flow recovery and the comparison between canonical rough wall flows and their permeable surface was missing.

2.3 Acoustic Liners

Acoustic liners differ from typical permeable surfaces as they are only permeable in the wall normal direction due to the perforated facesheet at the top and the relatively larger pores with respect to the boundary layer thickness of the grazing flow, $d/\delta \approx \mathcal{O}(0.1)$ [46]. It is not clear, however, whether the same principles that govern the flow over canonical permeable surfaces also apply to acoustic liners. Pores with large diameter have the potential to substantially alter the flow physics compared to typical permeable surfaces and may lead to significant mass flow rate through their pores; they exhibit higher pore Reynolds numbers than typical canonical permeable surfaces. Deviations from Darcy's law for increasing Re_p are well documented in the literature [47, 48, 49], and have been associated with nonlinear effects that arise at high pore Reynolds numbers. Therefore, for the case of acoustic liner type permeable surfaces with a perforated plate facehseet, it is not sufficient to only take into account the Darcy drag. Equation (2.4) is, therefore, replaced by,

$$\frac{\Delta P}{t}\frac{d^2}{\mu U_t} = \frac{d^2}{K_y} + \sigma\alpha_y d Re_p, \tag{2.5}$$

where U_t is the superficial velocity (Figure 2.5 (a)), t is the thickness of the plate and K_y and α_y are the permeability and the Forchheimer coefficient in the direction normal to the plate, respectively [49, 48]. The superficial velocity is the hypothetical uniform incoming velocity perceived by the orifice [47]. This is related to the orifice velocity by mass conservation,

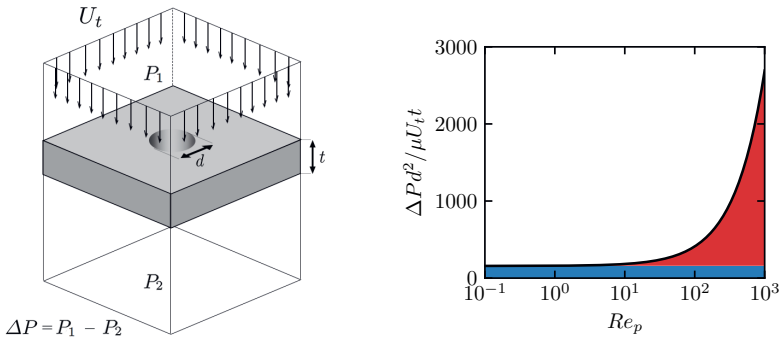

Figure 2.5: (*a*) Sketch of the flow normal to a perforated plate with diameter d and thickness t. U_t is the superficial velocity and $\Delta P = P_1 - P_2$ the pressure drop through the plate. (*b*) Darcy (blue) and Forchheimer (red) contributions to the pressure drop from Equation (2.5) as a function of the pore Reynolds number Re_p for $\sigma = 0.322$ and $t/d = 1$.

$$U_t A_p = U_p A_o \quad \Rightarrow \quad U_t = \sigma U_p, \quad \sigma = \frac{A_o}{A_p}, \tag{2.6}$$

where A_p and A_o are the plate and the orifice area, respectively. Hence, the superficial velocity can be interpreted as measure of the total mass flow rate through the permeable surface.

Numerical and experimental simulations of acoustic liners are also a challenging endeavor. Experimentally, it is very difficult to accurately measure drag. Numerically, it is difficult to replicate the operating conditions and the range of length scales of acoustic liners. Figure 2.6 shows that the plate porosity is relatively small, typically $\sigma = 0.08$–0.3 and the orifice diameter is about 2–3mm. The orifice diameter with respect to the boundary layer length scales can be estimated assuming an aircraft at cruise condition with freestream Mach Number $M_\infty \approx 0.3$–0.6, freestream velocity $u_\infty \approx 90$–$180 m/s$, and kinematic viscosity $\nu \approx 3.5 \times 10^{-5} m^2/s$. In these conditions, we can estimate a friction Reynolds number $Re_\tau \approx 3300$–5400, with boundary layer thickness $\delta \approx 30mm$, and viscous length scale $\delta_v = 5$–$10\mu m$. Therefore, acoustic liners in operating conditions have $d/\delta \approx 0.07$, $d^+ \approx 200$–400. The depth of a cavity is typically $h = 40mm$, corresponding to $h/\delta \approx 1.3$. Satisfying both these constraints from a numerical perspective is quite challenging and implies a very high computational cost. Nevertheless, there have been efforts recently at studying acoustic liners, both experimentally and numerically, albeit with simplifications such as studying only a single cavity [46] or replacing the acoustic liner altogether with an equivalent impedance boundary condition [50], in order to reduce the computational cost. We have performed the first fully resolved simulations Shahzad et al. [51] of acoustic liner arrays that provide accurate details of the interaction of these liners with the flow.

Wilkinson [10] was among the first to perform experiments of turbulent boundary layers over porous plates for different values of the viscous-scaled orifice diameter $d^+ := d/\delta_v$, viscous-scaled plate thickness $t^+ := t/\delta_v$ and plate porosity (open-area ratio) σ.

More recently, several experiments have been conducted in the Grazing Flow Impedance Tube (GFIT) facility at NASA [52] and considerable effort has been dedicated to estimating

Figure 2.6: The typical pore size of acoustic liners used in turbofan engines.

the added drag provided by acoustic liners using a static pressure drop approach [11, 53, 54]. These experimental campaigns considered several liner geometries, for both conventional and more exotic configurations [11, 54], and reported a drag increase between 16% and 350% compared to a smooth wall.

An important finding of the GFIT experiments is that the cavity depth has a negligible contribution to the total drag in the absence of acoustic waves, which instead is largely influenced by the orifice diameter, plate porosity and the facesheet thickness. For instance, Howerton and Jones [11] noted that, for constant porosity, reducing the diameter of the orifices reduced drag. Similarly, Howerton and Jones [54] reported 50% drag increase for porosity $\sigma = 0.08$ and 400% drag increase for $\sigma = 0.3$, for the same flow conditions and approximately the same orifice diameter. Additionally, these experiments suggest that it is possible to reduce the drag penalty without harming the noise attenuation.

Aerodynamically optimized acoustic liners have been proposed, although the novel geometries were mostly based on trial and error rather than on a solid understanding on the flow physics. Howerton and Jones [53] studied different orifice configurations, changing the orifice shape and orientation, including rectangular orifices either parallel or perpendicular to the flow, and found that the perpendicular slot orifice performed better compared to the baseline circular orifices. The parallel slot orifice, on the other hand, despite having the same dimensions as the perpendicular slot orifice, had the highest added drag, at a freestream Mach number $M_\infty = 0.3$. Furthermore, Howerton and Jones [53] noted that, despite the changes in the orifice shape, the acoustic performance was largely unchanged, meaning that there is potential for reducing the added drag, without hampering the acoustic performance.

Gustavsson et al. [55] performed experiments over several acoustic liner geometries and reported a drag increase between 30%–50%, without incoming acoustic waves, arguing

that the added drag might be even larger in the presence of incoming noise.

Previous numerical simulations of turbulent flows over acoustic liners very often they relied on simplified configurations or wall models because pore-resolved simulations are computationally expensive. A common approach that has been pursued for reducing the computational cost is to simulate a single cavity rather than an array of resonators [56, 7, 46]. Zhang and Bodony [7] performed DNS of turbulent grazing flow over a single resonator with a similar cavity geometry as the one studied by Howerton and Jones [11] in the GFIT [57]. However, the simulations were at a much lower friction Reynolds number, see table 2.1. For a free stream Mach number $M_\infty = 0.5$, Zhang and Bodony [7] reported a minor drag increase of 4.2% with respect to a smooth wall in the absence of sound waves. These results seem to contradict experiments of Howerton and Jones [11] who reported a drag increase of about 50%, at matched Mach number and cavity geometry. This discrepancy can probably be traced back to the simplified numerical setup wherein only one single orifice is simulated, resulting in a very low porosity $\sigma = 0.0099$, compared to $\sigma = 0.08$ in the experiments.

Another common simplification in numerical simulation is to approximate the effect of acoustic liners with an equivalent impedance boundary condition [58], which substantially reduces the computational cost. However, the accuracy with which the impedance boundary condition represents the real acoustic liner geometry is not well understood and discrepancies can be observed in literature. For instance, Olivetti et al. [59] performed DNS of turbulent pipe flow with impedance boundary conditions and did not report changes in the structure of the near-wall turbulence. On the contrary, Scalo et al. [50] and Sebastian et al. [60] performed large eddy simulations (LES) of turbulent channel flow with a characteristic impedance boundary condition [61, 62], and noted significant changes in the structure of the near-wall cycle which could, in some cases, be completely replaced by Kelvin–Helmholtz-like rollers, with drag increase up to 500%.

The difficulty studying acoustic liners and their drag also stems from the complex environment that they operate in. In realistic operating conditions, not only are acoustic liners subject to turbulent grazing flow, but also high amplitude acoustic forcing. The coupled interaction of turbulent grazing flow and acoustic forcing leads to a complex flow phenomena inside the orifice. Zhang and Bodony [7] studied acoustic liners under the combined action of grazing flow and acoustic forcing, noting how acoustic forcing leads to high wall-normal velocity fluctuations that may dwarf the turbulent fluctuations if the amplitude of the forcing is high enough.

The work of Zhang and Bodony [7] represents the sole DNS that attempts to highlight flow features of acoustic liners under the simultaneous action of acoustic forcing and a turbulent grazing boundary layer, quantifying the acoustic performance by the acoustic impedance. The impedance $Z = p/v_{a,n}$, from which the impedance boundary condition derives from, quantifies the response of an acoustic liner and is the ratio of the pressure to the acoustic velocity normal to the resonator orifice. It is related to the acoustic sound absorption by,

$$\text{Absorption coefficient } = 1 - \left\| \frac{Z(\omega) - 1.0}{Z(\omega) + 1.0} \right\|^2 . \tag{2.7}$$

The impedance has been extensively used to characterise acoustic liners, initially in

the absence of grazing flow and more recently in the presence of grazing flow. Tam et al. [63] showed how a mean grazing flow changes the impedance of the acoustic liner, and by extension, the acoustic absorption characteristics. So while it is relatively well understood that acoustic performance is altered by sound waves, the converse is not very well understood. Zhang and Bodony [7] showed how drag increases with the strength of the acoustic forcing. Zhang and Bodony [7] noted a drag increase of 25% in the presence of $140dB$ sound waves and a drag increase of approximately 100% in the presence of $160dB$ sound waves, compared to 4.2% without sound waves, hinting at a significant influence of acoustic forcing on the aerodynamic performance. However, the results are in contrast with the experiments of Howerton and Jones [11] who saw virtually no influence of $140dB$ acoustic waves on the added drag, similar to the results presented in the thesis that show no change in drag with the addition of acoustic waves, highlighting the discrepancies that are common in studies investigating aerodynamic influence of acoustic liners.

The literature study summarized in table 2.1 shows that reported values for the actual drag increase caused by acoustic liners vary between 2% and 500%. This literature survey shows that there have been several attempts to measure the added drag caused by acoustic liners, both experimentally and numerically, suggesting a large interest of the community in this topic. However, the discrepancies between previous studies are too large to be acceptable. This large uncertainty can be associated with the critical modelling assumptions that have been used in numerical simulations and the difficulty in measuring drag in experiments. There seems to be a consensus that the added drag depends both on the orifice diameter d and the porosity of the facesheet σ. This type of functional dependency has been observed in turbulent grazing flows over porous substrates, which is a hint that acoustic liners might be regarded as porous surfaces, permeable only in the wall-normal direction.

Furthermore, it is not known whether there is a degree of similarity in the behaviour between canonical permeable surfaces and acoustic liners. Acoustic liners, due to their relatively large pore diameter, may lead to significant momentum exchange inside the orifices. At sufficiently high pore Reynolds number, Darcy drag can be assumed negligible and the entirety of the pressure drag is due to the nonlinear term. The pressure drop characteristics of perforated plates at high Reynolds numbers $Re_p \geq \mathcal{O}(10^2)$ have been studied extensively both numerically [47] and experimentally [64, 65, 66, 67, 68]; however Equation (2.5) for the normal flow has never been associated to the case of grazing boundary layer over porous surfaces, for which Darcy's law has always been used, to our knowledge.

In this work, we aim at developing a rigorous theoretical framework to characterize acoustic liners within the larger body of non-smooth surface textures. We believe that this can only be achieved by performing pore-resolved DNS, which allows us to have access to the 3D flow field and to accurately measure the drag without relying on additional modelling assumptions.

	M_∞	Re_δ	Re_τ	h/δ_v	h/δ	d/δ_v	d/δ	t/δ_v	t/δ	σ	$\Delta D(\%)$
Howerton and Jones [11]	$0.1-0.5$	$2.44\times10^{5\,\circledast}$	$7800^\circledast$	$14200^\circledast$	$1.8^\circledast$	$180-370^\circledast$	$0.025-0.05^\circledast$	$370^\circledast$	$0.05^\circledast$	0.08	$30-50\%$
Howerton and Jones [53]	$0.3-0.5$	$2.44\times10^{5\,\circledast}$	$7800^\circledast$	$14200^\circledast$	$1.8^\circledast$	$280^\circledast$	$0.036^\circledast$	$280^\circledast$	$0.036^\circledast$	0.08	$16-20\%$
Howerton and Jones [54]	$0.3-0.5$	$2.44\times10^{5\,\circledast}$	$7800^\circledast$	$14200^\circledast$	$1.8^\circledast$	$280^\circledast$	$0.036^\circledast$	$280^\circledast$	$0.036^\circledast$	0.1	$10-15\%$
	$0.3-0.5$	$2.44\times10^{5\,\circledast}$	$7800^\circledast$	$14200^\circledast$	$1.8^\circledast$	$660^\circledast$	$0.084^\circledast$	$660^\circledast$	$0.084^\circledast$	0.2	$80-130\%$
	$0.3-0.5$	$2.44\times10^{5\,\circledast}$	$7800^\circledast$	$14200^\circledast$	$1.8^\circledast$	$470^\circledast$	$0.06^\circledast$	$470^\circledast$	$0.06^\circledast$	0.3	$200-350\%$
Wilkinson [10]	0	$(2.8-6.4)\times10^{4\,\dagger}$	$500-2000^\dagger$	$350-1100$		$40-150$		$30-150$		$0.06-0.12$	$2-20\%$
	0	$(2.8-6.4)\times10^{4\,\dagger}$	$500-2000^\dagger$	$600-3700$		$9-55$		$6-35$		$0.047-0.139$	$30-60\%$
Shahzad et al. [69]	0.3	$(0.9-3.5)\times10^4$	$500-2000$	$250-1000$	0.5	$40-160$	0.08	$40-160$	0.08	$0.03-0.3$	70%
Gustavsson et al. [55]	$0.3-0.6$	$(4.8-8.3)\times10^{4\,\dagger}$	$2000-3000^\dagger$	$12000-20000^\dagger$	$5.85-6.05^\dagger$	$350-550^\dagger$	$0.15-0.17^\dagger$	$360-600^\dagger$	$0.15-0.17^\dagger$	0.0853	$30-50\%$
Zhang and Bodony [7]	0.	$2.26\times10^{4\,\dagger}$	-	-	-	114	0.05	-	-	0.0099	$4-100\%$
Scalo et al. [50]	$0.05-0.5$	6900	-	Impedance Boundary Condition							$\leq 325\%$
Sebastian et al. [60]	0.3	6900	$400-1000$	Impedance Boundary Condition							$\leq 575\%$
Jiménez et al. [24]	0	2830	$180-215$	Resistance Boundary Condition ($X=0$)							$21-44\%$

Table 2.1: Dataset of previous studies on drag over acoustic liner geometries. M_∞ is the Mach number. $Re_\delta = u_0\delta/\nu$ is the Reynolds number based on the boundary layer thickness and external velocity (free-stream velocity for boundary layers or bulk flow velocity for channel flow simulations) and Re_τ is the friction Reynolds number. The liner geometry is defined by the orifice diameter d, the depth of the cavity h, the thickness of the facesheet t and the porosity σ. ΔD is the increase in drag observed in these studies. Quantities that are approximated are denoted using the † superscript. Quantities that are approximated using RANS simulations of the GFIT by Zhang and Bodony [7] are denoted using the $^\circledast$ superscript.

3

Numerical Methodology

Prior work on acoustic liners have employed simplifications such as the use of modelled boundary conditions. These simplifications do not provide an accurate picture of the flow and it is not known how well they represent realistic acoustic liner geometries. We perform fully resolved simulations of acoustic liner geometries to get an accurate image of the flow.

Acoustic liners are subject to grazing flow and incoming acoustic waves and it is not known which geometric features primarily influence their behaviour. The orifice diameter, porosity, number of holes per cavity, cavity size and cavity depth are just some of the parameters that could influence acoustic liner behaviour. We perform a systematic analysis of acoustic liner geometries with:

- Channel flow simulations that are computationally tractable to perform a parametric study of acoustic liner geometries and their influence on turbulent grazing flow.
- Boundary layer simulation of acoustic liner geometry in the absence of sound waves to understand the influence of a changing boundary layer on acoustic liner behaviour.
- Boundary layer simulation of acoustic liner geometry in the presence of sound waves to understand the combined influence of acoustics and grazing turbulent flow.

The numerical methodology is detailed in the following sections.

3.1 Direct Numerical Simulation

We solve the compressible Navier–Stokes equations for a calorically perfect gas,

$$\frac{\partial \rho}{\partial t} + \frac{\partial \rho u_i}{\partial x_i} = 0, \tag{3.1}$$

$$\frac{\partial \rho u_i}{\partial t} + \frac{\partial \rho u_i u_j}{\partial x_i} = -\frac{\partial p}{\partial x_i} + \frac{\partial \sigma_{ij}}{\partial x_j} + \Pi \delta_{i1}, \tag{3.2}$$

$$\frac{\partial \rho E}{\partial t} + \frac{\partial \rho u_i H}{\partial x_i} = -\frac{\partial q_i}{\partial x_i} + \frac{\partial \sigma_{ij} u_i}{\partial x_j} + \Pi u_1 + \Pi_T, \tag{3.3}$$

where $u_i = \{u_1, u_2, u_3\} = u, v, w$ are the velocity components, $x_i = \{x_1, x_2, x_3\} = \{x, y, z\}$ are the streamwise, wall-normal and spanwise spatial coordinates, p is the pressure, $E = c_v T + u_i u_i / 2$ is the total energy per unit mass, T is the temperature, ρ is the density, and $H = E + p/\rho$ is the total enthalpy. c_p and c_v are the heat capacities at constant pressure and constant volume. q_j and σ_{ij} are the heat flux vector and viscous stress tensor,

$$\sigma_{ij} = \mu \left(\frac{\partial u_i}{\partial x_j} + \frac{\partial u_j}{\partial x_i} - \frac{2}{3} \frac{\partial u_k}{\partial x_k} \delta_{ij} \right), \tag{3.4}$$

$$q_j = -k \frac{\partial T}{\partial x_j}, \tag{3.5}$$

where $k = c_p \mu / Pr$ is the thermal conductivity. The Prandtl number is $Pr = 0.72$. The viscosity dependence on the temperature is accounted for using a power law with exponent 0.75.

3.1.1 Numerical Scheme

The Navier–Stokes equations are solved using the solver STREAmS [70]. The non-linear advection terms in the Navier–Stokes equations are discretized using an energy-conservative scheme in locally conservative form [71]. The non-linear terms in the Navier–Stokes are of the form:

$$\frac{\partial \rho u_i \Theta}{\partial x_i}, \tag{3.6}$$

where Θ is the quantity being transported. $\Theta = 1$ for the continuity equation, $\Theta = u_i$ for the momentum equations and $\Theta = H$ for the total energy equation. The flux at $x = x_j$ can be approximated using,

$$\left.\frac{\partial \rho u \Theta}{\partial x}\right|_{x=x_j} \approx \frac{1}{\Delta x}\left(\hat{f}_{j+1/2} - \hat{f}_{j-1/2}\right), \tag{3.7}$$

where $\hat{f}_{j+1/2}$ is a numerical flux. The numerical flux, $\hat{f}_{j+1/2}$ can be approximated using energy-conserving central difference approximations of the first derivative [72] using,

$$\hat{f}_{j+1/2} = 2\sum_{l=1}^{L} a_l \sum_{m=0}^{l-1} (\widetilde{\rho, u, \Theta})_{j-m,l}, \tag{3.8}$$

where a_l are the coefficients for standard central difference approximations of order $2L$. A sixth order scheme is used throughout the simulations in the thesis. Three two point, three variable averaging operator is,

$$(\widetilde{f, g, h})_{j,l} = \frac{1}{8}(f_j + f_{j+l})(g_j + g_{j+l})(h_j + h_{j+l}) \tag{3.9}$$

The viscous terms are expanded into a Laplacian form and approximated with sixth-order central finite-difference formulas to avoid odd-even decoupling phenomena,

$$\frac{\partial}{\partial x}\left(\mu \left.\frac{\partial u}{\partial x}\right|_i\right)\Bigg|_i = \left.\frac{\partial \mu}{\partial x}\right|_i \left.\frac{\partial u}{\partial x}\right|_i + \mu \left.\frac{\partial^2 u}{\partial x^2}\right|_i = \frac{1}{\Delta x^2}\sum_{l=-L}^{L} a_l^2 \mu_{i+l} u_{i+l} + \mu_i \frac{1}{\Delta x^2}\sum_{l=-L}^{L} b_l u_{i+l}, \tag{3.10}$$

where b_l are second order approximations for the standard central finite difference approximations. Time stepping is carried out using Wray's three-stage third-order Runge–Kutta scheme [73],

$$\mathbf{q}^{l+1} = \mathbf{q}^l + \alpha_l \Delta t \mathbf{R}^{(l-1)} + \beta_l \Delta t \mathbf{R}^{(l)}, \tag{3.11}$$

where $\mathbf{q}$ is a solution to the Navier–Stokes, $\mathbf{R}$ is the vector of residuals, Δt is the time step, and $\alpha_l = (0, -17/60, -5/12)$ and $\beta_l = (8/15, 5/12, 3/4)$ are integration coefficients.

3.2 Flow Cases

3.2.1 Channel Flow

For our plane channel flow configuration, the fully developed flow between two plates is driven in the streamwise direction by a uniform body force, Π, which is adjusted every time step to maintain a constant mass flow rate and the power spent is added to the total energy equation. A uniform bulk cooling term, Π_T, is also added to the total energy equation to maintain a constant bulk flow temperature. The bulk velocity, temperature and density are defined as,

$$u_b = \frac{1}{\rho_b V}\int_V \rho u_1 \, dV, \quad T_b = \frac{1}{\rho_b u_b V}\int_V \rho u_1 T \, dV, \quad \rho_b = \frac{1}{V}\int_V \rho \, dV, \tag{3.12}$$

where $V = L_x \times 2\delta \times L_z$ is the fluid volume between $y = -\delta$ and $y = \delta$. For our channel flow simulations, periodic boundary conditions are employed in the streamwise and spanwise direction. In the wall-normal direction, a no-slip isothermal wall-boundary condition is used for simulations with a smooth wall. For the case of acoustic liners, the upper and lower walls are replaced by acoustic liners and the geometry is resolved using an immersed boundary method (IBM).

3.3 Boundary Layer Flow

In a similar fashion to the channel flow simulations, periodic boundary conditions are used in the spanwise direction for the boundary layer simulations. Unlike the channel flow simulations, a velocity profile is assigned at the inflow and forcing terms Π and Π_T are not used. A no-slip isothermal boundary condition is applied using the IBM at the lower wall, that consists of a smooth wall region followed by acoustic liners. A characteristic type non-reflective boundary condition is used at the top boundary. Relaxation characteristic based boundary conditions are used at the inflow and outflow.

3.3.1 Inflow and Outflow Boundary Conditions

Dirichilet boundary conditions are assigned for the density and velocity at the inflow. At the outflow boundary, the reference pressure, p_0 is assigned. The velocity profile assigned at the inlet consists of the mean velocity profile and turbulent velocity fluctuations. The mean velocity profile is approximated using the correlations suggested by Musker [74], and the temperature profile is approximated using temperature-velocity relations for compressible flow [75]. For the turbulent velocity fluctuations, a recycling-rescaling procedure of the form proposed by Pirozzoli et al. [76] is used. A recycling station sufficiently downstream of the inflow is used to recycle, after rescaling, turbulent velocity fluctuations back to the inflow. The rescaling works by dividing the boundary layer into an inner layer and an outer layer and assuming that the fluctuations scale with the viscous-scaled wall-normal coordinate y^+ in the inner layer and by y/δ in the outer layer. The total fluctuations of a given quantity at the inflow is then determined by,

$$\Theta = \Theta_{\text{inn}}(1 - W(y)) + \Theta_{\text{out}} W(y), \tag{3.13}$$

where $W(y)$ is a weighting function [77] and Θ_{inn} and Θ_{out} are the inner and outer layer fluctuations respectively. The velocity fluctuations are further rescaled using rescaling

parameter, $\gamma = (u_\tau \sqrt{\rho_w})_{textin}/(u_\tau \sqrt{\rho_w})_{textrec}$, where the subscripts in and rec denote the inflow and recyling stations respectively.

To minimise reflections, a characteristic-based 'relaxation' boundary condition is used to assign variables at the inflow, outflow and top boundary, of the form proposed by Pirozzoli and Colonius [78]. The relaxation boundary conditions attempt to approximately assign the desired variables at the boundaries, based on the LODI relations [79]. Characteristic boundary conditions perform a characteristic decomposition of the flow normal to the boundary. As an example, at the left and right boundaries, the Navier–Stokes equations can be rewritten as,

$$\frac{\partial \mathbf{q}}{\partial t} + R_x \Lambda_x L_x \frac{\partial \mathbf{q}}{\partial x} = \text{RHS}, \tag{3.14}$$

where the right hand side (RHS) consists of the contribution of the viscous and inviscid fluxes, R_x and L_x are the right and left eigenvectors, and $\Lambda_x = \text{diag}\lambda_l(\lambda_1 = u - c, \lambda_2 = \lambda_3 = \lambda_4 = u, \lambda_5 = u + c)$ are the eigenvalues or characteristic directions. Neglecting the contribution of the viscous and inviscid fluxes, the time derivative of the characteristic variables, defined by $\partial w = L_x q$ can be expressed as,

$$\mathcal{L} = \Lambda_x L_x \frac{\partial q}{\partial x} = \begin{bmatrix} \lambda_1 \left(\dfrac{\partial p}{\partial x} - \rho c \dfrac{\partial u}{\partial x} \right) \\ \lambda_2 \left(c^2 \dfrac{\partial \rho}{\partial x} - \dfrac{\partial p}{\partial x} \right) \\ \lambda_3 \dfrac{\partial v}{\partial x} \\ \lambda_4 \dfrac{\partial w}{\partial x} \\ \lambda_5 \left(\dfrac{\partial p}{\partial x} + \rho c \dfrac{\partial u}{\partial x} \right) \end{bmatrix} \tag{3.15}$$

Characteristics $\mathcal{L}_1$ and $\mathcal{L}_5$ represent outgoing (incoming) and incoming (outgoing) acoustic waves at the inflow (outflow). $\mathcal{L}_2$ represents entropy waves and $\mathcal{L}_3$ and $\mathcal{L}_4$ represent convection of wall-normal and spanwise velocities. At the inflow, $\mathcal{L}_2$, $\mathcal{L}_3$, $\mathcal{L}_4$ and $\mathcal{L}_5$ are used to assign the velocities and density. The inflow and outflow boundary conditions are assigned by splitting up the contribution of the incoming and outgoing waves,

$$\mathcal{L} = \Lambda_x^o L_x \frac{\partial \mathbf{q}}{\partial x} + \Lambda_x^i L_x \frac{\partial \mathbf{q}}{\partial x} \approx \Lambda_x^o L_x D \mathbf{q}_b + \Lambda_x^i L_x P \frac{\mathbf{v}_g - \mathbf{v}_b}{\Delta}, \tag{3.16}$$

where the superscripts o and i represent the outgoing and incoming characteristics, the subscripts b and g represent the boundary node and first ghost node, $\mathbf{v}$ is the vector of primitive variables and $P = \partial \mathbf{q}/\partial \mathbf{v}$. The solution at the boundary can then be advanced in time using,

$$\frac{\partial \mathbf{q}_b}{\partial t} = -R_x \Lambda_x^o L_x \frac{\partial \mathbf{q}}{\partial x} + R_x \Lambda_x^i L_x \frac{\partial \mathbf{q}}{\partial x} \approx \Lambda_x^o L_x D \mathbf{q}_b + \Lambda_x^i L_x P \frac{\mathbf{v}_g - \mathbf{v}_b}{\Delta}. \tag{3.17}$$

As an example, at the outflow, the incoming characteristic is used to assign the pressure,

$$\mathcal{L}_1 = K_o(p - p_d), \tag{3.18}$$

where K_o is a constant and p_d is the desired outflow pressure. In the original formulation of the LODI relations, K_o is inversely proportional to the total length of the domain. In the current formulation, the constant is inversely proportional to the mesh size, implying a greater restoring force to the desired pressure. At the top boundary condition, the incoming characteristics are set to zero, leading to a non-reflecting boundary condition.

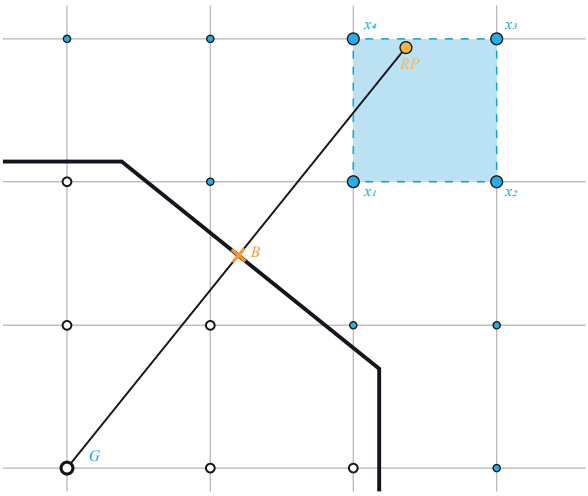

Figure 3.1: Schematic for the ghost-point-forcing immersed boundary method used. Point 'G' represents the ghost point inside the solid body. Point 'RP' represents the reflected point in the fluid corresponding to the ghost point 'G'. Point 'B' is equidistant from 'G' and 'RP' and the line 'GB' is perpendicular to the body. In this 2D representation, the flow variables are assigned to point 'RP' using a bilinear interpolation using points x_1, x_2, x_3 and x_4. In a 3D case, a trilinear interpolation is used. The values at point 'RP' are then used to assign flow variables at the ghost point.

3.3.2 Sound

The assigned outflow pressure is $p_o(t) = p_0 + A\cos(\omega_r T)$, A is the amplitude of the perturbation and T is the time. If no sound wave is imposed at the outflow and the amplitude of the sound wave is set to zero. If sound waves with a sound pressure level, SPL $= 150dB$ are imposed at the outflow, the corresponding amplitude is $A = p_r \cdot 10^{\mathrm{SPL}/20}$, where $p_r = 20\mu$Pa is a reference pressure.

3.3.3 Selective Frequency Damping

In order to prevent interaction and reflection of acoustic waves with the inflow, selective frequency damping (SFD) [80, 81, 82] was used. SFD is based on control theory and

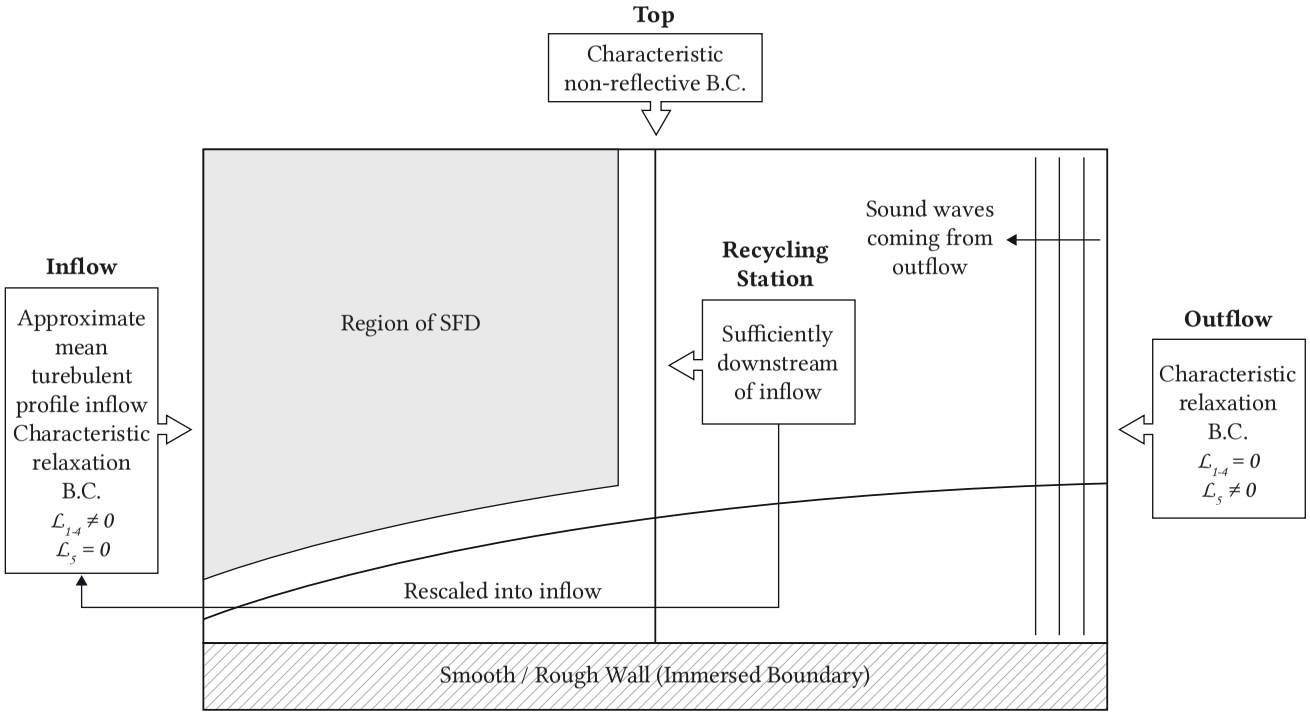

Figure 3.2: Setup of the boundary layer showing the boundary conditions. Flow is from left to right but sound waves are introduced from the outflow.

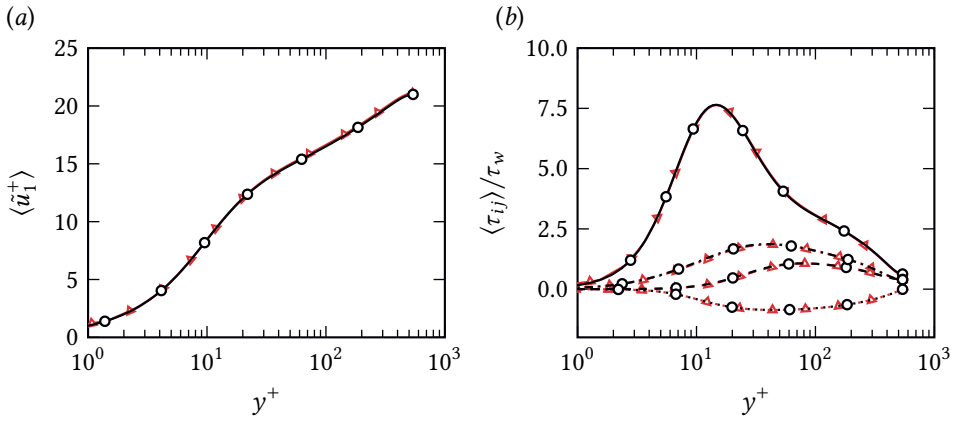

Figure 3.3: Comparison of the average streamwise velocity (*a*) and Reynolds stresses (*b*) between STREAmS [70, triangles] and the DNS of Lee and Moser [83] at $Re_\tau = 550$. In (*b*), different lines represent different components of the Reynolds stress tensor: $\langle \tau_{11} \rangle$ (solid), $\langle \tau_{22} \rangle$ (dashed), $\langle \tau_{33} \rangle$ (dashed-dotted) and $\langle \tau_{12} \rangle$ (dotted).

adds a linear term to the Navier–Stokes to force towards a particular filtered solution, $\dot{\mathbf{q}} = \mathcal{F}(\mathbf{q}) - \chi(\mathbf{q} - \mathbf{q}_f)$, where $\mathbf{q}$ is the vector of conservative variables in the Navier–Stokes, $\mathbf{q}_f$ is the filtered solution, and χ is the control parameter. The encapsulated form of the equations [81] is used where the filtered solution is defined as, $\dot{\mathbf{q}}_f = 1/\Delta(\mathbf{q} - \mathbf{q}_f)$, and Δ represents the cut-off frequency. SFD is used between $x/\delta_0 = 0$ and $x/\delta_0 = 70$ and is only applied in the freestream, outside the influence of the turbulent boundary layer, where δ_0 is the inflow boundary layer thickness. The control parameter χ is ramped up linearly in the upstream direction from $\chi = 0$ at $x/\delta_0 = 70$ to $\chi = \chi_{\max} = 0.8$ for $x/\delta_0 < 45$.

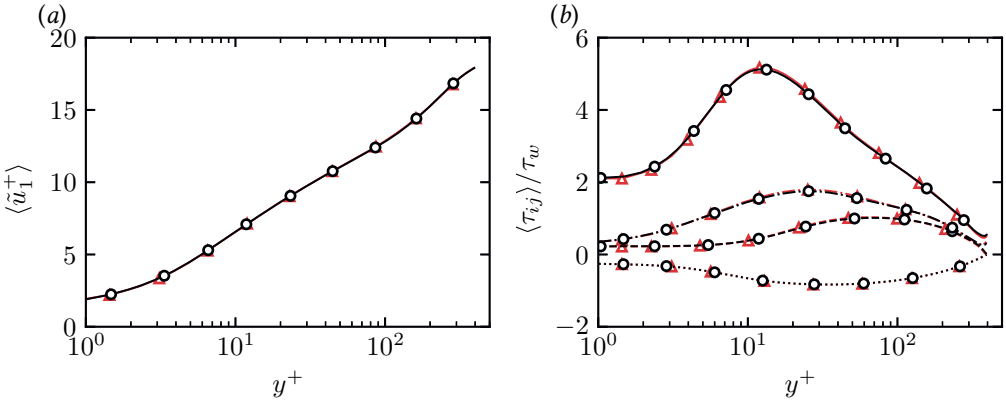

Figure 3.4: Comparison of the average streamwise velocity (*a*) and Reynolds stresses (*b*) between STREAmS [70, triangles] and the DNS of spanwise-aligned bars of MacDonald et al. [19, circles] with streamwise spacing $s^+ = 200$ and height $k^+ = 50$. In (*b*), different lines represent different components of the Reynolds stress tensor: $\langle \tau_{11} \rangle$ (solid), $\langle \tau_{22} \rangle$ (dashed), $\langle \tau_{33} \rangle$ (dashed-dotted) and $\langle \tau_{12} \rangle$ (dotted).

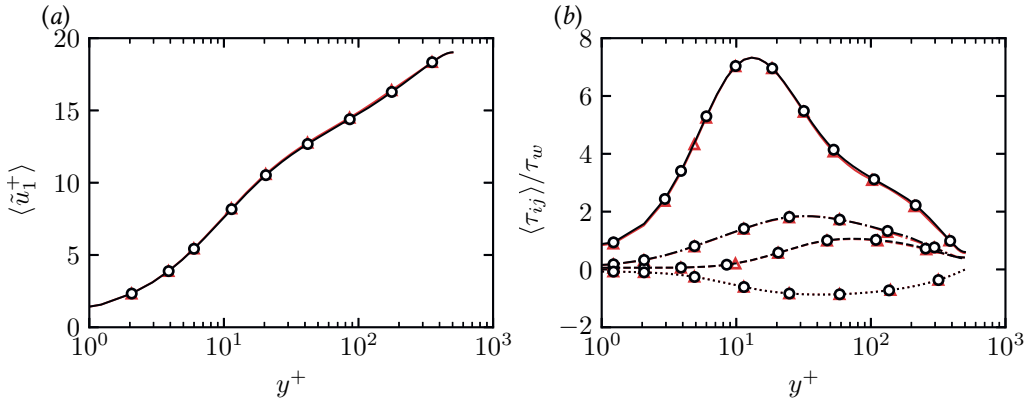

Figure 3.5: Mesh refinement study for flow case $L-L_{32}$: mean streamwise velocity (*a*) and Reynolds stresses (*b*) for the fine mesh (triangles - 40 points per orifice) and the coarse mesh (circles - 26 points per orifice). In (*b*), different lines represent different components of the Reynolds stress tensor: $\langle \tau_{11} \rangle$ (solid), $\langle \tau_{22} \rangle$ (dashed), $\langle \tau_{33} \rangle$ (dashed-dotted) and $\langle \tau_{12} \rangle$ (dotted).

3.4 Immersed Boundary Method

The complexity of the roughness geometry is handled using a ghost-point-forcing immersed boundary method to treat arbitrarily complex geometries [84, 85]. The geometry of the solid body is provided in OFF format for 3D objects. The computational geometry library CGAL [86] is used to perform the ray-tracing to define the grid nodes belonging to the fluid and the solid, and to compute the distance of each point from the interface. To retain the same computational stencil close to the boundaries, the first three layers of interface points inside the body are tagged as ghost nodes. The ghost nodes are assigned fictitious values to assign the proper boundary condition at the surface of the geometry.

Figure 3.1 shows a schematic of the interpolation procedure used for the IBM. For each ghost node, we identify the nearest surface of the geometry and find the intersection point of the line passing through the ghost point, that is orthogonal to the surface. For each ghost node, we identify a reflected point along the wall-normal, laying inside the fluid domain. We interpolate the solution at the reflected point using a trilinear interpolation and use the values at the reflected points to fill the ghost nodes inside the body to apply the desired boundary condition. For a two dimensional case, using bilinear interpolation, a generic flow variable, Θ, at position (x_{RP}, y_{RP}) can be interpolated as,

$$\Theta = c_1 x_{RP} y_{RP} + c_2 x_{RP} + c_3 y_{RP} + c_4, \tag{3.19}$$

with the coefficients determined by solving the linear system of equations,

$$\begin{bmatrix} x_1 y_1 & x_1 & y_1 & 1 \\ x_2 y_2 & x_2 & y_2 & 1 \\ x_3 y_3 & x_3 & y_3 & 1 \\ x_4 y_4 & x_4 & y_4 & 1 \end{bmatrix} \begin{bmatrix} c_1 \\ c_2 \\ c_3 \\ c_4 \end{bmatrix} = \begin{bmatrix} \Theta_1 \\ \Theta_2 \\ \Theta_3 \\ \Theta_4 \end{bmatrix}. \tag{3.20}$$

In the case that one or more of the interpolation nodes intersect the solid body, the solid body itself is used to assign the boundary condition. As an example in the case that $(x1, y1)$ lies inside the solid body, the intersection point, (x_B, y_B) (see figure 3.1), we need to apply a Dirichilet boundary condition amd the coefficients can be determined using,

$$\begin{bmatrix} x_B y_B & x_B & y_B & 1 \\ x_2 y_2 & x_2 & y_2 & 1 \\ x_3 y_3 & x_3 & y_3 & 1 \\ x_4 y_4 & x_4 & y_4 & 1 \end{bmatrix} \begin{bmatrix} c_1 \\ c_2 \\ c_3 \\ c_4 \end{bmatrix} = \begin{bmatrix} \Theta_B \\ \Theta_2 \\ \Theta_3 \\ \Theta_4 \end{bmatrix}, \tag{3.21}$$

where Θ_B is the desired Dirichilet boundary condition. For a Neumann boundary condition, the gradient with respect to the surface normal, $\partial\Theta_B/\partial n$ is imposed instead, and the coefficients are determined by solving,

$$\begin{bmatrix} y_B n_x + x_B n_y & n_x & n_y & 0 \\ x_2 y_2 & x_2 & y_2 & 1 \\ x_3 y_3 & x_3 & y_3 & 1 \\ x_4 y_4 & x_4 & y_4 & 1 \end{bmatrix} \begin{bmatrix} c_1 \\ c_2 \\ c_3 \\ c_4 \end{bmatrix} = \begin{bmatrix} \partial\Theta_B/\partial n \\ \Theta_2 \\ \Theta_3 \\ \Theta_4 \end{bmatrix}. \tag{3.22}$$

An extensive description of the algorithm is available in the work by Vanna et al. [85], and validation of the present implementation is available in Appendix 3.5 and in the paper by Modesti et al. [87].

3.5 Verfication

3.5.1 Verification of Numerical Method

The numerical setup has been validated by reproducing the results of Lee and Moser [83], who performed DNS of turbulent channel flows at a range of friction Reynolds numbers. We reproduced the simulation at friction Reynolds number $Re_\tau = 550$ with the same box size of $L_x \times L_y \times L_z = 8\pi\delta \times 2\delta \times 3\pi\delta$ with grid size $N_x \times N_y \times N_z = 800 \times 250 \times 68$. Figure 3.3 shows a comparison of the mean streamwise velocity and the Reynolds stresses. Perfect agreement is observed between the DNS of Lee and Moser [83] and the present data, confirming the accuracy of the numerical method.

3.5.2 Immersed Boundary: Comparison with Spanwise-Invariant Roughness

The immersed boundary method has been validated by reproducing the results of MacDonald et al. [19], who performed DNS of open channel flow over spanwise-aligned bars using a body-fitted solver. We reproduced this configuration by simulating the flow over the same roughness geometry, matching the viscous-scaled spacing in the streamwise direction $s^+ = 200$, the roughness height $k^+ = 50$, and the friction Reynolds number $Re_\tau \approx 395$, using grid size $N_x \times N_y \times N_z = 800 \times 250 \times 68$. Figure 3.4 shows a comparison of the mean streamwise velocity and the Reynolds stresses. Perfect agreement is observed between the DNS of MacDonald et al. [19] and the present data, confirming the accuracy of our immersed boundary method.

3.5.3 Grid convergence

We performed a grid convergence study to ascertain the number of points required to resolve acoustic liner geometry. The grid convergence is performed on flow case $L\text{-}L_{32}$, introduced later in chapter 4. Flow case $L\text{-}L_{32}$ represents an acoustic liner with diameter $d = 0.08\delta$, thickness, $t/d = 1$ and porosity, $\sigma \approx 0.32$. The grid used for flow case has 40 points per orifice. Flow case $L\text{-}L_{32}$ has also been simulated using a coarser mesh with 26 grid points per orifice in the wall-parallel directions. Figure 3.5 shows a comparison of the mean streamwise velocity and the Reynolds stresses for the two different grid spacings. The results between the two grids are identical, indicating that 26 mesh points per orifice are already sufficient to achieve grid independence.

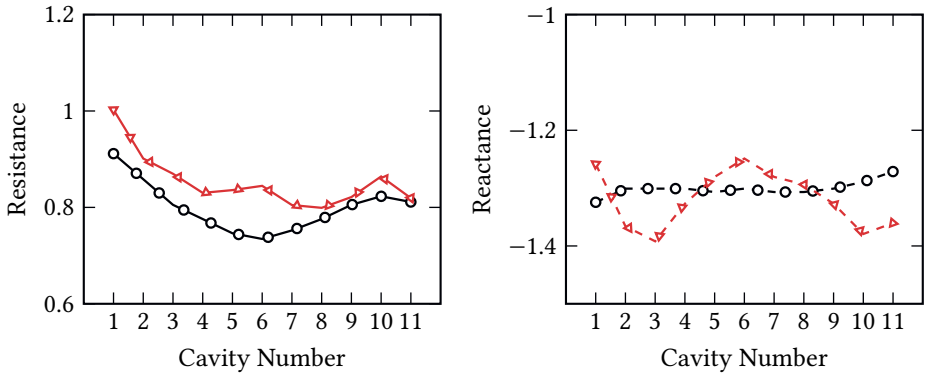

Figure 3.6: Comparison of the resistance (a) and reactance (b) with the simulations of Schroeder et al. [88] for incoming sound waves with a frequency $f = 800$Hz and SPL$= 150dB$. Circles represent simulations of Schroeder et al. [88] and triangles represent the current simulations.

3.5.4 Introduction of Sound Waves: Impedance of Acoustic Liner Array

The introduction of sound waves is validated by reproducing the results of Schroeder et al. [88], who performed multi-orifice simulations of an acoustic liner array with multiple holes. Simulations are done without flow and soundwaves are introduced into the domain using the characteristic relaxation boundary condition, as in the boundary layer flow case. Sound waves with a frequency $f = 800$Hz and SPL$= 150dB$ are introduced. A comparison of the resistance and reactance of the corresponding acoustic liner array is shown in figure 3.6. Although differences are observed between the reference data and our current simulation, these can, in part, be chalked down to the different way in which the sound wave is introduced into the domain and the slightly different geometry of the acoustic liner, which was approximated in our current simulation. The trends of the resistance and reactance, however, match well with the reference data.

4

Channel Flow Simulations

Parts of this chapter have been published in J. Fluid Mech. 965, A10 and Flow Turb. Combust. 109 (4), 1241-1254.

We begin our analysis of acoustic liner geometries with our channel flow simulations. Acoustic liner geometries cover a large parameter space. The diameter of the orifice, the length, breadth and depth of the cavity along with its shape, and the local boundary layer properties are only some of the variables that could influence its behaviour. To make the problem more tractable, we restrict the parameter space so we match, approximately, the diameter of acoustic liners with respect to the boundary layer length scales, to study these liners in flow conditions that are representative of actual conditions that will be encountered in real flight. The following sections detail the cases studied, highlight the geometric parameters considered, and elaborate upon the aerodynamic performance of acoustic liner-type permeable surfaces.

4.1 Methodology

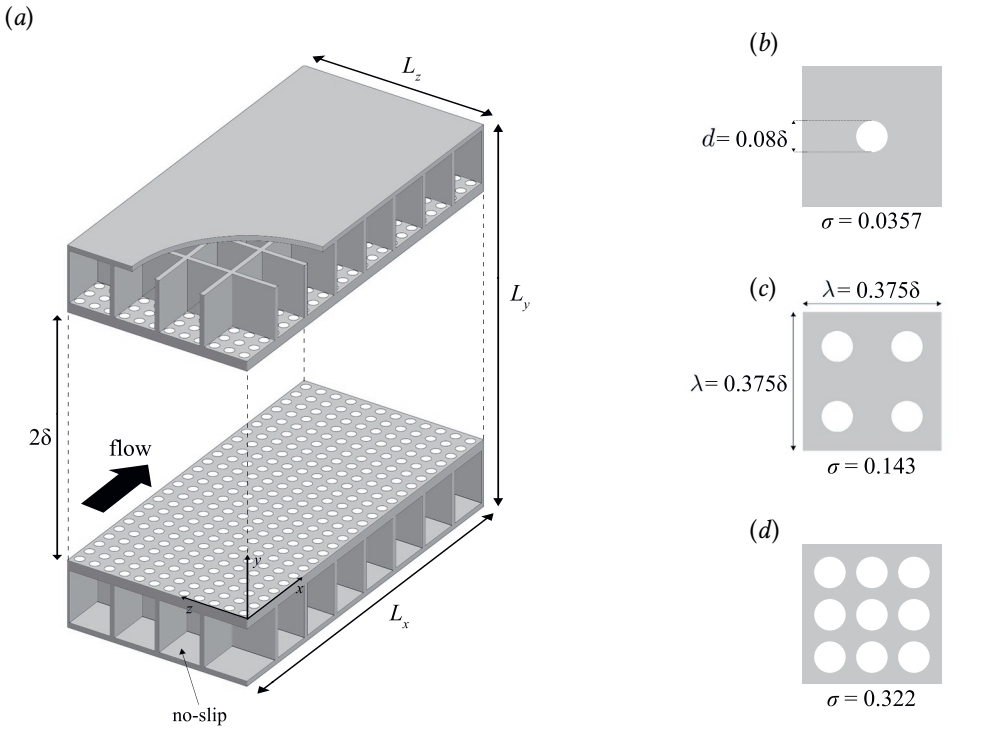

Figure 4.1: Sketch of the computational domain. Turbulent channel flow configuration with box dimension $L_x \times L_y \times L_z$. Different porosities are considered by increasing the number of holes per cavity. The three different porosities, σ are shown on the right.

The simulations are carried out in a rectangular box of size $L_x \times L_y \times L_z = 3\delta \times 2(\delta + h) \times 1.5\delta$, where δ is the channel half-width. This box size is smaller than is usually recommended for DNS [89]. However, similar and even smaller box sizes have been used previously to aid parametric analysis of rough wall turbulent flows [90, 91, 92, 93] through

	Re_b	Re_τ	d^+	σ	$\sqrt{K_y}^+$	$1/\alpha_y^+$	ΔU^+	$C_f \times 10^3$	Δx^+	Δy^+_{min}	Δz^+	N_x	N_y	N_z	ℓ_T^+	$T_{\text{av}} u_\tau/\delta$
S-L	9268	506.1	0	0	0	0	-	4.578	5.1	0.80	5.1	300	350	150	0.00	37.8
S-M	21180	1048	0	0	0	0	-	3.791	5.2	0.80	5.2	600	600	300	0.00	40.9
S-H	45240	2060	0	0	0	0	-	3.201	5.2	0.80	5.2	1200	800	600	0.00	45.8
L-L_3	9139	503.5	40.3	0.0357	1.04	0.0528	0.14	4.598	1.1	0.80	1.1	1500	500	750	0.20	24.0
L_t-L_3	9139	505.3	40.4	0.0357	0.937	0.0287	0.17	4.738	1.5	0.81	1.5	1000	500	500	0.25	22.3
L-L_{14}	8794	496.4	39.7	0.142	2.06	0.859	0.56	4.855	1.0	0.80	1.0	1500	500	750	1.00	32.8
L_t-L_{14}	8794	515.5	41.2	0.142	1.92	0.552	0.69	4.856	1.6	0.82	1.6	1000	500	500	1.10	26.1
L-L_{32}	8264	505.3	40.4	0.322	3.22	5.14	1.90	5.539	1.0	0.81	1.0	1500	500	750	2.75	17.6
L-M_{14}	19505	1038	83.0	0.142	4.30	1.727	0.96	4.363	2.1	0.83	2.1	1500	800	750	1.00	25.2
L_t-M_{14}	19505	1047	83.8	0.142	3.90	1.120	1.40	4.475	3.1	0.84	3.1	1000	800	500	1.25	29.6
L-M_{32}	17810	1026	82.1	0.322	6.53	10.4	2.78	5.058	2.1	0.82	2.1	1500	800	750	3.75	30.7
L_t-M_{32}	17810	1055	84.4	0.322	5.95	6.692	3.28	5.317	3.1	0.84	3.2	1000	800	500	4.00	24.2
L-H_{32}	35470	2044	164.0	0.322	13.0	20.8	4.44	5.267	4.1	0.82	4.1	1500	1400	750	5.00	32.3

Table 4.1: DNS dataset comprising smooth (S-Re) and liner (L-$Re_{\sigma(\%)}$ and L_t-$Re_{\sigma(\%)}$) cases where $Re = \{L, M, H\}$ correspond to the three Reynolds numbers $Re \approx 500$ (Low), $Re \approx 1000$ (Medium), and $Re \approx 2000$ (High) and σ is the porosity of the liner case. Cases L_t-$Re_{\sigma(\%)}$ have plate thickness $t/d = 0.5$ and flow cases L-$Re_{\sigma(\%)}$ have $t/d = 1$, where d is the orifice diameter. K_y and α_y are the Darcy and Forchheimer wall-normal permeabilities. ΔU^+ is the Hama roughness function measured at $y^+ + \ell_T^+ = 100$, where ℓ_T is the virtual origin shift. $C_f = 2/u_\delta^{+2}$ is the skin-friction coefficient, where u_δ^+ is the viscous-scaled streamwise velocity at the channel centerline. Simulations are performed in a computational box with dimensions $L_x \times L_y \times L_z = 3\delta \times 2(\delta + h) \times 1.5\delta$. Δx^+ and Δz^+ are the viscous-scaled mesh spacing in the streamwise and spanwise direction, and Δy^+_{min} is the minimum mesh spacing in the wall-normal direction. $T_{\text{av}} u_\tau/\delta$ is the time averaging interval.

comparison with smooth wall simulations with the same box size. We use uniform mesh spacing in the streamwise and spanwise directions. In the wall-normal direction, the mesh is clustered towards the facesheet walls and coarsened towards the backplate and the channel centre. The simulations are performed at bulk Mach number, $M_b = u_b/c_w = 0.3$, where c_w is the speed of sound at the wall. This value of Mach number is representative of the values encountered inside aircraft air intakes, where the flow is decelerated before reaching the fan. We also note that at this Mach number and in the absence of incoming acoustic waves, we do not expect significant compressibility effects, as the friction Mach number does not exceed $M_\tau = u_\tau/c_w < 0.02$ for any of the flow cases. The bulk-to-wall temperature ratio is fixed $T_b/T_w = 1$, which corresponds to an isothermal cold wall with $T_w/T_{aw} = 0.984$, where T_{aw} is the adiabatic wall temperature based on the bulk Mach number.

We choose the liner geometry to match as closely as possible the orifice size of acoustic liners in operating conditions. The acoustic liner comprises a total of 64 cavities: an array of 8×4 in the streamwise and spanwise direction on the upper and lower wall. Each cavity has a square cross-section with a side length $\lambda_c = 0.335\delta$, depth $h = 0.5\delta$. The orifices have a diameter of $d = 0.08\delta$, the cavity walls have a thickness of 0.02δ.

We carry out simulations at three friction Reynolds numbers $Re_\tau = 500, 1000, 2000$, corresponding to a viscous-scaled diameters $d^+ = 40, 80, 160$. Additionally, we increase the liner porosity between $\sigma \approx 0.036$–0.32 by varying the number of orifices per cavity between 1 and 9. We also vary the facesheet thickness. The dataset is complemented by smooth wall simulations at approximately matching friction Reynolds numbers. Flow cases are named with the letter S-Re or L-$Re_{\sigma(\%)}$, depending on if they are smooth wall (S) or liner configurations (L), followed by the Reynolds number, low (L) for $Re_\tau \approx 500$, medium (M) for $Re_\tau \approx 1000$ and high (H) for $Re_\tau \approx 2000$. For liner cases, $\sigma(\%)$ is the facesheet porosity, expressed as a percentage. The naming convention of the liner cases also contains information about the thickness of the facesheet. Cases L-$Re_{\sigma(\%)}$ have a facesheet thickness of $t = d$ and cases L_t-$Re_{\sigma(\%)}$ have a facesheet thickness of $t = d/2$. For example, flow case $L-M_{32}$ indicates a liner flow case at $Re_\tau \approx 1000$ with facesheet thickness $t/d = 1$ and a porosity of 32%. Details of all flow cases are reported in table 4.1. The same wall-normal mesh is employed for cases with thickness $t = d$ and $t = d/2$. This ensures that, at a minimum, 25 grid points are used to resolve the facesheet thickness at $Re_\tau = 500$ and $t = d/2$. Note that whereas 40 points are used to resolve the orifice diameter in the streamwise and spanwise direction for cases with $t = d$, and 26 points are used for flow cases with $t = d/2$. This resolution is well within the viscous spacing typically accepted in DNS, and it does not affect the results, as we show in the mesh refinement study detailed in 3.5.3. The orifice configurations within a cavity, along with a sketch of the entire domain, are shown in figure 4.1. We compare the results of the liner simulations with smooth-wall simulations at approximately matching friction Reynolds numbers. Quantities that are non-dimensionalised by δ_v and u_τ are denoted by the '+' superscript.

The near-wall flow is spatially inhomogeneous due to the acoustic liner. Therefore, flow statistics are calculated by averaging in time and over the cavity phase $\lambda = 0.375\delta$ in the streamwise and spanwise direction, both using Favre ($\widetilde{\cdot}$) and Reynolds ($\overline{\cdot}$) ensemble averages,

$$f(x,y,z,t) = \widetilde{f}(x,y,z) + f''(x,y,z,t), \quad f(x,y,z,t) = \overline{f}(x,y,z) + f'(x,y,z,t). \tag{4.1}$$

Additionally, we use angle brackets $\langle\cdot\rangle$ to denote intrinsic averages (average over the fluid only) in the wall-parallel directions. With this notation, the ensemble-averaged Reynolds stress tensor is $\tau_{ij}(x,y,z) = \overline{\rho u_i'' u_j''}$. The wall-normal coordinate is measured upwards from the surface of the facesheet such that $y/\delta = -h$ corresponds to the bottom surface of the cavity. For comparing the smooth wall and the liner cases, a virtual origin shift ℓ_T is also introduced. The virtual origin is measured positively downwards from the surface of the facesheet. More details about the virtual origin are provided in section 4.2.3.

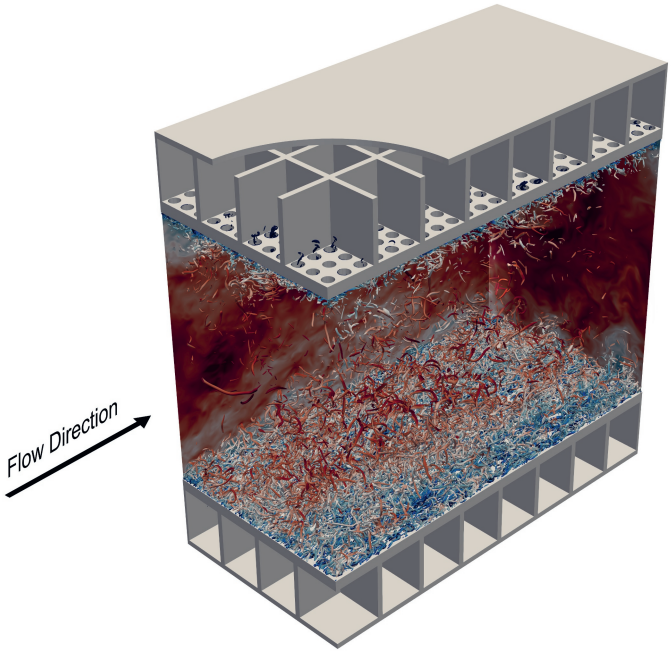

Figure 4.2: Instantaneous flow field from DNS of turbulent channel flow at $Re_\tau = 2000$ and bulk Mach number $M_b = 0.3$. The streamwise velocity is shown in an $x-y$ plane, and a $y-z$ plane. Vortical structures are visualised using the Q-Criterion.

4.2 Flow over Acoustic Liners

4.2.1 Instantaneous Flow

We begin our analysis by inspecting an instantaneous visualisation of flow case $L\text{-}H_{32}$ at friction Reynolds number $Re_\tau = 2000$. Figure 4.2 shows the streamwise velocity in the wall-normal planes and vortical structures visualised using the Q-Criterion. The near-wall region is populated by small-scale structures indicating intense turbulence activity close to the wall, whereas the flow below the cavities is more quiescent, although some vortices penetrate below the facesheet.

Figure 4.3 shows contours of the instantaneous streamwise (*a*, *b*) and wall-normal (*c*, *d*) velocity, in a wall-parallel plane above the facesheet for flow case $L\text{-}H_{32}$. The streamwise

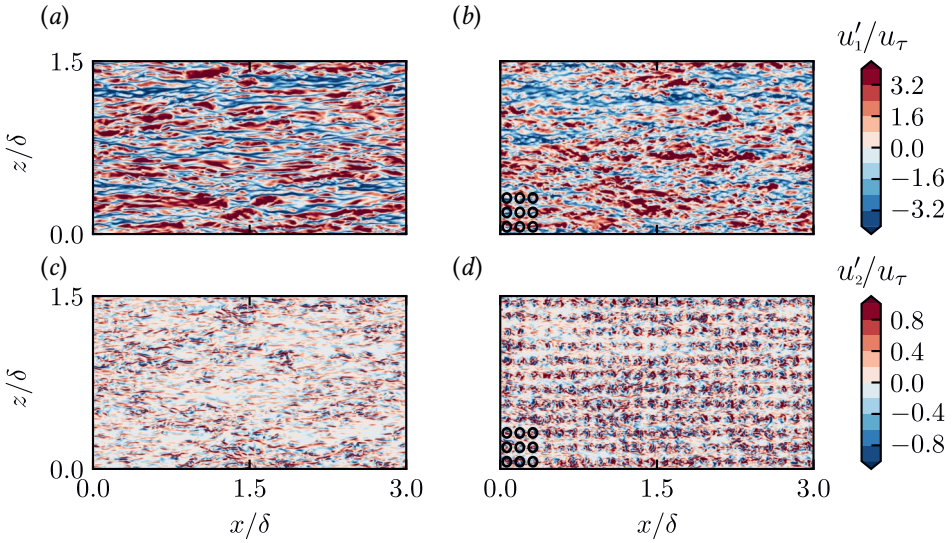

Figure 4.3: Instantaneous streamwise (*a*, *b*) and wall-normal (*c*, *d*) velocity fluctuations in an $x-z$ plane at $y^+ + \ell_T^+ = 12$ for flow case *S-H* (*a*, *c*) and flow case *L-H*$_{32}$ (*b*, *d*) at $Re_\tau \approx 2000$. The position of the orifices is shown at the bottom left corner, for one cavity only. The virtual origin ℓ_T is defined in section 4.2.3.

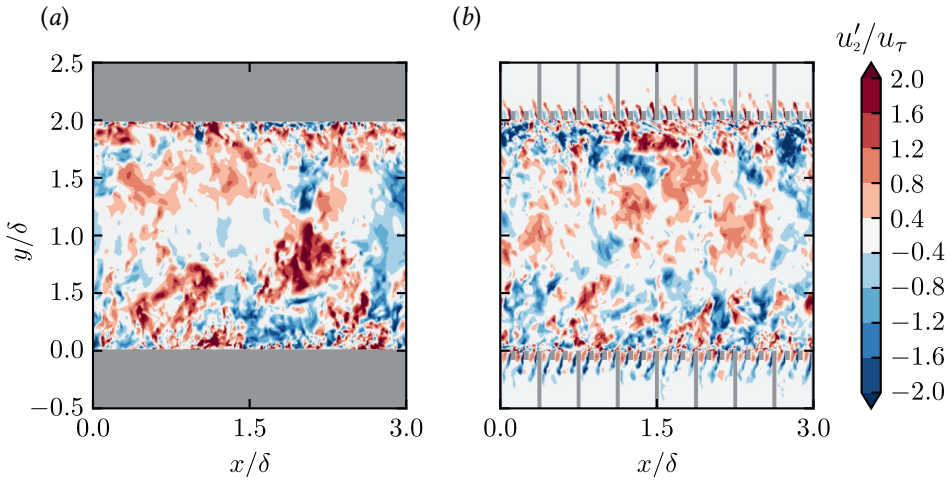

Figure 4.4: Wall-normal velocity fluctuations in an $x-y$ plane at for flow case *S-H* (*a*) and flow case *L-H*$_{32}$ (*b*) at $Re_\tau \approx 2000$. Grey patches represent solid wall regions.

velocity is significantly altered as compared to the smooth wall and near-wall streaks are shorter over the liner. A similar break-up of the streaks was also observed by Orlandi and Leonardi [94] for different roughness geometries. Here, the streaky structures can still be discerned, suggesting a modification, rather than a complete replacement of the near-wall cycle.

These observations are in line with previous studies on permeable walls, which reported shorter streaks caused by the higher wall-normal velocity fluctuations [95]. We also observe higher wall-normal velocity fluctuations as compared to the smooth wall, mainly concentrated at the orifices, figure 4.3. The wall-normal velocity fluctuations seem reminiscent of the underlying surface pattern, as the position of the orifices can easily be discerned in the contours of u_2', suggesting that turbulence in the near-wall region is modulated by the surface topography [96].

Figure 4.4 shows a snapshot of the wall-normal velocity in an $x-y$ plane, where we observe that the effect of the liner on the flow is concentrated near the wall and inside the cavities. Inside the orifices, high wall-normal velocity fluctuations are visible, and they are notably higher at the downstream edge. Wall-normal velocity fluctuations penetrate inside the cavities forming a jet-like flow which extends down to 0.2δ below the facesheet, indicating important inertial effects inside the orifices.

4.2.2 Mean Flow

In order to quantify the flow penetration and inertial effects inside the orifices, we report the mean wall-normal velocity, wall-normal Reynolds stress component for liner flow cases with $t = d$ in figure 4.5. Away from the facesheet, the flow is homogeneous in the wall-parallel directions, indicating that the effect of the liner is primarily contained in the near-wall region. The mean flow is highly three-dimensional close to the liner. The wall-normal velocity is negative at the downstream edge of the orifice, suggesting that flow penetrates inside the orifices, and positive at the upstream edge due to the mean flow recirculation inside the pore, separating the region above and below the facesheet. The vortex is asymmetric, and the negative values of $\widetilde{u}_2$ are always higher than the positive ones. Moreover, we note that the intensity of $\widetilde{u}_2$ is, primarily, a function of the viscous-scaled orifice diameter, whereas it seems less dependent on the porosity of the plate.

For sufficiently large d^+, we observe high values of the wall-normal velocity extending down into the cavity, resembling a jet-like flow also observed in the instantaneous flow in figure 4.4. This jet-like mean flow is accompanied by high wall-normal velocity fluctuations inside the orifice, as shown in figures 4.5 (g)–(l). Also the wall-normal velocity fluctuations τ_{22} are higher at the downstream edge of the orifice, where they reach values comparable to, or even higher than, the peak in the near-wall cycle. This is particularly true for liner cases L-M_{32} and L-H_{32} (figures 4.5 (k), (l)) where τ_{22} is higher below the facesheet than in the near-wall cycle above the facesheet. These high wall-normal velocity fluctuations are a symptom of inertial effects inside the orifices. A comparison between liner flow cases with $t = d$ indicates that τ_{22} seems to depend on both σ and d^+.

We also investigate the effect of the plate thickness, using flow cases L_t-L_{14}, L_t-M_{14} and L_t-M_{32}, which have $t = 0.5d$. Reducing the thickness causes an increase of the mean wall-normal velocity (compare figure 4.5 (e) to 4.6 (c)) and its fluctuations (compare figure 4.5 (k) to 4.6 (f)) within the orifice. Wall-normal velocity fluctuations have been correlated

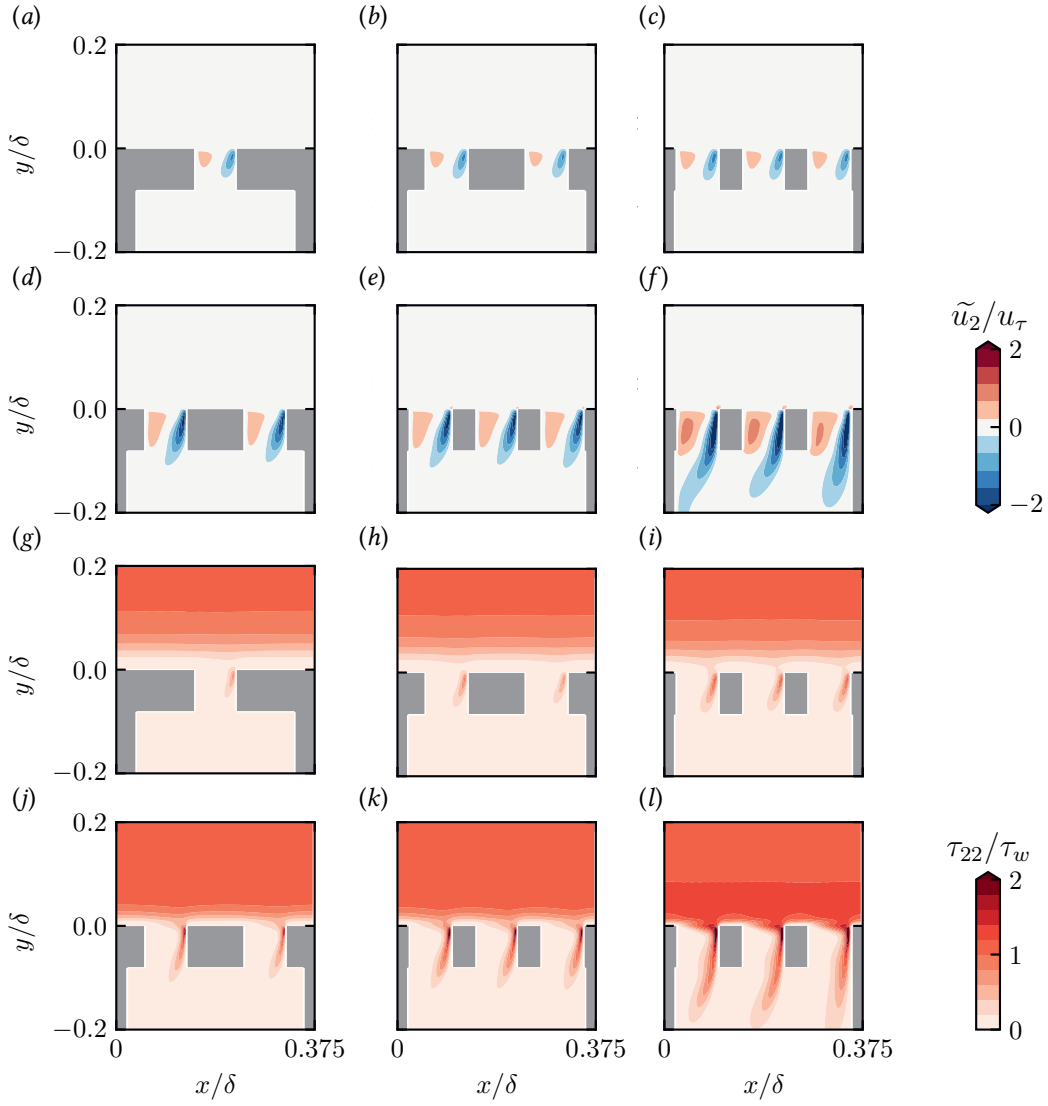

Figure 4.5: Mean wall-normal velocity $\widetilde{u}_2$ (*a*)–(*f*) and wall-normal Reynolds stress τ_{22} (*g*)–(*l*) over a liner cavity for flow cases *L*-L_3 (*a*, *g*), *L*-L_{14} (*b*, *h*), *L*-L_{32} (*c*, *i*), *L*-M_{14} (*d*, *j*), *L*-M_{32} (*e*, *k*) and *L*-H_{32} (*f*, *l*).

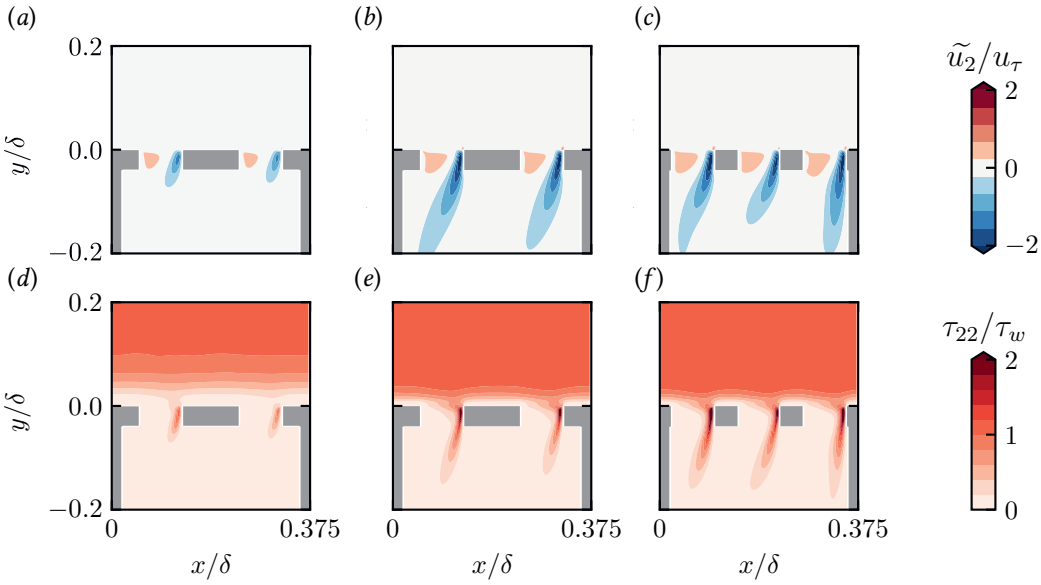

Figure 4.6: Mean wall-normal velocity $\widetilde{u}_2$ (*a*)–(*c*) and wall-normal Reynolds stress τ_{22} (*d*)–(*f*) over a liner cavity for flow cases L_t-L_{14} (*a*, *d*) L_t-M_{14} (*b*, *e*) L_t-M_{32} (*c*, *f*).

with drag increase over rough surfaces [97] as they are indicative of momentum transfer between the the crest and the trough in the case of roughness, and the regions above and below the facesheet for acoustic liners. Therefore, this qualitative analysis suggests that the added drag over acoustic liners might depend on d^+, σ and t/d, as we discuss further in the following section.

4.2.3 Virtual Origin and Drag Increase

On smooth walls, there is no ambiguity on the wall-normal origin of the flow, which is always at the wall, where both the mean velocity and Reynolds stresses are zero. The presence of complex surface patterns introduces uncertainty on the wall-normal origin location, which can be relevant when comparing rough wall results to the solution for a corresponding smooth wall.

This virtual origin is a flow property, and it can be interpreted as the wall-normal location where the outer flow perceives the wall. Several methods to estimate the virtual origin have been proposed [98, 18, 22]. In the present work, we calculate the origin of turbulence ℓ_T following the approach of Ibrahim et al. [99], namely we shift the Reynolds shear stress profile of the liner cases to match the smooth wall one. The virtual origin is located ℓ_T below the surface of the facesheet (figure 4.7), meaning that the near-wall cycle tends to penetrate inside the orifices, as is also clear from the high values of the Reynolds shear stress in figure 4.8 (*a*), and from instantaneous flow visualizations. The virtual origin shift is limited to a few wall units $\ell_T^+ \leq 5$ for all flow cases, but accounting for this displacement allows us to restore a very good match with the smooth wall data down

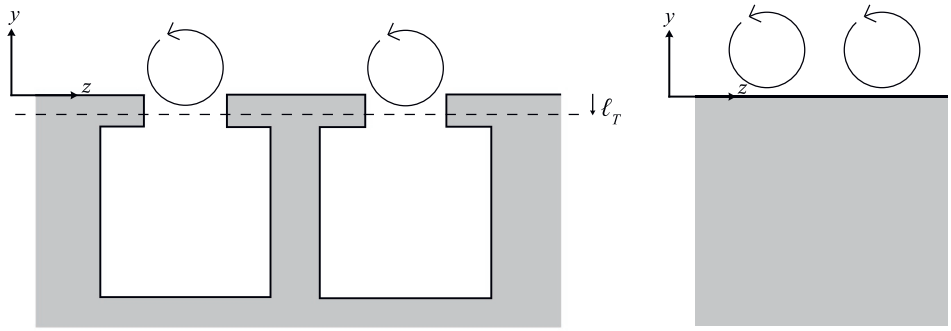

Figure 4.7: Schematic depicting the virtual origin of the flow configuration.

to the viscous sublayer (figure 4.8 (*b*)), confirming that at least part of the effect of the liner can be accounted for by an origin shift.

Having estimated the virtual origin, we can now draw meaningful comparisons between the smooth wall and liner statistics. Figure 4.9 shows the mean velocity profiles in viscous units for all flow cases. The mean velocity profiles over the liner show a downward shift ΔU^+ with the respect to the baseline smooth wall, indicating that the flow experiences higher drag. Despite the shift, velocity profiles are parallel to each other, which supports outer-layer similarity, as is typical of many rough surfaces [100]. The von Kármán constant is $\kappa \approx 0.39$ for both liner and smooth wall cases.

This is in contrast to the work of Breugem et al. [39] and Kuwata and Suga [101], who reported different values of κ over permeable surfaces. The discrepancy could be due to the low-Reynolds number of previous studies (maximum $Re_\tau \approx 350$ for smooth impermeable cases), or perhaps to the use of Darcy-type boundary conditions, as compared to pore-resolved simulations. The flow cases with low porosity, $\sigma = 0.0357$ and $d^+ = 40$ (circles), show a smooth-wall-like behaviour with very minor changes in the mean velocity profile. However, a departure from the smooth-wall velocity profile becomes evident as either σ or d^+ is increased or t/d is decreased.

A fundamental question is whether acoustic liners exhibit a fully rough regime, namely, whether the Hama roughness function follows a logarithmic law,

$$\Delta U^+ = \frac{1}{\kappa}\log(\ell^+) + B(\ell^+), \tag{4.2}$$

where ℓ is a suitable length scale of the liner geometry. In canonical k-type roughness, ℓ is simply the roughness height, however, for acoustic liners different choices are possible. Unlike canonical roughness, there is no protrusion into the flow and therefore the definition of a suitable length scale is not straightforward. It is clear that it depends upon the geometrical parameters of the orifice, namely the porosity, orifice diameter and plate thickness. However, as is apparent in figure 4.10 (*a*), none of these parameters can account for the effect of the liner on their own. For instance, flow cases *L*-L_{14} and *L*-L_{32} have the same t/d and approximately the same d^+, but different porosity and therefore a different ΔU^+. Similarly, cases *L*-L_{32} and *L*-M_{32} have the same porosity and t/d, but case *L*-M_{32} has

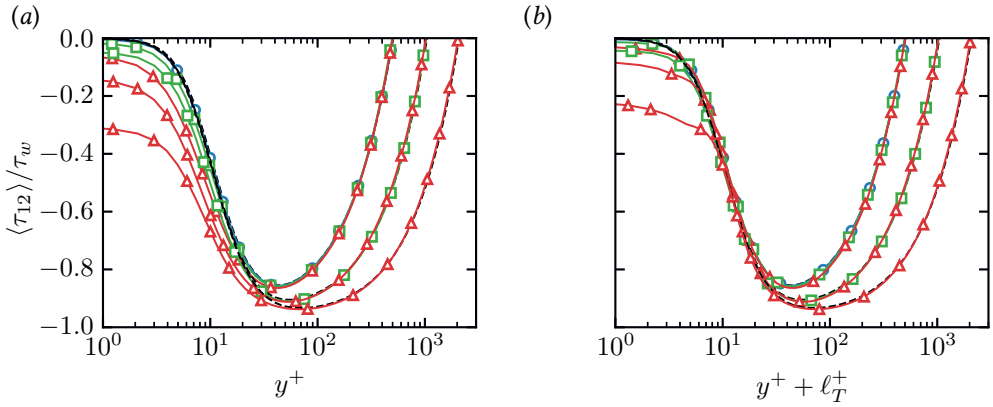

Figure 4.8: Intrinsic averaged Reynolds shear stress $\langle \tau_{12} \rangle$ as a function of the wall-normal distance for smooth wall flow cases with $t = d$ (dashed) and liner flow cases (solid with symbols), before virtual origin correction (*a*) and after virtual origin correction (*b*). Symbols indicate different porosities: $\sigma = 0.0357$ (blue circles), $\sigma = 0.143$ (green squares) and $\sigma = 0.322$ (red triangles).

a larger viscous scaled diameter, leading to a larger ΔU^+, see table 4.1. An increase in ΔU^+ is also noted if the thickness is decreased and the other two parameters are constant.

Other candidate length scales can be inferred by regarding acoustic liners as porous surfaces. The flow normal to a porous plate is characterized by the pressure drop through the facesheet ΔP, which can be expressed as the sum of two contributions [48, 102],

$$\frac{\Delta P}{t} \frac{d^2}{\rho \nu U_t} = \frac{d^2}{K_y} + \sigma \alpha_y d Re_p. \tag{4.3}$$

The Darcy permeability has the physical dimension of an area whereas the Forchheimer coefficient is the inverse of a length scale, and they are both related to the ease with which the flow passes through the plate because both contribute to the pressure drop. Their relative importance depends on Re_p: Darcy permeability dominates at low pore Reynolds number ($Re_p \leq \mathcal{O}(1)$), whereas the Forchheimer permeability becomes relevant from $Re_p \gtrsim 5$. The permeability coefficients are measured by simulating a laminar flow in the direction perpendicular to the facesheet for a single cavity and measuring the pressure drop as a function of the mass flow rate through the porous medium. Different mass flow rates have been simulated, which allows us to estimate the permeability coefficients of the Darcy–Forchheimer law. More details and an extensive discussion on Darcy and Forchheimer drag is available in the addendum at the end of the chapter, where we calculate the Darcy permeability and the Forchheimer coefficient of perforated plates that match the present DNS dataset and compare the results to available engineering formulas.

If we regard acoustic liners as porous surfaces, two relevant length scales for the flow are the square root of the Darcy permeability, $\sqrt{K_y}$ and the inverse of the Forchheimer coefficient, $1/\alpha_y$, besides the orifice diameter. We show ΔU^+ as a function of the viscous-scaled orifice diameter and the square root of the wall-normal Darcy permeability in figure 4.10. Data show that neither the orifice diameter nor the square root of the Darcy permeability

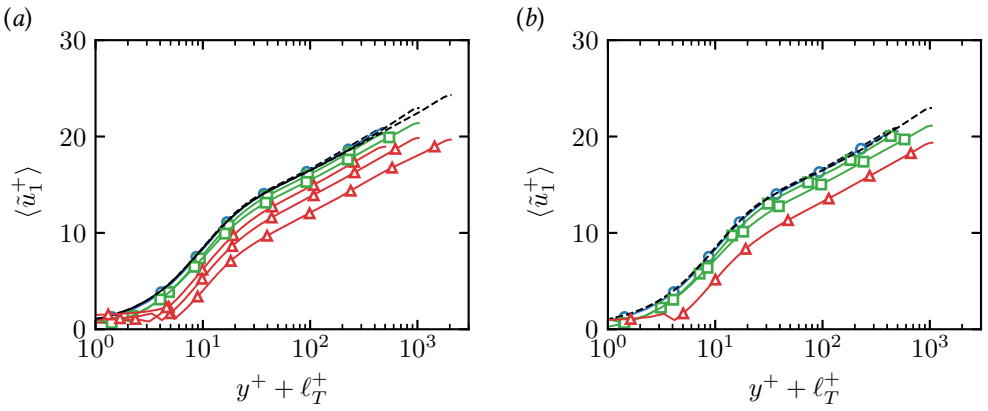

Figure 4.9: Intrinsic averaged mean streamwise velocity for smooth wall flow cases (Dashed lines) and liner flow cases with $t = d$ (*a*) and $t = d/2$ (*b*) as a function of the wall-normal distance. Symbols indicate different porosities: $\sigma = 0.0357$ (blue circles), $\sigma = 0.143$ (green squares) and $\sigma = 0.322$ (red triangles).

are suitable length scales for predicting the drag increase, as we find a clear non-monotonic trend, see figure 4.10. Instead, we find that ΔU^+ shows a very promising trend when reported as a function of the inverse of the viscous-scaled Forchheimer coefficient, suggesting that $1/\alpha_y^+$ is the most appropriate length scale for characterising the additional drag, figure 4.11.

This is consistent with the importance of inertia due to the very high wall-normal velocity fluctuations experienced inside the orifice, as observed in figure 4.5. Hence, the Darcy permeability, which is commonly associated with the pressure drop in the limit case of Stokes flow, is no longer the dominant term. This is further elaborated upon in Section 4.2.4. Additional supportive evidence that $1/\alpha_y$ is the relevant length scale is provided by figure 4.11 (*b*), showing a nearly linear relation between the inverse of the Forchheimer coefficient and the roughness sublayer. The roughness sublayer is defined as the wall-normal location, measured upwards from the virtual origin, where the time-averaged flow becomes homogeneous in the wall-parallel directions [100]. It is a measure of the wall-normal extension of the liner influence, and has been correlated often with the relevant roughness length scale [103, 104, 22].

Moreover, the data in figure 4.11 (*a*) show good agreement with data for classical sand-grain roughness of Nikuradse [13], supporting the emergence of a fully rough regime,

$$\Delta U^+(1/\alpha_y^+) = \frac{1}{\kappa}\log(1/\alpha_y^+) + C. \tag{4.4}$$

with $C \approx -3.5$.

For $t/d = 1$, our data match very well the sand-grain roughness of Nikuradse [13] with $k_s^+ \approx 1/\alpha_y^+$ being the equivalent sand-grain roughness height. For flow cases with a lower plate thickness $t/d = 0.5$, we observe a similar trend, although the fully rough regime is not reached, and flow cases at higher $1/\alpha_y^+$ would be necessary to determine k_s^+ more accurately.

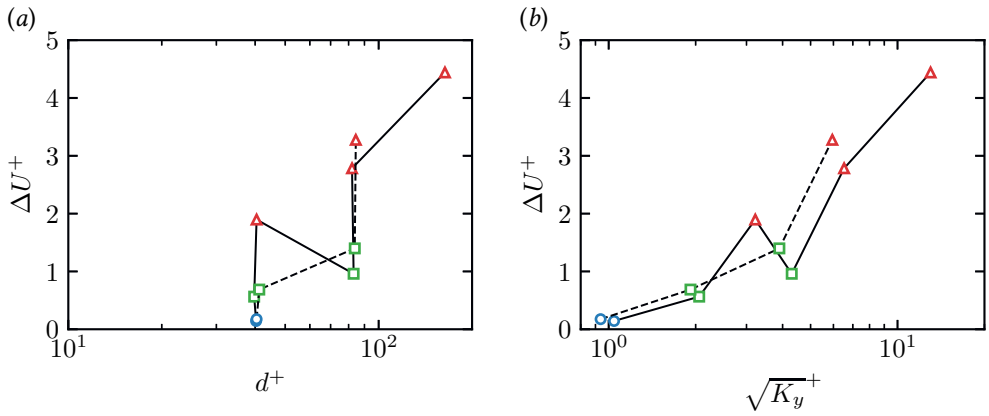

Figure 4.10: ΔU^+ as a function of the viscous-scaled orifice diameter, d^+ (*a*) and the Darcy permeability (*b*). Different line types indicate different facesheet thicknesses: solid ($t = d$) and dashed ($t = d/2$). Symbols indicate different porosities: $\sigma = 0.0357$ (blue circles), $\sigma = 0.143$ (green squares) and $\sigma = 0.322$ (red triangles).

The existence of a fully rough regime is in line with the observations of Esteban et al. [40], who note a fully rough regime in their experiments over porous foams, however, they noted that, the relevant length scale was the square root of the Darcy permeability.

The fully rough regime is usually associated with the dominance of pressure drag over viscous drag, and the same appears to hold for acoustic liners. In table 4.2 we report the friction coefficient, decomposed into its viscous and pressure contribution, which shows that pressure drag is nearly negligible for flow case *L*-L_3, whereas it becomes comparable to viscous drag for flow case *L*-H_{32}. The same trend is also observed for cases with lower plate thickness. Even though pressure drag is still contributing for less than 50% for flow case *L*-H_{32}, we believe that the trend is rather clear and it supports the emergence of a fully rough regime for acoustic liners.

The relevance of pressure drag can also be demonstrated by analysing the mean momentum balance in the streamwise direction,

$$\frac{\partial \overline{\rho}\widetilde{u}_1\widetilde{u}_j}{\partial x_j} + \frac{\partial \overline{\rho}\widetilde{u_1''u_j''}}{\partial x_j} = -\frac{\partial \overline{p}}{\partial x_1} + \frac{\partial \widetilde{\sigma}_{1j}}{\partial x_j} + \overline{\Pi}. \tag{4.5}$$

Figure 4.12 shows the contribution of the different terms in equation (4.5), close to the orifice. Viscous diffusion becomes less relevant as the Reynolds number increases, whereas the intensity of turbulent convection increases, although the maximum value is confined very close to the wall, and inside the orifices. The magnitude of the pressure gradient term is constant for all considered Reynolds numbers, and its maximum location shifts downward into the orifices as the Reynolds number increases. The figure shows that the contribution of the pressure gradient is significant and its relative importance grows as the viscous sublayer becomes thinner. We also note that increasing the number of holes (porosity) increases the pressure drag, as each orifice seem to contribute approximately the same, independently of its location.

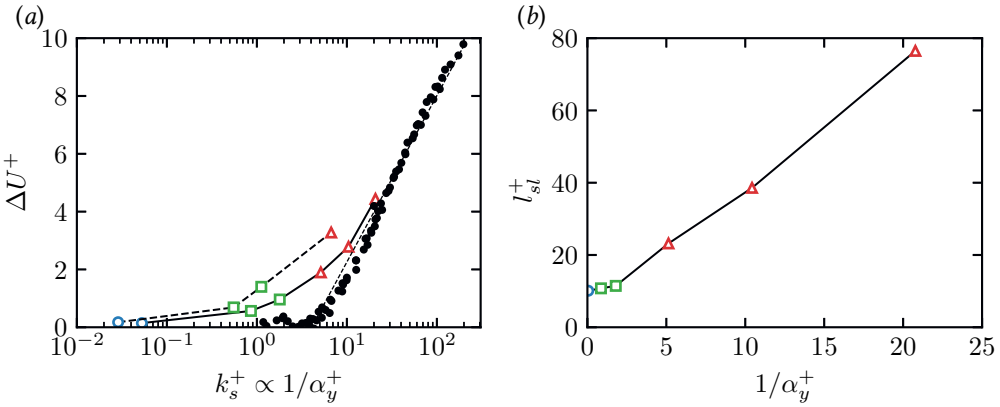

Figure 4.11: ΔU^+ (*a*) and the roughness sublayer height (*b*) as a function of the inverse of the Forchheimer coefficient, $1/\alpha_y^+$. Different line types indicate different facesheet thicknesses: Solid ($t = d$) and thick dashed ($t = d/2$). The thin dashed line in (*a*) indicates $\Delta U^+ = \kappa^{-1}\log(1/\alpha_y^+) - 3.5$. Symbols indicate different porosities: $\sigma = 0.0357$ (blue circles), $\sigma = 0.143$ (green squares) and $\sigma = 0.322$ (red triangles). The black filled circles indicate Nikuradse's data [13].

The values of the friction coefficient reported in table 4.2 only apply to the Reynolds number of the present DNS, which is much lower than in a realistic configuration. Fortunately, the existence of a fully rough regime simplifies the modelling of acoustic liners and makes it easy to estimate the drag increase they induce in operating conditions. As discussed in Section 2.2.2, the friction Reynolds number over acoustic liners is $Re_\tau \approx 5400$, and the viscous-scaled inverse of the Forchhemeir coefficient for a geometry with $d/\delta \approx 0.08$, $t/d \approx 1$ and $\sigma \approx 0.3$ is $1/\alpha_y^+ \approx 55$, see Addendum at the end of this chapter. Assuming that a fully rough regime exists, then equation (4.4) returns $\Delta U^+ \approx 6.5$, which can be converted into drag variation [22],

$$\Delta\text{Drag}(\%) = \frac{1}{\left(1 - \dfrac{\Delta U^+}{u_{\infty,s}^+}\right)^2} - 1, \tag{4.6}$$

Hence, acoustic liners, in operating conditions, are expected to provide about 70% drag increase per plane area with respect to a smooth wall. Of course, this value might slightly change depending on the specific geometry considered, and the presence of incoming acoustic waves could also alter this result.

4.2.4 Permeability and Velocity Fluctuations

We further analyse the effect of acoustic liners on the Reynolds stresses, see figure 4.13. Differences with respect to the smooth wall are primarily observed near the wall and increase as the permeability increases. The relaxed impermeability condition gives rise to non-zero Reynolds stresses at the liner wall, thus enhancing momentum transfer between the flow above and below the plate. The peak of the Reynolds stresses is also modified. The

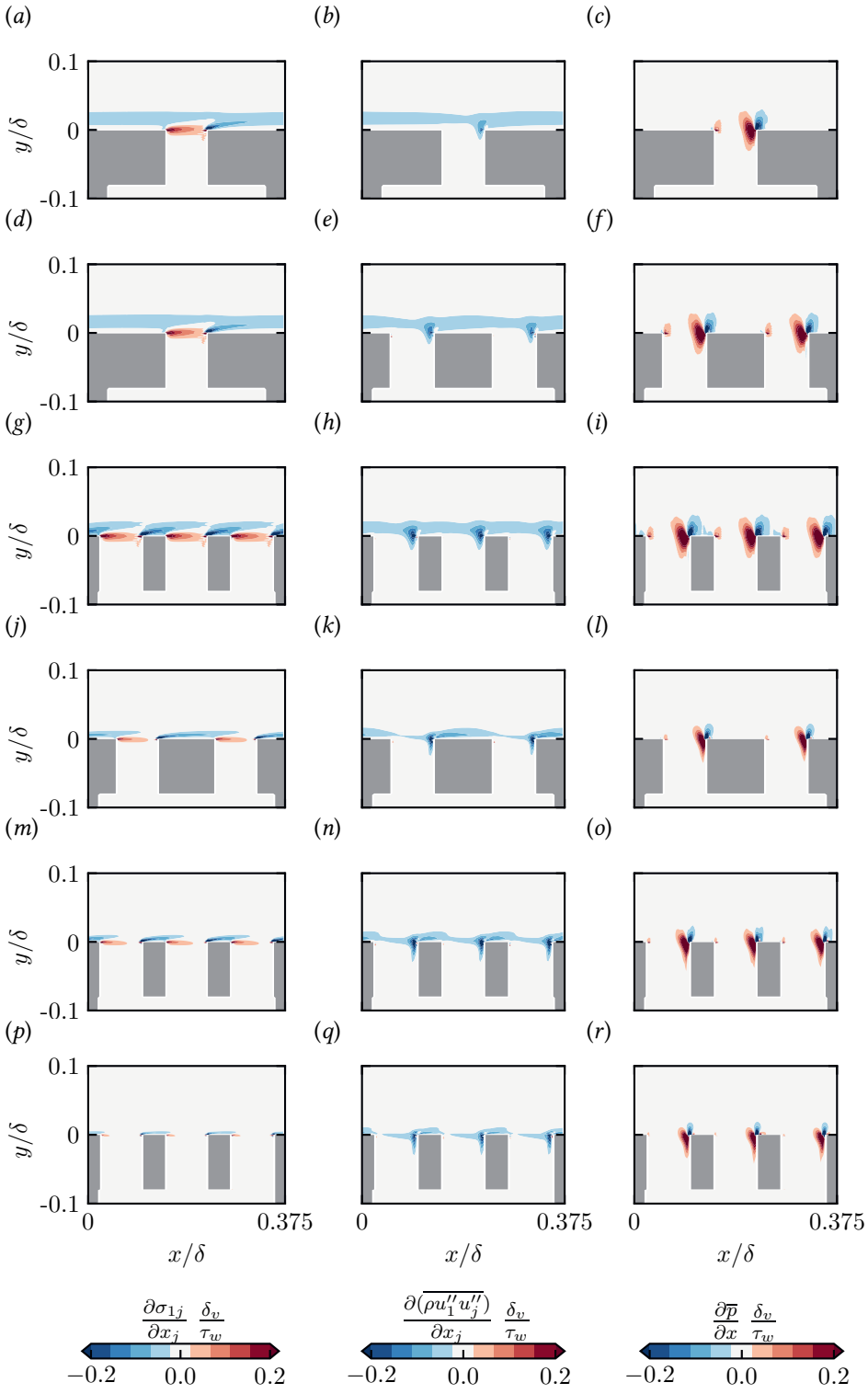

Figure 4.12: Contours of viscous diffusion (left), turbulent convection (middle) and pressure gradient (right), normalised by τ_w/δ_v for cases *L-L*$_3$(*a,b,c*), *L-L*$_{14}$(*d,e,f*), *L-L*$_{32}$(*g,h,i*), *L-M*$_{14}$(*j,k,l*), *L-M*$_{32}$(*m,n,o*) and *L-H*$_{32}$(*p,q,r*).

	$1/\alpha_y^+$	$C_f \times 10^3$	$C_{f,v} \times 10^3$	$C_{f,p} \times 10^3$	$C_{f,v}/C_f(\%)$	$C_{f,p}/C_f(\%)$
S-L	0	4.578	4.578	0	100	0
S-M	0	3.791	3.791	0	100	0
S-H	0	3.201	3.201	0	100	0
L-L$_3$	0.0528	4.598	4.492	0.106	97.7	2.3
L-L$_{14}$	0.859	4.855	4.389	0.466	90.4	9.6
L-M$_{14}$	1.73	4.527	3.988	0.539	88.1	11.9
L-L$_{32}$	5.14	5.539	4.149	1.390	74.9	25.1
L-M$_{32}$	10.4	5.082	3.608	1.474	71.0	29.0
L-H$_{32}$	20.8	5.267	3.029	2.238	57.5	42.5
L_t*-L*$_3$	0.0287	4.738	4.620	0.118	97.5	2.5
L_t*-L*$_{14}$	0.552	4.856	4.382	0.476	90.2	9.8
L_t*-M*$_{14}$	1.12	4.475	3.889	0.586	86.9	13.1
L_t*-M*$_{32}$	6.69	5.317	3.637	1.680	68.4	31.6

Table 4.2: Contribution of pressure ($C_{f,p}$) and viscous ($C_{f,v}$) drag to the skin-friction coefficient of acoustic liners.

maximum of $\langle \tau_{33} \rangle$ increases slightly, whereas the maximum of $\langle \tau_{11} \rangle$ decreases, compared to the smooth wall, which has also been reported for other types of porous surfaces [105, 95].

In the outer layer, the Reynolds stresses of the liner cases approximately match the smooth wall ones, as also typical of flows over rough walls. Small differences in the outer layer are visible for cases *L-M*$_{32}$ and *L-H*$_{32}$, hinting at a possible departure from outer layer similarity as the viscous-scaled Forchheimer permeability decreases. This is in contrast to what was observed for the mean streamwise velocity, whose outer layer seems to be more resilient to changes in the underlying surface pattern.

Different authors noted a correlation between wall-normal velocity fluctuations and drag variation over roughness [16, 97], riblets [92], and perforated plates [10]. Wilkinson [10] studied surfaces similar to acoustic liners geometries, and proposed the increase of wall-normal velocity fluctuations as the root cause behind the added drag. Orlandi et al. [16] and Orlandi and Leonardi [97] noted that the Hama roughness function of different 2D and 3D roughness geometries followed the same trend when reported as a function of the wall-normal velocity fluctuations, suggesting a correlation with the drag increase. The present simulations appear to confirm this trend. First, we note that acoustic liners exhibit high wall-normal velocity fluctuations inside the orifice, as shown in figure 4.14 (*a*) for flow case *L-H*$_{32}$. The peak of $\langle \tau_{22} \rangle$ corresponds to the wall-normal location of the most intense wall-normal velocity fluctuations at the downstream edge in figure 4.5.

Figure 4.14 shows ΔU^+ as a function of the maximum wall-normal Reynolds stress inside the liner orifice. Note that the latter has been weighted with the square of the porosity, following the idea that the reference velocity seen by the porous plate is the fluctuating superficial velocity, i.e. $\sigma u_2'$ [48]. All flow cases, irrespective of the thickness of the facesheet, follow the same trend, pointing to a correlation between velocity fluctuations and ΔU^+, as suggested by previous studies on rough surfaces. Large values of the wall-normal velocity fluctuations inside the orifices are clear symptoms of dominant inertial effects in this region of the flow.

This observation further supports the use of the Forchheimer permeability as the

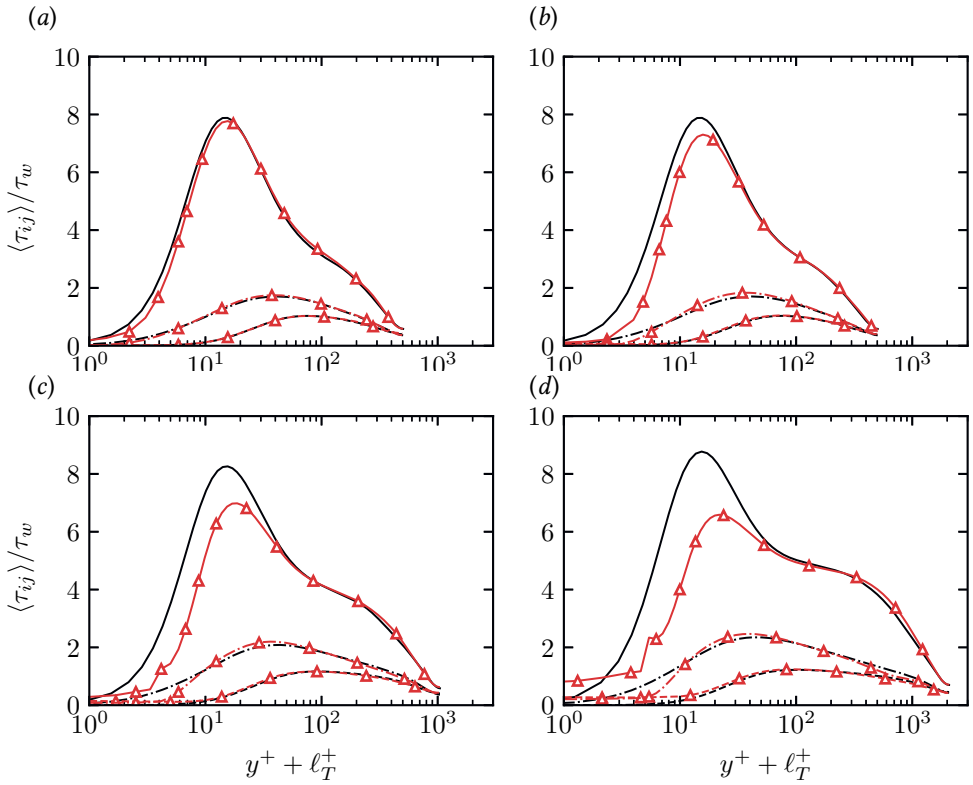

Figure 4.13: Intrinsic averaged Reynolds stresses as a function of the viscous-scaled wall-normal distance above the virtual origin for flow case L-L_{14} with $1/\alpha_y^+ = 0.859$ (a), L-L_{32} with $1/\alpha_y^+ = 5.14$ (b), L-M_{32} with $1/\alpha_y^+ = 10.4$ (c) and flow case L-H_{32} with $1/\alpha_y^+ = 20.8$ (d). Lines without symbols indicate the smooth-wall cases and the triangles indicate the liner case. Solid lines indicate $\langle \tau_{11}/\tau_w \rangle$, dashed lines indicate $\langle \tau_{22}/\tau_w \rangle$ and dashed-dotted lines indicate $\langle \tau_{33}/\tau_w \rangle$.

relevant length scale for the flow. Although there is no clear line demarcating where non-Darcy effects become dominant over the Darcy ones, Tanner et al. [47] note that already beyond pore Reynolds number $Re_p \approx 10$, it is necessary to account for non-Darcy effects. Using the maximum of the wall-normal velocity variance inside the orifice (weighted with σ), the pore Reynolds numbers for the present flow cases are in the range $Re_p \approx 50 - 500$, which is well into the nonlinear regime of permeability.

To further investigate what these wall-normal velocity fluctuations arise from, we look at the budget of the wall-normal velocity variance,

$$\frac{\partial}{\partial x_i}\left(\overline{\rho}\widetilde{u_2''u_2''}\tilde{u}_i\right) = P_k + T_k + \Pi_k + \Pi_{\alpha\alpha} - \epsilon, \tag{4.7}$$

where

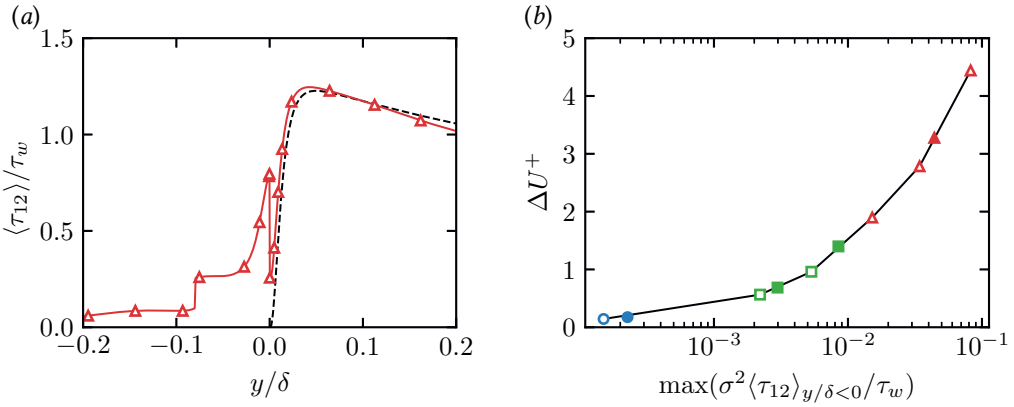

Figure 4.14: Intrinsic averaged wall-normal velocity fluctuations (*a*) as a function of the wall-normal distance for flow case *L*-H_{32} with $1/\alpha_y^+ = 20.8$ and ΔU^+ (*b*) as a function of the maximum of the wall-normal velocity fluctuations below the wall. The dashed line in (*a*) indicates the smooth-wall case. Different symbols indicate different facesheet thickness: Empty ($t = d$) and filled ($t = d/2$). Symbols indicate different porosities: $\sigma = 0.0357$ (blue circles), $\sigma = 0.143$ (green squares) and $\sigma = 0.322$ (red triangles).

$$P_k = -2\overline{\rho}\widetilde{u_2''u_i''}\frac{\partial\tilde{u}_2}{\partial x_i}, \quad \epsilon = -2\overline{\sigma_{i2}\frac{\partial u_2''}{\partial x_i}},$$
$$T_k = -\frac{\partial}{\partial x_i}\left(\overline{\rho}\widetilde{u_2''u_2''u_i''} - 2\overline{\sigma_{i2}u_2''} + 2\overline{p'u_2'}\delta_{2i}\right),$$
$$\Pi_k = -2\overline{u_2''}\frac{\partial\overline{p}}{\partial y}, \quad \Pi_{\alpha\alpha} = 2\overline{p'\frac{\partial u_2'}{\partial y}}.$$

Figure 4.15 shows the budget of the wall-normal component of the Reynolds stress tensor for flow cases *L*-M_{32} and *L*-H_{32} above the wall. The two dominant terms in the budget appear to be the pressure-strain correlation, $\Pi_{\alpha\alpha}$ and the transport term, T_k. Furthermore, T_k consists primarily of the transport of wall-normal velocity fluctuations via pressure fluctuations. Energy is redistributed into the wall-normal fluctuations via the pressure-velocity correlation and then also transported with the aid of pressure fluctuations. A better insight into the wall-normal component of the Reynolds stress tensor can be obtained with the help of figure 4.16, which shows a subset of the terms of equation (4.7). Other than a small region towards the downstream edge of the orifice, which corresponds, approximately with the strip of high wall-normal velocity fluctuations seen at the downstream edge in figure 4.5, production of wall-normal velocity fluctuations inside the cavity plays a relatively minor role, paling in comparison to the redistribution of energy into $u_2'^2$. Pressure fluctuations at the downstream edge redistribute energy into the wall-normal component of the Reynolds stress tensor and this effect appears to be stronger as d^+ increases. The location of maximum turbulent kinetic energy redistribution corresponds to the location of the peak in wall-normal Reynolds stress inside the orifice, shown in figure 4.5 and 4.14.

Production plays a minor role and energy is not extracted from the mean flow for the wall-normal velocity fluctuations. The enhanced transfer of energy into the wall-

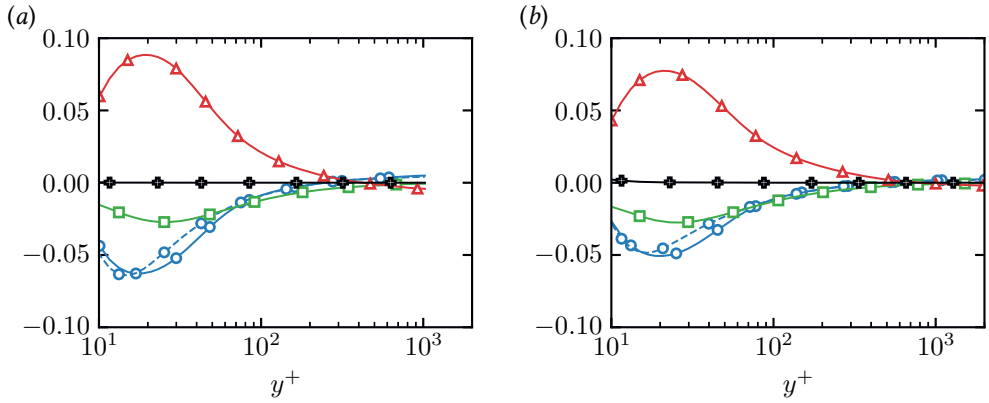

Figure 4.15: Intrinsically averaged budget of the wall-normal component of the Reynolds stress tensor for flow case $L\text{-}M_{32}$ (*a*) and $L\text{-}H_{32}$ (*b*). Symbols represent different terms: T_k (blue circles), ϵ (green squares), $\Pi_{\alpha\alpha}$ (red triangles) and P_k (black plusses). The dashed line with circles represents the transport of wall-normal velocity fluctuations due to pressure fluctuations.

normal component matches the findings of Yuan and Piomelli [106], who noted in their simulation of sand-grain roughness that energy is redistributed into the wall-normal velocity fluctuations, particularly below the roughness crest as is also observed for acoustic liners, that then distort the near-wall streamwise structures.

4.2.5 Spectral Densities

The spectral analysis of velocity fluctuations provides additional insight into the organization of turbulence. Figures 4.17 show the pre-multiplied spectral densities of the streamwise and wall-normal velocity components as a function of the wall-normal distance from the virtual origin and the spanwise wavelength λ_z, for flow cases $L\text{-}L_{32}$, $L\text{-}M_{32}$ and $L\text{-}H_{32}$.

Spectrograms of the smooth wall cases (isolines) show the typical organization that characterizes wall turbulence. At low Reynolds numbers a near-wall energy peak is evident, at wavelength $\lambda_z^+ \approx 100$, corresponding to the near-wall cycle. The smooth wall flow case at $Re_\tau = 2000$ shows a secondary energy peak in the outer layer for the streamwise velocity fluctuations, which is associated with the emergence of large-scale energy-containing structures in the outer layer [107].

At the lowest Reynolds number, the spectra for the acoustic liners (coloured contour) match very well the smooth wall results, with minor differences only visible around the near-wall peak. An obvious difference from the smooth wall is the presence of a distinct energy peak in the spanwise velocity spectrogram at a wavelength corresponding to the spacing of the orifices. This energy maximum is accompanied by a decrease in the inner energy peak, which was also observed in the streamwise velocity variance in figure 4.13, and it becomes more prominent for increasing Reynolds number.

The same trend is also visible for the wall-normal velocity fluctuations. However, in this case, the near-wall energy peak is visible primarily for the high Reynolds case $L\text{-}H_{32}$ and is spread out over a larger band of wavelengths. We further note that the peak of the

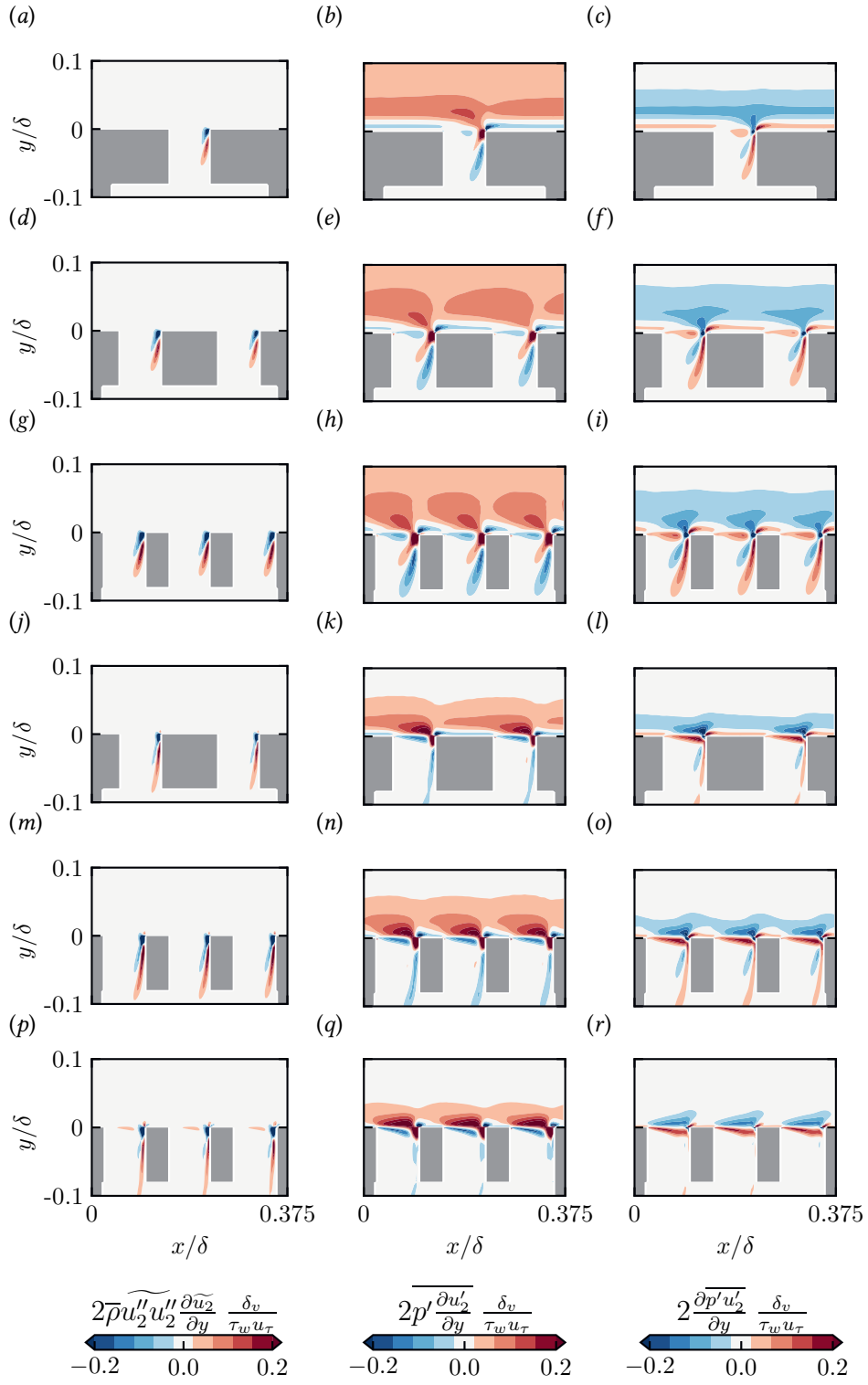

Figure 4.16: Contours of $2\overline{\rho}\widetilde{u_2''u_2''}\partial\widetilde{u}_2/\partial y$ (left), $2\overline{p'\partial u_2'/\partial y}$ (middle) and $2\partial(\overline{p'u_2'})/\partial y$ (right), normalised by $(\tau_w u_\tau)/\delta_v$ for cases *L*-L_3(*a*, *b*, *c*), *L*-L_{14} (*d*, *e*, *f*), *L*-L_{32}(*g*, *h*, *i*), *L*-M_{14}(*j*, *k*, *l*), *L*-M_{32}(*m*, *n*, *o*) and *L*-H_{32}(*p*, *q*, *r*).

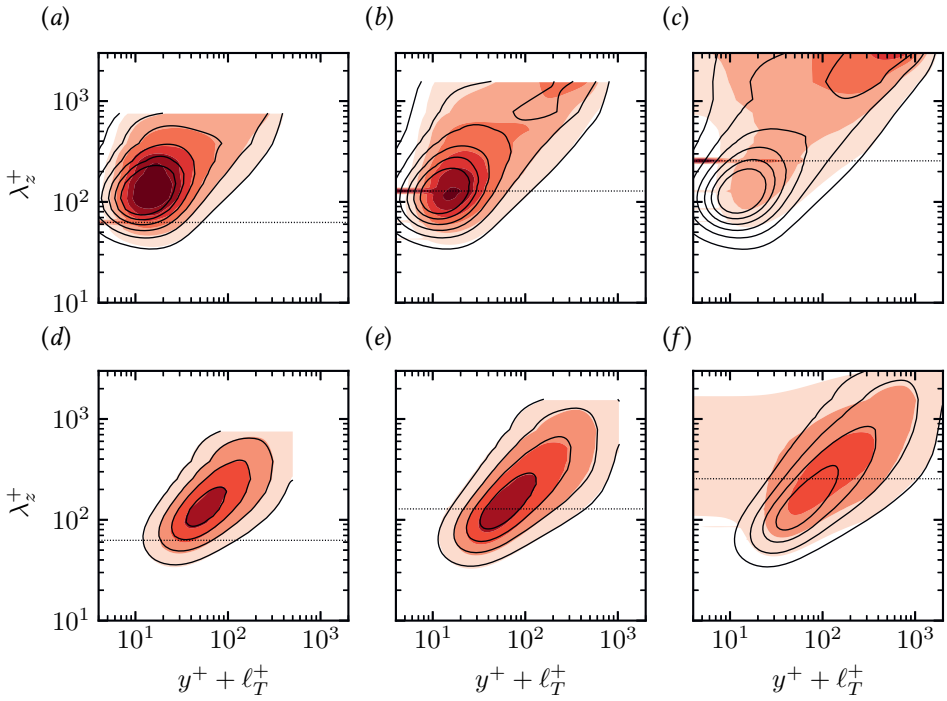

Figure 4.17: Premultiplied streamwise velocity (*a*)-(*c*) and wall-normal velocity (*d*)-(*f*) spectra, normalised by u_τ^2. Filled contours represent flow case *L*-L_{32} (*a*),(*d*), flow case *L*-M_{32} (*b*),(*e*) and flow case *L*-H_{32} (*c*),(*f*). Contour lines represent smooth wall flow cases at matching Re_τ. The dotted line indicates the spacing of the orifices, normalised by the viscous length scale. Contour levels [1.0,2.0,3.0,4.0,5.0,6.0] are shown for the streamwise velocity spectra and [0.25,0.50,0.75,1.00] are shown for the wall-normal velocity spectra.

near-wall cycle is slightly biased towards the length scale corresponding to orifice spacing. This wavelength bias was also observed by Chu et al. [108] on porous beds formed by cylindrical elements.

The picture that emerges is that acoustic liners drain energy from the near-wall cycle, and tend to re-arrange it at length scales typical of the underlying surface pattern, such as the orifice spacing. This behaviour has also been reported for other types of surface patterns, such as plant canopies [109].

Notable differences are visible for flow case *L*-H_{32}, where the streamwise velocity spectrum tends to deviate from the smooth wall case away from the wall, exhibiting greater energy at higher wavelengths. Furthermore, unlike cases *L*-L_{32} and *L*-M_{32}, higher wavelengths also exhibit energy closer to the wall. Therefore, near-wall energy is concentrated in two distinct regions for case *L*-H_{32}, a sharp tonal peak at the orifice spacing ($\lambda_z \approx 250$) and a range of higher wavelengths ($\lambda_z \gtrapprox 1000$). Given the scale separation between the two wavelength bands, and the existence of a distinct outer layer energy peak, the energy at higher wavelengths in the near-wall region may be associated with the footprint of large-scale structures interacting with the near-wall turbulence. This behaviour is also

typical of flows over smooth walls, although it emerges at much higher Reynolds numbers [110]. Modification of inner/outer layer interaction due to surface roughness has been observed in many other studies, in different forms. Efstathiou and Luhar [34] observed an enhancement of the interaction over porous surfaces, as compared to the smooth wall, and associated it to the appearance of spanwise-elongated structures close to the wall. Kim et al. [111] also observed stronger inner/outer layer interaction over porous surfaces, and they associated it to the enhanced wall-normal turbulent mixing caused the relaxation of the impermeability condition. A similar effect was also reported over rough walls [112].

It seems that acoustic liners promote inner/outer layer interaction at lower Reynolds number, probably because the flow is approaching the fully rough regime, thus the viscous effects which would normally mask this interaction are less prominent and we observe flow features of high Reynolds number turbulence already at $Re_\tau \approx 2000$. A different interpretation of the same mechanism can be that the near-wall cycle penetrates deeper into the porous media, thus effectively reducing the viscous sublayer perceived by the large-scale eddies, which therefore scrapes the surface of the liner at a lower friction Reynolds number than on a smooth wall, which is also consistent with the interpretation of Kim et al. [111].

Addendum: Flow through a Perforated Plate

Methodology

In this section, we estimate the Darcy and Forchheimer permeability coefficients. In order to calculate the permeability, we perform simulations of laminar flow through a perforated plate using the setup sketched in Figure 2.5. We solve the incompressible Navier–Stokes equations, and fix the superficial velocity at the inflow and the pressure at the outflow. Neumann boundary conditions are used for the outflow velocity and inflow pressure. No-slip boundary condition is used at the surface of the perforated plate, and symmetry boundary conditions are used at the lateral boundaries.

Simulations discussed in this section are performed with the pimpleFoam solver, which is part of the open-source library OpenFOAM® [113]. A forward Euler time step scheme with a maximum CFL number of 0.7 is used and simulations are run until a steady-state solution is reached (residual $< 10^{-9}$). The inflow and outflow boundaries are at least 40 orifice diameters away from the perforated plate. We have verified that the final solution is independent of the domain size. Approximately 10M cells are used with a minimum mesh size of $\approx 0.001d$ in the proximity of the plate orifice. We have performed a grid resolution study to ensure that the presented results are fully converged.

Permeability: Darcy and Forchheimer

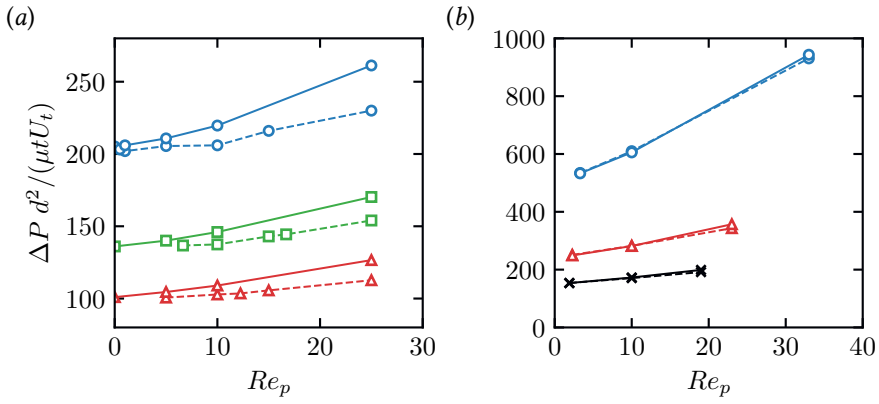

Figure 4.18: Normalised pressure drop as a function of the pore Reynolds number for cases B_{r1}-B_{r3} (*a*) and cases T_{r1}-T_{r3} (*b*). Solid lines represent pressure drop for the current simulations. Dashed lines represent the pressure drops by Bae and Kim [48] and Tanner *et al.* [47] in (*a*) and (*b*), respectively. Symbols refer to different porosities: $\sigma = 0.2$ (circles), $\sigma = 0.3$ (squares), $\sigma = 0.4$ (triangles) and $\sigma = 0.5$ (crosses).

We consider 9 plate geometries with different porosity and thickness-to-diameter ratio t/d, which are summarised in Table 4.3. Six geometries are designed to match the parameters of Bae and Kim [48] ($B_{r1} - B_{r3}$), and Tanner *et al.* [47] ($T_{r1} - T_{r3}$), whereas ($L_{g1} - L_{g3}$) are geometries corresponding to the DNS flow cases reported in the bulk of this chapter. Permeability is considered independent of the spacing of the holes [48, 66, 47], therefore we simulate plates with a single orifice, and change the porosity by changing the orifice diameter. The pressure drop ΔP is evaluated as the difference between the inlet

	σ	t/d	$\alpha_y d$						
			Kast *et al.*	Idelchik	Malvasi *et al.*	Miller	Holt *et al.*	Bae and Kim	Present
B_r1	0.2	2	12.3	6.59	12.5	6.55	4.82	7.5	7.68
B_r2	0.3	2	4.69	2.36	4.62	2.35	1.75	2.91	4.67
B_r3	0.4	2	2.25	1.05	2.07	1.02	0.791	1.41	2.61
T_r1	0.2	0.25	98.0	94.9	100	247	89.9	60.0	70.2
T_r2	0.4	0.25	18.0	15.2	16.6	38.5	13.4	11.2	13.17
T_r3	0.6	0.25	5.55	3.69	3.91	8.28	3.69	3.33	4.43
L_g1	0.0357	1	960	643	1005	644	604	567	763
L_g2	0.143	1	51.9	33.1	53.8	33.6	25.0	31.4	46.2
L_g3	0.322	1	7.89	4.51	7.59	3.95	3.00	4.91	7.87

Table 4.3: Forchheimer coefficient for different porosities σ and thickness-to-diameter ratio t/d. The last column refers to the present dataset, whereas the other columns refer to the values obtained with engineering correlations reported at the end of the chapter.

and outlet pressure, see the sketch in Figure 2.5(a). For each of the 9 plate geometries , we perform simulations at different Re_p and use Equation (2.5) to compute the Darcy permeability and the Forchheimer coefficient.

Figure 4.18 shows the pressure drop of flow cases $B_{r1} - B_{r3}(a)$ and $T_{r1} - T_{r3}(b)$ for our simulations and corresponding data from Bae and Kim [48] and Tanner *et al.* [47]. We note a disagreement for flow cases $B_{r1} - B_{r3}$ when compared to the data of Bae and Kim [48], which becomes more evident for increasing pore Reynolds number, with differences up to 20% at the highest Re_p. On the contrary, we observe a very good match for flow cases $T_{r1} - T_{r3}$ with the data of Tanner *et al.* [47]. The reasons for the mismatch between the two datasets can be numerous, but are most likely down to the different flow solver and numerical set up. For example, an upwind scheme was used by [48], whereas a second-order central discretization scheme is used for the present simulations. Discrepancies of this order of magnitude are possible at high Re_p [66], and therefore we consider the differences acceptable.

As additional validation, we compare the Forchheimer coefficients from the current simulations to several engineering correlations based on experimental data, which are summarized at the end of the chapter. The values of α_y returned by these correlations are reported in Table 4.3. There is a large spread in the Forchheimer coefficient proposed by the different correlations, and differences up to 50–60% seem common in the literature.

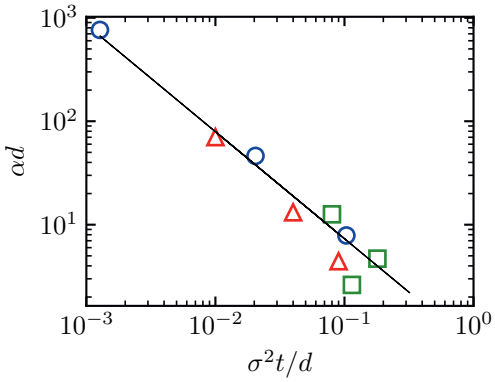

Figure 4.19: Forchheimer coefficient $\alpha_y d$ as a function of $\sigma^2 t/d$ for L_{g1}-L_{g3} (circles), B_{r1}-B_{r3} (squares) and T_{r1}-T_{r3} (triangles).

This large uncertainty of the Forchheimer coefficient can be traced back to the weak dependence of α_y on Re_p, which has been reported by several studies [47]. Most of these empirical correlations are based on data at high pore Reynolds numbers in the attempt to minimize the dependence on Re_p. However, this is often not enough because the dependence of α_y on Re_p can be more or less significant depending on the thickness-to-diameter ratio t/d [47], thus complicating the evaluation of the Forchheimer coefficient. Perfect agreement with the empirical correlations is therefore not expected. The Forchheimer coefficients we calculate are within the range of the engineering correlations (50%-60% spread, Table 4.3), that are based on experimental data at high Reynolds number. Comparison with previous

numerical simulations in figure 4.18, show a much better agreement with our data.

Even though these correlations differ from each other, they all suggest the same trend of the Forchheimer coefficient for low values of σ, namely $\alpha_y \sim 1/(\sigma^2 t)$. For this reason, we report $\alpha_y d$ as a function of $\sigma^2 t/d$ in Figure 4.19. The figure shows a visual representation of the Forchheimer coefficient which highlights that the dependence of α_y on the geometry is approximately captured with a single geometrical parameter. The approximation $\alpha_y \sim 1/(\sigma^2 t)$ is accurate for lower values of the porosity, whereas we observe larger errors for large σ. For low values of the porosity $\sigma < 0.2$ this simple analytical formula has comparable accuracy as experimental data.

Empirical Correlations for Pressure Drop through Perforated Plates

We report popular engineering formulas for estimating the Forchheimer coefficient or the friction factor, used in table 4.3.

Bae and Kim [48] performed numerical simulations of flow through perforated plates and, proposed the following expression for the Forchheimer coefficient:

$$\alpha_y = \frac{3(1-\sigma)}{4\sigma^2 t}. \tag{4.8}$$

Several experimental studies at high Reynolds number are available which provide semi-empirical formulas for the friction factor, which can be easily converted into Forchheimer coefficient. Idelchik [64] provides several empirical correlations for estimating the friction factor across a perforated plate. At finite thickness of the plate and high Reynolds number, Idelchik [64] proposes a correlation of the form:

$$\alpha_y = \frac{1}{2\sigma^2 t}\left(0.5 + 0.24\sqrt{1-\sigma}(1-\sigma) + (1-\sigma)^2\right). \tag{4.9}$$

Malavasi *et al.* [66] suggest an alternative relationship of the form:

$$\alpha_y = \frac{1}{2C^2\sigma^2 t}\left(\sqrt{1-\sigma^2-\sigma^2C^2} - C\sigma\right)^2, \tag{4.10}$$

where C is a discharge coefficient that depends upon the geometrical parameters of the orifice and the Reynolds number. Similarly, Kast *et al.*[65] proposes the following relationship:

$$\alpha_y = \frac{1}{2\sigma^2 t}\left(\left(\frac{1}{C} - 1\right)^2 + (1-\sigma)^2\right). \tag{4.11}$$

According to Miller [67] the Forchheimer coefficient can be expressed as:

$$\alpha_y = \frac{C_0(1 - C_c\sigma)}{C_c^2\sigma^2 t}, \tag{4.12}$$

where C_0 is a coefficient that depends on t/d and C_c is the jet contraction coefficient. Holt *et al.* [68] present a piecewise function for the Forchheimer coefficient,

$$\alpha_y = \begin{cases} \frac{1}{2t}\left(2.9 - 3.79\frac{t}{d}\sigma^{0.2} + 1.79\left(\frac{t}{d}\right)^2\sigma^{0.4}\right)K & \frac{t}{d}\sigma^{0.2} < 0.9 \\ \frac{1}{2t}\left(0.876 - 0.069\frac{t}{d}\sigma^{0.2}\right)K & \frac{t}{d}\sigma^{0.2} > 0.9, \end{cases}$$

where $K = 1 - 2/\sigma + 2/\sigma^2(1 - 1/C_C + 1/(2C_C^2))$.

5

Optimised Acoustic Liner Geometries

Parts of this chapter have been published in AIAA Journal 62 (8), 3018-3026

The previous chapter identified the inverse of the Forchheimer coefficient as the characteristic length scale of acoustic liners. We saw that the drag increase can be traced back to the very high wall-normal velocity fluctuations emanating from the orifice. This leads to the possibility that by restricting somehow these wall-normal velocity fluctuations, by for example changing orifice geometry, the drag increase can be limited. However, any change made to orifice and liner geometry influences its acoustic performance and as acoustic liners are used primarily to reduce engine noise, it is imperative that any changes made to acoustic liner geometry not negatively influence the noise attenuation. The following sections highlight the potential for simultaneous acoustic and aerodynamic optimisation of acoustic liner geometries simply by slight modifications to conventional acoustic liner orifice geometries. We begin first by introducing the setup and the geometries considered, including the rationale behind the modifications. We then proceed with demonstrating their aerodynamic and acoustic properties.

5.1 Methodology

5.1.1 Test Setup

In a similar vein to chapter 4, we solve the compressible Navier–Stokes equations for a calorically perfect gas using the solver STREAmS [70, 114], at friction Reynolds numbers $Re_\tau = \delta/\delta_v \approx 500$ and at bulk Mach number $M_b = u_b/c_w = 0.3$. The box size, cavity dimensions, and acoustic liner is distribution is the same as chapter 4, see Fig. 5.1. We use uniform mesh spacing in the streamwise and spanwise directions. In the wall-normal direction, the mesh is clustered towards the wall and coarsened towards the backplate and the channel centre. A minimum of 26 mesh points are used to resolve the orifice diameter (or minor axis in the case of an ellipse). This resolution is well within the viscous spacing typically accepted in DNS, as shown in section 3.5.3.

We wish to study the influence of orifice geometry on the aerodynamic and acoustic performance of a liner and compare it to the baseline configuration with circular straight holes that are common in most applications. For the baseline reference case, see Fig. 5.1 (*b*) we consider the geometry studied in chapter 4, with porosity $\sigma = 0.322$, viscous-scaled diameter $d^+ = d/\delta_v \approx 40$ and a thickness to diameter ratio $t/d = 1$, where the orifice diameter for the baseline case is $d = 0.08\delta$. We chose the baseline liner geometry to be representative of acoustic liners in operating conditions, while also keeping a reasonable computational cost to perform a parametric study using DNS. The orifice size and facesheet thickness are in the range found on engine-mounted acoustic liners when scaled with the local boundary layer thickness in landing conditions, as discussed in chapter 2. The cavity depth we use is smaller than in real applications, however, previous studies have reported that its influence on the added drag is negligible [11]. The porosity is slightly higher than typically found on modern aircraft engines. However, in the previous chapter we demonstrated that that the relevant nondimensional parameter for quantifying the added drag is the viscous-scaled Forchheimer permeability, which is thus a more relevant nondimensional quantity than the porosity.

To compare the result of liner simulations with the smooth wall data, we take into account the effect of the virtual origin ℓ_T, namely, the distance below the plate at which the flow perceives the equivalent smooth wall, see figure 4.7. All simulations are advanced

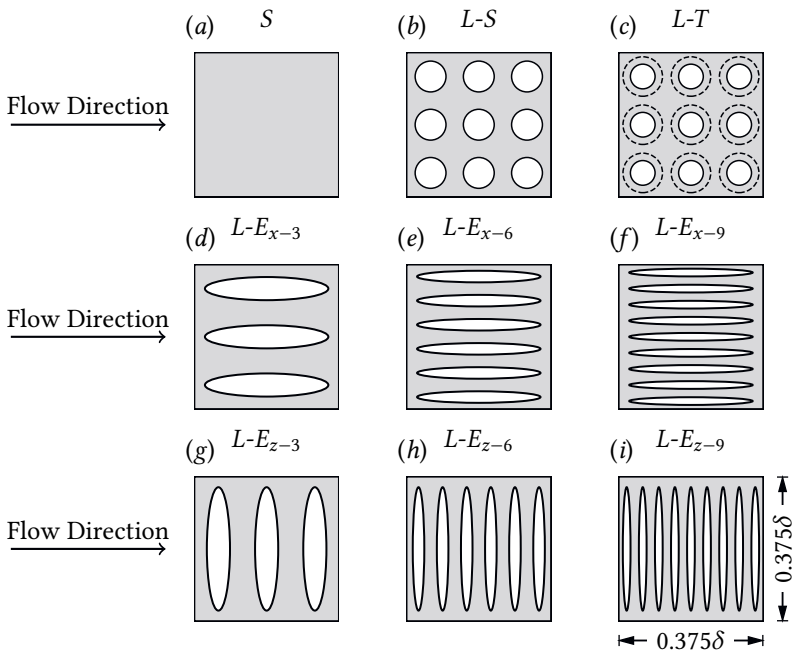

Figure 5.1: Orifice configurations considered. All liner cases, except for case L_T have a top surface open area ratio of $\sigma = 0.322$. All liner cases are such that the total volume of the perforations is equal to $V_o = 9\pi d_s^2 t/4$, where d_s is the diameter of the baseline orifice configurations and $t = d_s$ is the thickness of the facesheet that is constant for all cases.

forward in time until they reach a statistically stationary state, after which statistics are collected for at least $T_{\text{av}} u_\tau/\delta \approx 16$, where T_{av} is the averaging interval.

5.1.2 Novel Configurations

The facesheet thickness and the cavity dimensions remain unchanged for all cases considered. The novel configurations proposed only differ in the orifice shape, size, and orientation. In an attempt to reduce the aerodynamic drag induced by acoustic liners, we pursue two ideas:

- We aim at increasing the wall-normal Forchheimer permeability of the plate α_y. Although α_y has a complex dependency on the plate geometry, a first-order approximation is $\alpha_y \sim 1/(\sigma^2 t)$ [51], and therefore a reduction of the plate permeability will result in lower drag.
- We take inspiration from riblets, namely streamwise-aligned surface grooves that are able to reduce friction drag [22, 115], and argue that the same surface anisotropy in the streamwise direction might be beneficial for acoustic liners.

Following these two hypotheses, we propose liner geometries that should be more efficient from an aerodynamic perspective and possibly retain the acoustic properties of the

	Re_b	Re_τ	d_x^+	d_z^+	$K/t^2 \times 10^3$	$1/(\alpha t)$	Δx^+	Δy^+_{min}	Δz^+	N_x	N_y	N_z	ΔU^+	$C_f \times 10^3$
S-L	18536	506.1	0	0	-	-	5.1	0.80	5.1	300	350	150	-	4.58
L-L_{32}	16528	505.3	40.4	40.4	6.33	0.127	1.5	0.80	1.5	1000	500	500	1.90	5.54
L-T	16984	515.8	33.0	33.0	17.0	0.156	1.3	0.81	1.3	1200	600	500	1.45	5.28
L-E_{x-3}	13124	492.8	29.6	157.7	7.32	0.0869	5.9	0.79	1.1	250	500	700	4.87	7.78
L-E_{x-6}	15602	501.5	15.0	160.5	2.23	0.0401	6.0	0.80	0.6	250	500	1300	2.33	5.80
L-E_{x-9}	17300	515.5	10.3	165.0	1.07	0.0217	6.2	0.82	0.4	250	500	2000	0.85	4.97
L-E_{z-3}	16104	510.0	163.2	30.6	7.32	0.0869	1.1	0.82	6.1	1400	500	125	2.17	5.70
L-E_{z-6}	16042	506.8	162.1	15.2	2.23	0.0401	0.6	0.81	6.1	2600	500	125	2.29	5.78
L-E_{z-9}	16670	515.6	165.0	10.3	1.07	0.0217	0.4	0.82	6.2	4000	500	125	1.90	5.54

Table 5.1: DNS dataset comprising smooth (S-L), baseline liner (L-L_{32}) and novel liner (L-C) cases where $C = \{S, T, E_{x-\chi}, E_{z-\chi}\}$ corresponds to the orifice configuration and χ is the number of ellipses per cavity. Cases S-L and L-L_{32} are as in chapter 4. ΔU^+ is the Hama roughness function measured at $y^+ + \ell_T^+ = 100$, where ℓ_T is the virtual origin shift. Simulations are performed in a computational box with dimensions $L_x \times L_y \times L_z = 3\delta \times 2(\delta + h) \times 1.5\delta$. d_x and d_z are the lengths of the streamwise and spanwise axes of the orifices. For cases L-L_{32} and L-T, $d_x^+ = d_z^+$. Δx^+ and Δz^+ are the viscous-scaled mesh spacing in the streamwise and spanwise direction, and Δy^+_{min} is the minimum mesh spacing in the wall-normal direction.

liner. Therefore, we change the orifice geometry while keeping constant the resonance frequency of the resonators $\omega_r = c_w \sqrt{A/tV_c}$. In this way, we aim to optimise the aerodynamic performance without compromising the acoustic properties.

Based on the first idea, we propose a 'tapered-hole' configuration where the orifice has a smaller diameter at the top of the facesheet and a larger diameter at the bottom of the facesheet, such that the total volume of the orifice is constant and the resonance frequency of the liner, disregarding entry and exit effects, does not change. Entry and exit effects are included using empirical correction factors when determining the resonance frequency of the liner as they change the effective mass of air that oscillates in the orifice. For a canonical orifice shape, the correction is known and well-documented [116, 117, 118, 7]. Since entry/exit effects are accounted for by empirical corrections, our hypothesis can only be verified a posteriori through acoustic simulations at different frequencies. For the considered case (case *L-T*) the orifice diameter increases continuously from $d = 0.064\delta$ at the top of the facesheet to $d = 0.1024\delta$ at the bottom of the facesheet.

Based on the second idea, we propose elliptical orifices, that have the same porosity as the baseline liner, i.e. $\sigma = 0.322$. The major axis of the ellipse is fixed at $a = 0.32\delta$ and the minor axis is calculated by assuming a constant porosity and depends on the number of orifices per cavity. For example, in the case of 9 elliptical orifices per cavity, see Fig. 5.1 (*f*) or (*i*), the minor axis is $b = 0.02\delta$, and in the case of 3 elliptical orifices per cavity, see Fig. 5.1 (*d*) or (*g*), the minor is $b = 0.06\delta$, such that the porosity is always $\sigma = 0.322$.

In addition, the influence of the elliptical orifices' orientation is also studied. While we expect that streamwise-aligned ellipses should minimize the added drag, previous experiments [53] have shown that rectangular slots perpendicular to the flow have lower drag compared to the canonical configuration. Therefore, we consider elliptical orifices with the major axis aligned with the streamwise or spanwise direction.

The geometries considered are shown in Fig. 5.1, and details of all flow cases are reported in Table 5.1. The naming of the flow cases for the two baseline cases, *S-L* and L-L_{32} is as in chapter 4, and *L-C* for the novel liner cases, where $C = \{S, T, E_{x-\chi}, E_{z-\chi}\}$ refers to the specific liner flow case. In particular, T, $E_{x-\chi}$ and $E_{z-\chi}$ are the tapered-orifice liner, streamwise-oriented ellipses and spanwise-oriented ellipses, respectively, and χ is the number of ellipses per cavity.

5.2 Peformance Characteristics

5.2.1 Aerodynamic Drag

Figure 5.2 shows the mean streamwise velocity profiles for all flow cases. We see that the mean velocity profile over acoustic liners is shifted downward as compared to the smooth wall. In Fig. 5.2 we note that all liner cases show a downward shift compared to the smooth wall (ΔU^+), indicating that all cases increase drag. However, several liner geometries exhibit a lower ΔU^+ compared to the baseline case, demonstrating that modifying the orifice shape can result in a lower added drag. For convenience, the value of the Hama roughness function ΔU^+ and the friction coefficient are also reported in Table 5.1.

Some elliptical orifice configurations show potential for decreasing the added drag. However, this depends both on the ellipse dimensions and orientation. For streamwise-oriented slots, the drag variation strongly depends on the spanwise size of the orifices. The

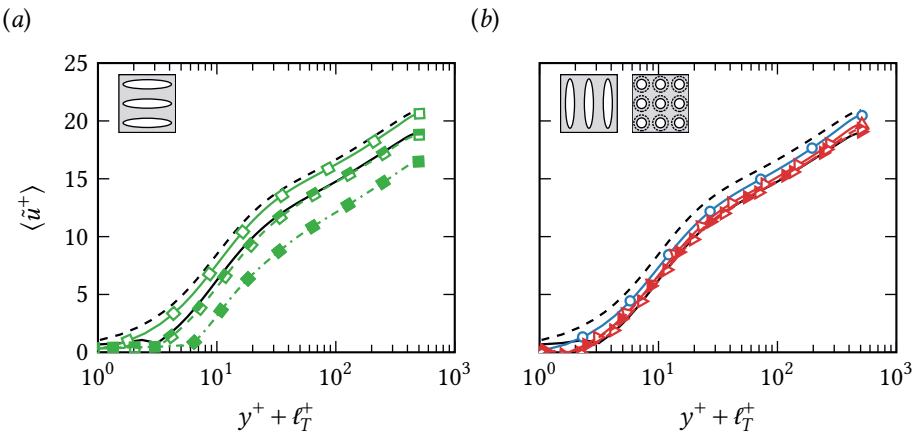

Figure 5.2: Mean streamwise velocity for streamwise-oriented ellipses (*a*) and for spanwise-oriented ellipses and tapered circular holes (*b*). Novel geometries are compared to the smooth wall flow case (dashed black line without symbols) and to the baseline liner flow case (solid black line without symbols). The novel liner flow cases have the following line style: *L-T* (circles), *L-E*$_{x-\chi}$ (squares) and *L-E*$_{z-\chi}$ (triangles). Different line types with symbols indicate the number of orifices per cavity: $\chi = 3$ (dash-dotted line with filled symbols), $\chi = 6$ (dashed line with half-filled symbols) and $\chi = 9$ (solid line with empty symbols).

5

narrow orifices of flow case *L-E*$_{x-9}$ lead to a substantially lower drag than the baseline case, whereas the wider slots of case *L-E*$_{x-3}$ result in a massive drag increase. It is interesting to note that the elliptical slots of *L-E*$_{x-9}$ have a spanwise width of size $d_z^+ \approx 10$, which is similar to the spacing of drag-reducing riblets [22]. For spanwise-oriented slots, ΔU^+ is less sensitive to the slots size, and we find the same or a marginally lower drag than the baseline liner. These findings confirm the experiments of Howerton and Jones [53] who observed lower drag for spanwise-oriented rectangular slots. They found that streamwise-oriented rectangular slots increased drag compared to the baseline case, however, they did not investigate the effect of slot size, which might have been too large in viscous units to observe the 'riblets-like' effect we report in this study. The tapered orifice also decreases drag compared to the baseline case. In this case, the improved performance can be traced back to the reduced superficial porosity experienced by the flow.

In a previous chapter, we related the added drag induced by acoustic liners to the wall-normal velocity fluctuations; thus, we inspect instantaneous velocity realizations in wall parallel planes at $y^+ + \ell_T^+ = 8$ in Fig. 5.3 and 5.4. For all liner cases, we note that near-wall streaks are disrupted and much shorter than on a smooth wall, see Fig. 5.3. The break-up of the near-wall streaks is particularly evident for case *L-E*$_{x-3}$ (Fig. 5.3 (*g*)), where the near-wall flow deviates substantially from the typical organization found for the smooth wall (Fig. 5.3 (*a*)).

For the baseline liner geometry, wall-normal velocity fluctuations are concentrated, primarily, around the orifice location, and the positions of the orifices are clearly visible in the contours of the wall-normal velocity, see Fig. 5.4 (*b*). This effect is more evident for cases *L-E*$_{x-3}$ and *L-E*$_{x-6}$, where the wall-normal velocity fluctuations in the near wall region originate primarily from the orifices. The higher wall-normal velocity fluctuations

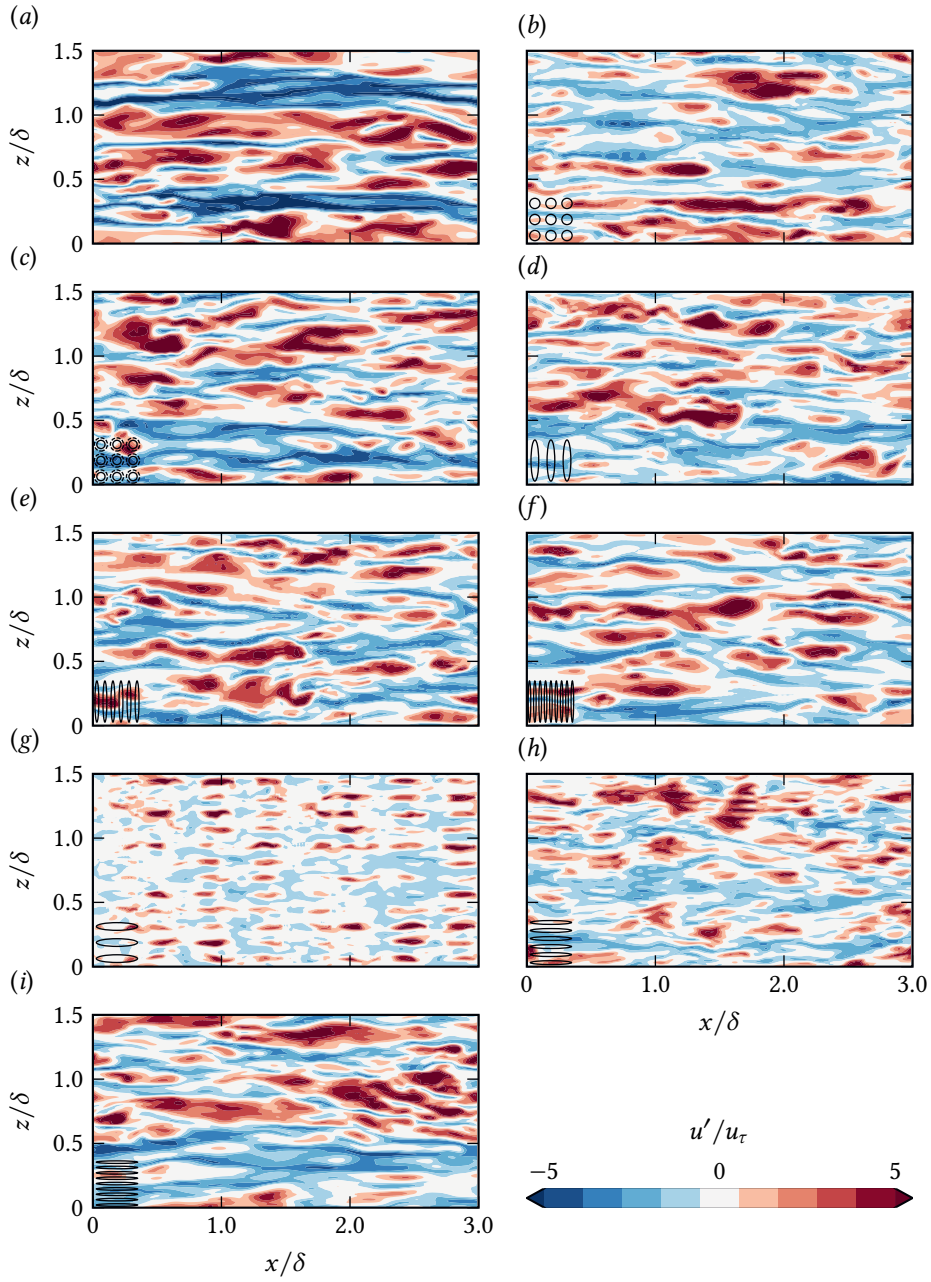

Figure 5.3: Streamwise velocity fluctuations on a wall-parallel plane at $y^+ + \ell_T^+ = 8$ for cases *S-L* (*a*), *L-L*$_{32}$ (*b*), *L-T* (*c*), *L-E*$_{z-3}$ (*d*), *L-E*$_{z-6}$ (*e*), *L-E*$_{z-9}$ (*f*), *L-E*$_{x-3}$ (*g*), *L-E*$_{x-6}$ (*h*), *L-E*$_{x-9}$ (*i*). The sketch in the lower left corner shows the shape and size of the orifices for a single cavity.

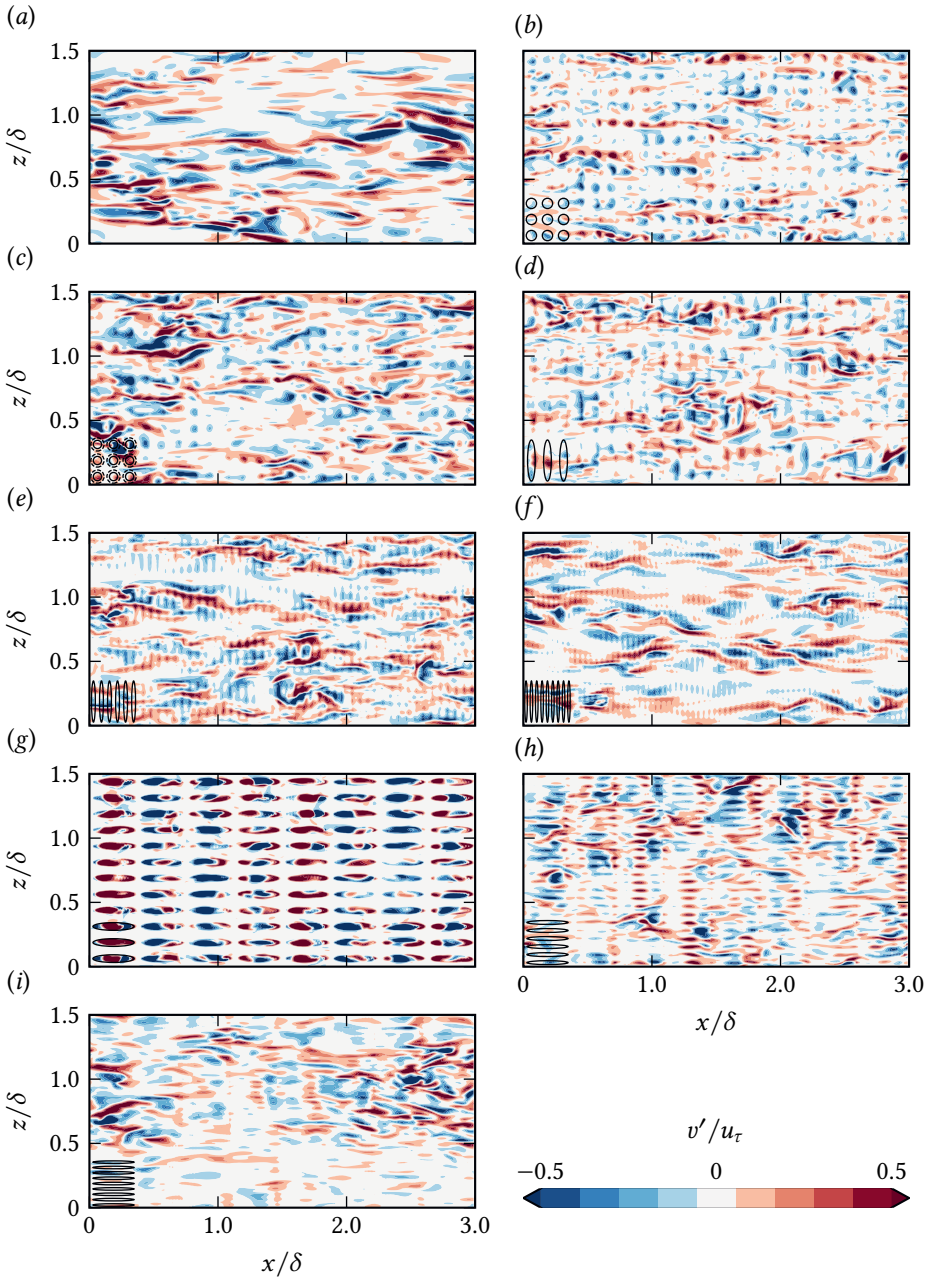

Figure 5.4: Wall-normal velocity fluctuations on a wall-parallel plane at $y^+ + \ell_T^+ = 8$ for cases *S-L* (*a*), *L-L*$_{32}$ (*b*), *L-T* (*c*), *L-E*$_{z-3}$ (*d*), *L-E*$_{z-6}$ (*e*), *L-E*$_{z-9}$ (*f*), *L-E*$_{x-3}$ (*g*), *L-E*$_{x-6}$ (*h*), *L-E*$_{x-9}$ (*i*). The sketch in the lower left corner shows the shape and size of the orifices for a single cavity.

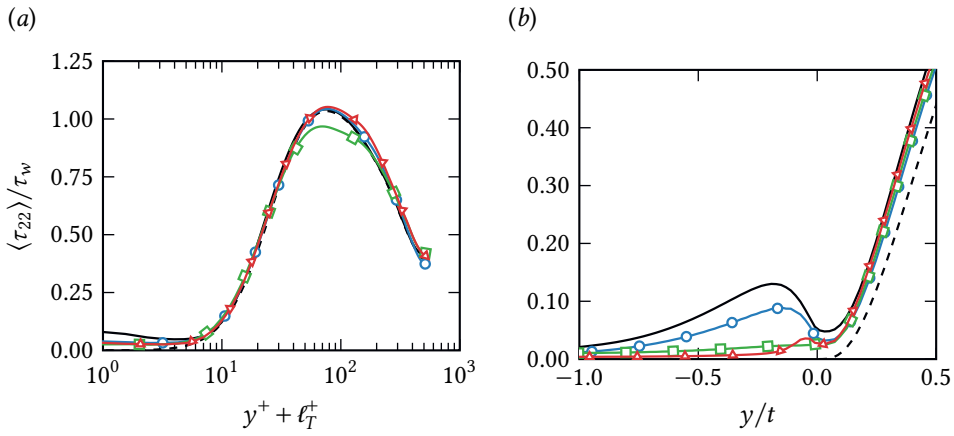

Figure 5.5: Wall normal Reynolds stress τ_{22}, as a function of the viscous-scaled wall distance (*a*) and as a function of y/t (*b*), where t is the plate thickness, for smooth wall flow case (dashed line without symbols), the baseline liner flow case (solid line without symbols) and novel liner flow cases *L-T* (circles), *L-*E_{x-9} (squares) and *L-*E_{z-9} (triangles).

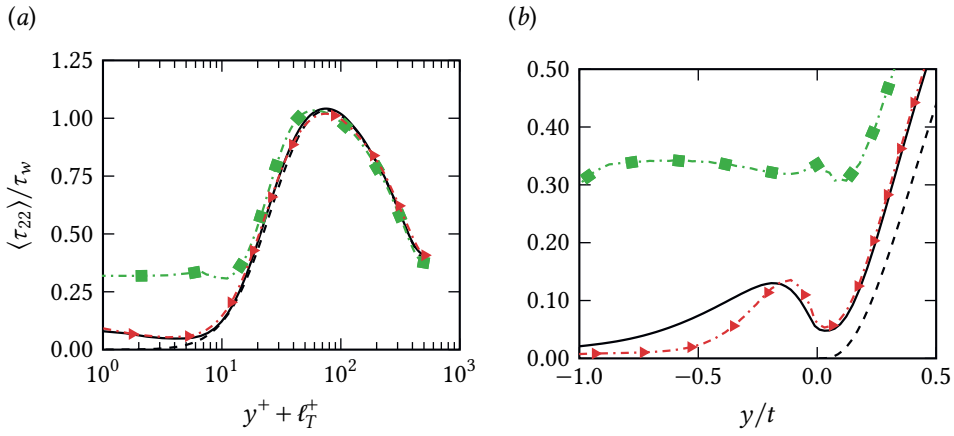

Figure 5.6: Wall normal Reynolds stress τ_{22}, as a function of the viscous-scaled wall distance (*a*) and as a function of y/t (*b*), where t is the plate thickness, for smooth wall flow case (dashed line without symbols), the baseline liner flow case (solid line without symbols) and novel liner flow cases *L-*E_{x-3} (squares) and *L-*E_{z-3} (triangles).

for flow case $L\text{-}E_{x-3}$ are correlated with the significantly higher drag of this case.

Furthermore, we find that liner cases with lower drag present lower wall-normal velocity fluctuations and a more smooth-wall-like organization of the near-wall flow. These qualitative observations suggest that the correlation that relates the added drag and the intensity of the wall-normal velocity fluctuations holds for all facesheet geometries under scrutiny.

For a more quantitative analysis, we further show the wall-normal Reynolds stress components $\tau_{22} = \widetilde{\overline{\rho}v''v''}$ in Fig. 5.5 and 5.6. It is clear that the wall-normal velocity fluctuations are not zero, irrespective of the case considered, above and below the facesheet. We find that flow cases that exhibit lower drag than the baseline liner show lower wall-normal velocity fluctuations in the near-wall region and below the facesheet, Fig. 5.5. The converse is true for cases that increase the added drag, Fig. 5.6.

5.2.2 Acoustic Attenuation

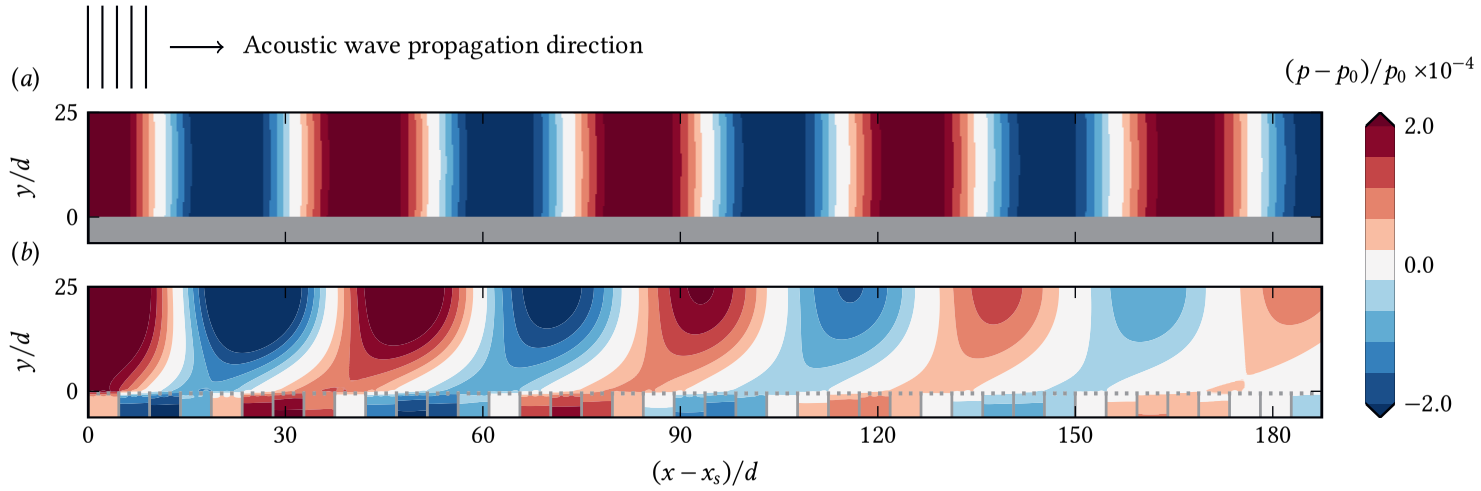

Figure 5.7: Instantaneous pressure fluctuations over the smooth wall (*a*) and the baseline liner (*b*). p_0 is the reference thermodynamic pressure. Sound propagation direction is from left to right. x_s is the streamwise location where the liners start.

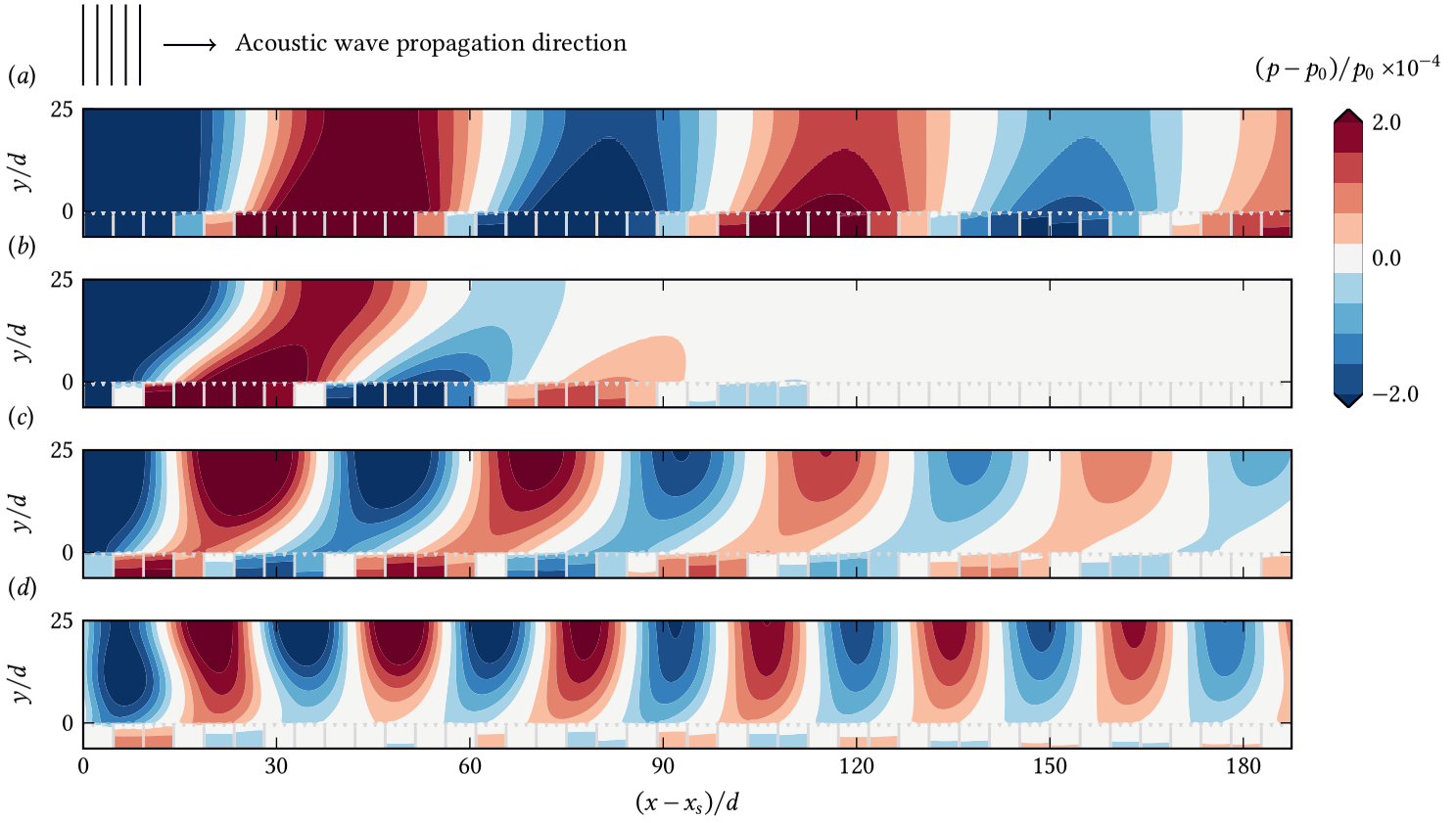

Figure 5.8: Instantaneous pressure fluctuations for the tapered orifice configuration for various acoustic wave frequencies f/f_r= 0.5 (*a*), 0.75 (*b*), 1.0 (*c*) and 1.5 (*d*).

We have studied the aerodynamic drag of different orifice configurations and have identified several geometries that induce lower drag compared to the baseline liner with circular orifices. As acoustic liners are used to reduce engine noise, it is imperative to also test their acoustic performance. In order to do so, we study the noise attenuation properties of these novel configurations in the absence of grazing flow. A complete picture of the noise attenuation properties of aerodynamically optimised acoustic liner geometries would require including the influence of grazing flow. However, studies of acoustic liners without grazing flow have been extensively used to provide an initial estimation of their acoustic performance [6, 119, 88]. Simulations in the absence of grazing flow allow us to study the acoustic performance over a range of frequencies for all geometries considered at tractable computational cost.

Simulations are performed in a channel of size $L_x \times L_y \times L_z = 1250d \times (25d + h) \times 4.69d$, where d is the orifice diameter of the baseline liner and $h = 6.25d$. The spanwise domain size corresponds to a single cavity, and periodic boundary conditions are applied in the spanwise direction. We apply no-slip isothermal boundary conditions on the top and bottom walls and place acoustic liners at the bottom wall of the channel. An array of 40×1 acoustic liner cavities is placed between $x_s = 500d$ and $x_e = 687.5d$. The geometries of the liners are the same as those considered when studying the aerodynamic performance. The angular resonance frequency of the system is expected to be approximately $\omega_r \approx 0.056\pi c/d$. However, the correction due to the pressure field, particularly for the geometries considered in the paper, is difficult to estimate. We, therefore, test the performance of the novel geometries over a range of frequencies from $\omega/\omega_r = 0.5$ to $\omega/\omega_r = 1.5$ at a Reynolds number $Re_c = 800$ based on the orifice diameter and speed of sound. We verified that, while the absolute sound attenuation of these liners changes, the relative sound attenuation, compared to the baseline acoustic liner, does not depend on the Reynolds number.

Figure 5.7 shows an instantaneous snapshot of the pressure for the smooth wall case and the baseline liner, for the case with $\omega = \omega_r$. Figure 5.8 also shows how the instantaneous pressure field changes as the forcing frequency is changed. As the frequency of the acoustic wave is tuned to the resonant frequency of the liner, we see a significant attenuation of the acoustic wave over the liner. The amplitude of the pressure fluctuations towards the end of the acoustic liner is much lower than over the smooth wall, where the fluid viscosity is the only dissipative mechanism.

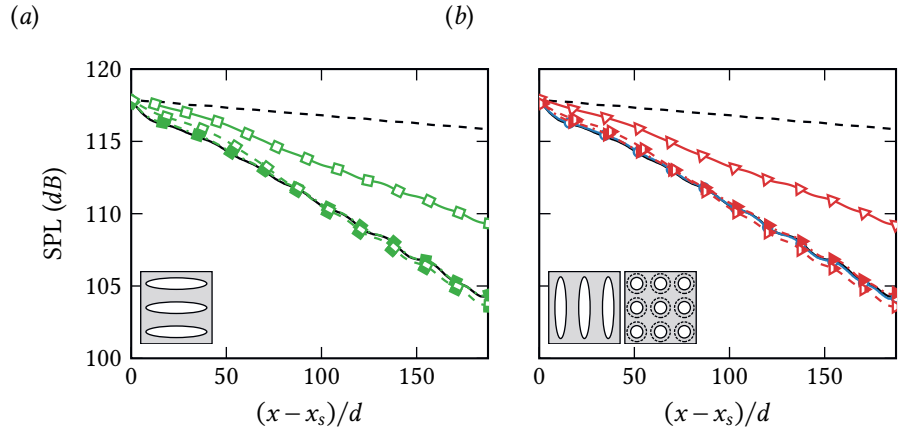

Figure 5.9: Sound pressure level as a function of the streamwise distance from the start of the liners for smooth wall flow case (dashed line without symbols), the baseline liner flow case (solid line without symbols) and novel liner flow cases *L-T* (circles), $L\text{-}E_{x-\chi}$ (squares) and $L\text{-}E_{z-\chi}$ (triangles). Different line types with symbols indicate the number of orifices per cavity: $\chi = 3$ (dash-dotted line with filled symbols), $\chi = 6$ (dashed line with half-filled symbols) and $\chi = 9$ (solid line with empty symbols).

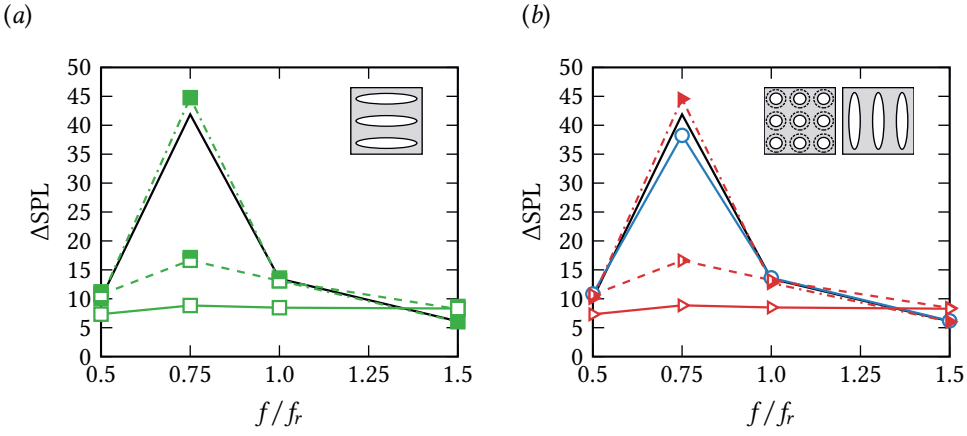

Figure 5.10: Sound pressure level as a function of the forcing frequency. Different line types represent different cases: *L-T* (circles), $L\text{-}E_{x-\chi}$ (squares) and $L\text{-}E_{z-\chi}$ (triangles). Different line types with symbols indicate the number of orifices per cavity: $\chi = 3$ (dash-dotted line with filled symbols), $\chi = 6$ (dashed line with half-filled symbols) and $\chi = 9$ (solid line with empty symbols).

Figure 5.9 compares the SPL evolution of the acoustic wave for all the liner configurations and the smooth wall, for the case with $\omega = \omega_r$. Although there is a clear SPL reduction for all configurations as compared to the smooth wall, some geometries perform better than others when evaluated against the baseline liner. This is true for the SPL loss over the entire frequency range considered, see Fig. 5.10. Cases $L\text{-}E_{x-3}$ and $L\text{-}E_{z-3}$, offer very similar acoustic noise attenuation over the entire frequency range, however, the narrow orifices of cases $L\text{-}E_{x-6}$, $L\text{-}E_{z-6}$, $L\text{-}E_{x-9}$ and $L\text{-}E_{z-9}$, that helped reduce drag, appear to inhibit acoustic noise attenuation. Cases $L\text{-}E_{x-6}$ and $L\text{-}E_{z-6}$ show similar noise attenuation properties at frequencies other than $f = 0.75 f_r$, whereas cases $L\text{-}E_{x-9}$ and $L\text{-}E_{z-9}$ show significantly lower attenuation throughout the frequency range. The tapered hole configuration provides comparable acoustic noise attenuation as compared to the standard acoustic liner. Figure 5.10 also shows that the effective resonance frequency is about 25% lower than the nominal one, that we estimated disregarding entrance and exit effects. Notably, the resonant frequency appears to be about the same for all orifice shapes, suggesting that the required correction for entrance and exit effects is similar for all orifice shapes. The tapered holes, therefore, improve not only the aerodynamic performance of the liner but also perform well acoustically. The elliptical orifices, however, depending upon the width of the orifice, may or may not have a detrimental influence on acoustic noise attenuation.

6

Acoustic Liners and a Growing Boundary Layer

Parts of this chapter have been published in AIAA Journal - In print.

Channel flow simulations are invaluable tools to understand how complex geometries would interact with turbulent flows. Their (relatively) cheap nature is what afforded the parametric simulations we have presented in the previous chapter and have aided us in grasping better how acoustic liners behave and which parameters can be tuned for a more aerodynamically efficient acoustic liner. However, in realistic operating conditions, acoustic liners are not only subject to a growing boundary layer, but high-amplitude acoustic fluctuations on top of turbulence. The present chapter extends the channel flow simulations, by studying a more realistic numerical setup, by performing DNS of a turbulent boundary layer over fully resolved acoustic liner arrays. The aim of this work is two-fold: i) we aim to validate our previous findings, obtained using a bi-periodic channel flow configuration, using the more realistic case of a developing boundary layer, which also allows us to introduce acoustic waves and assess their influence on the flow. ii) we study the adjustment of the flow to a step change in permeability, which is common in engineering applications. The considered setup, methodology and results are detailed in the following section.

6.1 Methodology

We perform DNS of a turbulent boundary layer over acoustic liners using the flow solver STREAmS [114, 70]. The simulation is performed in a rectangular box of size $L_x \times L_y \times L_z = 115\delta_0 \times (15\delta_0 + k) \times 5\delta_0$, where δ_0 is the inflow boundary layer thickness, and k is the depth of the acoustic liner, and x,y and z are the streamwise, wall-normal and spanwise directions respectively. We note that the boundary layer thickness grows in the streamwise direction, thus the effective box dimensions become smaller, compared to the local boundary layer thickness δ. At the outflow, the spanwise size of our domain approaches $L_z \approx 2\delta$. This domain size may seem small in absolute terms, however, similar and even smaller spanwise domains have been used previously to aid parametric analysis of rough wall turbulent flows [120, 121, 90, 91, 92, 93], including our previous turbulent plane channel flow simulations in chapter 4, where we used. For rough wall turbulent flow simulations smaller computational box sizes are accepted for two reasons: i) they relax the higher computational cost that is required to resolve the roughness and ii) the main interest when studying roughness is in the log layer, which is not affected by small box dimensions, as demonstrated by Chung et al. [90].

The freestream Mach number is $M_\infty = u_\infty / c_\infty = 0.3$, where u_∞ is the freestream velocity and c_∞ is the speed of sound based on freestream conditions, and the friction Reynolds number is $Re_\tau = \delta/\delta_v \approx 850–2600$. The domain consists of an initial smooth wall region

Case	σ	Re_τ	δ/δ_0	$\Delta x^+_{\max}$	$\Delta y^+_{\min}$	$\Delta z^+_{\max}$	$f\delta_0/u_\infty$	SPL (dB)
L_1	0.322	854–2587	0.86–2.43	8.26	0.79	5.55	0	0
L_2	0.322	861–2601	0.86–2.47	8.51	0.81	5.72	0.422	150

Table 6.1: DNS parameters for the two boundary layer cases considered, L_1 and L_2, in the absence and presence of acoustic waves. The computational domain has dimensions $L_x \times L_y \times L_z = 115\delta_0 \times 15\delta_0 + k \times 5\delta_0$ and the number of mesh points is $N_x \times N_y \times N_z = 21504 \times 672 \times 1120$. σ is the porosity (open area ratio). Re_τ and δ/δ_0 are the friction Reynolds number and the local boundary layer thickness. Δx^+, Δy^+ and Δz^+ are the viscous-scaled mesh spacings in the streamwise, wall-normal and spanwise directions.

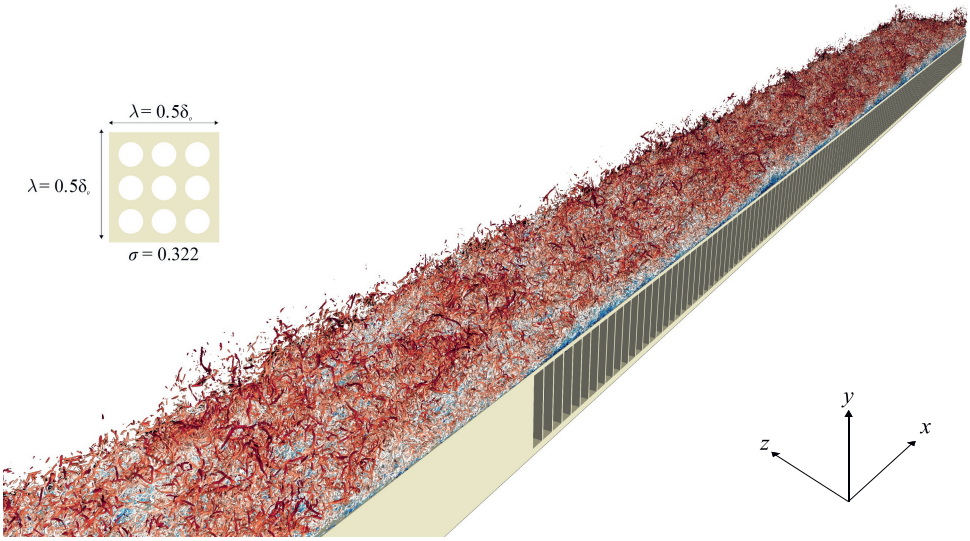

Figure 6.1: Instantaneous flow field of the boundary layer simulation. Orifice configurations within a single cavity are also shown at the top left. Vortical structures are visualised using the Q-Criterion, coloured by the streamwise velocity.

of streamwise length $L_{x,s} = 45\delta_0$, followed by an acoustic liner array that extends from $x = 45\delta_0$ to the end of the domain, $x = 115\delta_0$. The equations are discretized on a Cartesian grid with a mesh size $N_x \times N_y \times N_z = 21504 \times 672 \times 1120$. The mesh spacing is constant in the spanwise direction and points are clustered in the wall-normal direction at the liner facesheet and coarsened towards the backplate and the freestream. The mesh points are slightly clustered close to the transition point between the smooth wall and the liner and have a constant spacing over the liner. The orifice geometry is resolved by 24 points in the streamwise and spanwise directions to resolve the orifice geometry. This mesh resolution has been verified in chapter 4, where we carried out a mesh refinement study showing that this number of points yields have grid converged results. Details of the simulation are summarised in Table 6.1. A characteristic non-reflecting boundary condition is used at the top boundary. At the inflow and the outflow, the non-reflective condition is augmented with relaxation [78] to impose a realistic turbulent profile at the inflow, and the pressure value at the outflow. At the inflow, we impose the mean streamwise velocity obtained from the composite profile of Musker [74] with superposed turbulent velocity fluctuations from a recycling-rescaling procedure [76, 122]. The recycling plane is located at $x/\delta_0 = 40$, at a distance $5\delta_0$ upstream of the point of transition from the smooth wall to the liner. Periodic boundary conditions are used in the spanwise direction. The geometry, consisting of the smooth wall and the liner, is resolved using a ghost-point immersed boundary method [85] enforcing a non-slip adiabatic boundary condition.

The geometry of the acoustic liners is chosen to match as closely as possible a realistic acoustic liner in operating conditions. Our cavity geometry has a square cross-section with a side length $\lambda = 0.5\delta_0$ and depth $k = 2.0\delta_0$. Each cavity has 9 orifices with a diameter corresponding to a porosity of $\sigma \approx 0.322$. The geometry of the facesheet is similar to

the one studied in our channel flow simulations (chapter 4) at $\sigma \approx 0.322$ and thickness to diameter ratio $t/d = 1$. The domain consists of a total of 140×10 acoustic liner cavities in the streamwise and spanwise directions. An instantaneous flow visualisation of the flow field is shown in Figure 6.1 where vortices are visualised using the Q criterion. The top view of a single cavity depicting the distribution of orifices is also shown in figure 6.1. The figure shows the complex organisation of the turbulent structures and the growth of the boundary layer in the streamwise direction. Statistics are averaged in the spanwise direction and in time. Statistics are also averaged in the streamwise direction over a single cavity representing a streamwise extent of $\approx 0.5\delta_0$, to ensure better statistical convergence. Statistics are collected every $\Delta t \approx 0.3\delta_0/u_\infty$ for a total time of $t_{\text{tot}} = 150\delta_0/u_\infty$. We estimated the extent of convergence by residual of the streamwise mean momentum balance,

$$\frac{\partial}{\partial x}(\overline{\rho}\tilde{u}\tilde{u}) + \frac{\partial}{\partial y}(\overline{\rho}\tilde{u}\tilde{v}) = -\frac{\partial \overline{p}}{\partial x} - \frac{\partial}{\partial y}(\widetilde{\overline{\rho}u'v'}) + \frac{\partial}{\partial y}\left(\overline{\mu}\frac{\partial \tilde{u}}{\partial y}\right). \tag{6.1}$$

The residual of (6.1) $R(x,y)$ is integrated in the wall-normal direction,

$$\epsilon(x) = \left(\frac{1}{h}\int_0^\delta R(x,y)^2 \mathrm{d}y\right)^{1/2} \tag{6.2}$$

and we find that its maximum value nowhere exceed $\epsilon/(\rho_w u_\tau/\delta_v) \approx 4 \times 10^{-3}$. This value is in line with the convergence criterion proposed by Vinuesa et al. [123] for plane channel and square duct flow.

6.1.1 Sound waves

We perform two boundary layer simulations L_1 and L_2 with identical setup, apart from that the latter features incoming acoustic waves. When present, acoustic waves are introduced at the outflow boundary, where the outflow pressure is relaxed towards a target value $p_o(T) = p_0 + A\cos(2\pi f_o T)$, which oscillates around the reference freestream thermodynamic pressure p_0 with amplitude A, and T is time and $f_0 = c/(2\pi)\sqrt{O_A/t'V} \approx 0.422u_\infty/\delta_0$ is the resonance frequency of the liner. c is the speed of sound, O_A is the area of the orifices, $t' = t + 1.6\sqrt{A/\pi}$ is the thickness of the orifice corrected for the influence of the pressure field on the apparent mass of air in the orifice, and V is the volume of the cavity [7, 124, 125]. For case L_1, no sound wave is imposed at the outflow and the amplitude of the sound wave is set to zero. For case L_2, sound waves with a sound pressure level, $\text{SPL} = 150dB$ are imposed at the outflow. The corresponding amplitude is $A = p_r \cdot 10^{\text{SPL}/20}$, where $p_r = 20 \times 10^{-6}$Pa is a reference pressure.

The reason for choosing a 150dB amplitude is motivated by previous studies who used amplitudes in the range 130-150dB. We decided to pick a value in the upper range in the attempt to maximize the effect on the turbulent boundary layer. We introduce acoustic waves at the outflow traveling upstream. This is partially motivated by our turbulent inflow generation based on a recycling/rescaling technique, which would be more cumbersome to implement with the addition of incoming noise. Introducing acoustic noise at the inflow traveling downstream, would have been also a valid option, and it has been pursed by other authors [126]. It is worth noting that noise directionality matters in the presence of a grazing flow [126]. We note that acoustic waves coming from the outflow are closer to

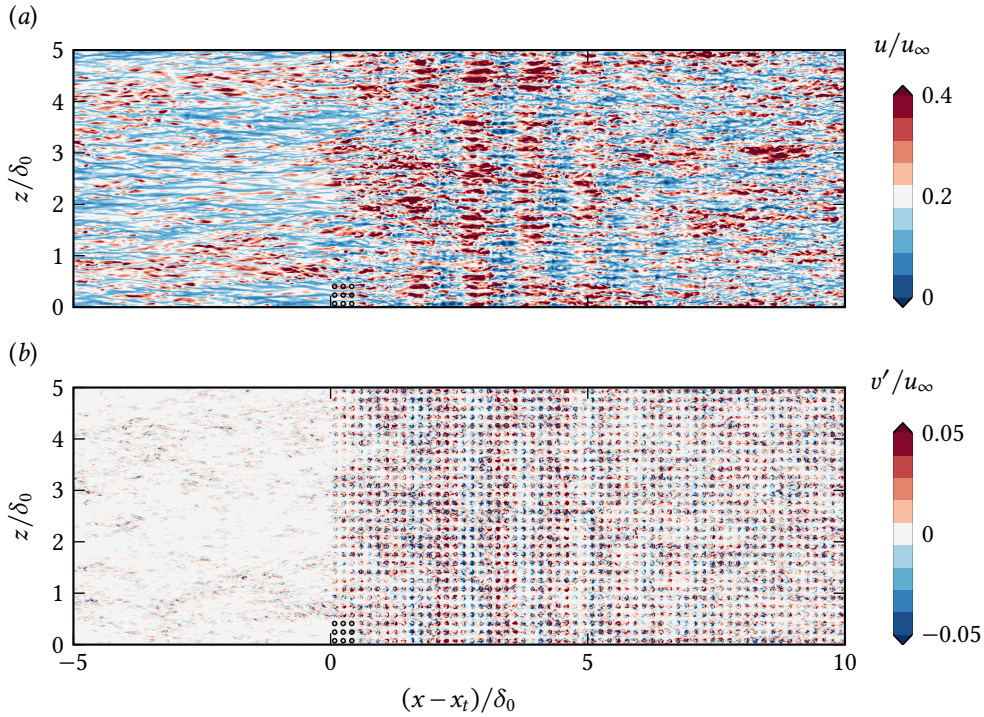

Figure 6.2: Instantaneous streamwise velocity (*a*) and wall-normal velocity fluctuations (*b*) in a wall parallel plane at $y/\delta_0 = 0.005$. The position of the orifices is shown for a single cavity at the smooth-to-porous transition. x_t represents the streamwise location of the smooth-to-porous transition point.

the case of acoustic liners in the aircraft engine intake [127] where noise is coming from the fan and traveling upstream the boundary layer. However, we also point out that in real conditions acostic waves are reflected and scatterd on the walls of the engine and the aircraft, thus acoustic waves come from other directions as well.

To prevent interaction of acoustic waves with the recycling, selective frequency damping (SFD) [80, 81, 82] was used. SFD is used between $x/\delta_0 = 0$ and $x/\delta_0 = 70$ and is above the boundary layer height. The control parameter χ is ramped up linearly in the upstream direction from $\chi = 0$ at $x/\delta_0 = 70$ to $\chi = \chi_{\max} = 0.8$ for $x/\delta_0 < 45$.

6.2 Turbulent boundary layer without sound waves

6.2.1 Instantaneous flow field

An instantaneous flow visualisation of the flow field is shown in Fig. 6.1, where vortices are visualised using the Q criterion. The figure shows the complex organisation of the turbulent structures and the growth of the boundary layer in the streamwise direction. Additional insight on the flow can be gained by inspecting wall-parallel planes close to the wall. Figure 6.2 shows the streamwise and wall-normal instantaneous velocity on an

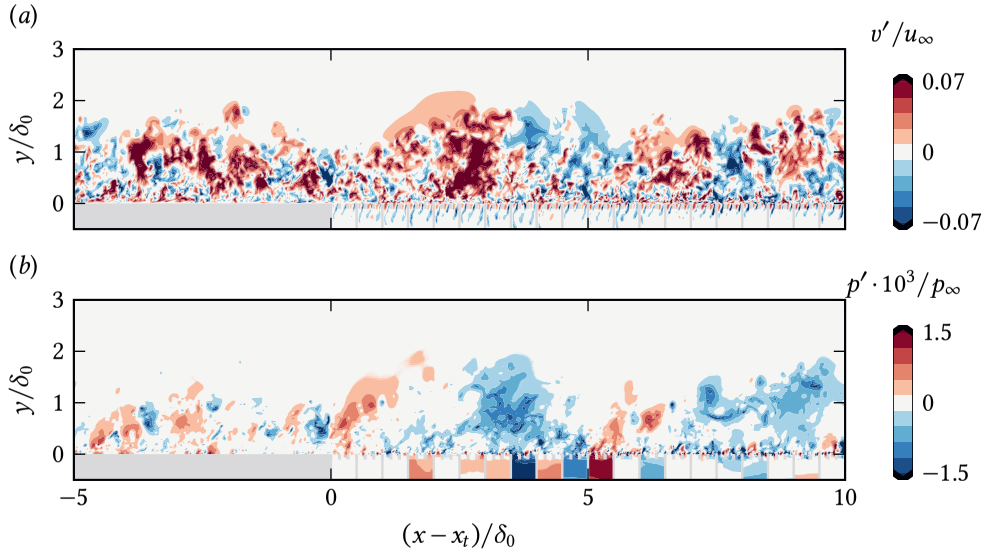

Figure 6.3: Instantaneous wall-normal velocity (*a*) and pressure fluctuations (*b*) in an x-y plane. x_t represents the streamwise location of the smooth-to-porous transition point.

$x-z$ plane over the smooth-to-liner transition region. Compared to the smooth wall, the liner leads to very high wall-normal velocity fluctuations near the surface of the facesheet, see Fig. 6.2 **(*b*)**. High-velocity magnitudes tend to be concentrated around the orifices. Wall-normal velocity fluctuations have been previously observed to play an important role in altering the near wall cycle [105, 115, 97], and have been proposed as the mechanism that leads to the drag increase over acoustic liners by Wilkinson [10] and also in chapter 4. Compared to the smooth wall, the streamwise velocity contours are also significantly altered, see Fig. 6.2 **(*a*)**. High-speed and low-speed streaks, typical of near-wall turbulence, are perturbed by the significant wall-normal velocity fluctuations at the wall and, thus, break down over the liner. Immediately after the smooth-to-porous transition, between $(x-x_t)/\delta_0 \approx 2$ and $(x-x_t)/\delta_0 \approx 5$, there exists a small region where the flow over the liner appears marginally distinct from the flow further downstream. The wall-parallel planes show a spanwise coherent flow organization, resembling Kelvin–Helmholtz-like structures, which have generally been previously observed over porous surfaces [50, 128] and riblets [129].

The high wall-normal velocity fluctuations induced by the liner are due to the interaction of the flow above and below the facesheet, evidence of which can be seen in Fig. 6.3 **(*a*)**, showing wall-normal velocity and pressure fluctuations in an $x-y$ plane. A jet-like flow is observed penetrating into the cavities, indicating high inertial effects inside the liner. In chapter 4, we noted that this jet-like flow is a result of pressure fluctuations redistributing energy into wall-normal velocity fluctuations. Figure 6.3 **(*b*)** shows contours of the pressure fluctuations in an $x-y$ plane. In a similar fashion to the wall-normal velocity fluctuations, pressure fluctuations significantly increase as the flow passes from the smooth wall to the liner, particularly close to the wall. High-pressure regions are observed closer to the downstream edge of the orifice, hinting at an increase in pressure drag over acoustic liners. Chapter 4 showed that pressure drag significantly increases over a liner, reaching nearly 50% of the total drag of the surface in their channel-flow simulations. We also note that the cavity and orifice pressure seem to respond to the large-scale structures in the boundary layer.

6.2.2 The Internal Boundary Layer

We continue our discussion by investigating how the flow reacts to the step change in permeability. To calculate the height of the IBL, we use the method proposed by Cheng and Castro [43] who used the point where the downstream velocity is 99% of the upstream velocity before the surface transition at the same wall-normal location and reported a growth rate of the internal boundary layer thickness $\delta_I \propto (x-x_t)^{0.33}$. Here, the method proposed by Cheng and Castro [43] is used because it is found to be more robust than the one by Elliott [42] which requires the identification of two logarithmic regions in the mean velocity profile, leading to a larger uncertainty for the present simulations.

Figure 6.4 **(*a*)** shows a graphical representation of the method by Cheng and Castro [43] to calculate the IBL height. The heights of the IBL, at three different streamwise locations, are marked with large encircled crosses, indicating the point where the velocity at the three streamwise locations, is 99% of the upstream velocity at the same wall-normal location. The growth of the IBL is shown in Fig. 6.4 **(*b*)**, along with the growth rates suggested by Cheng and Castro [43] and Elliott [42]. The adjustment of the streamwise velocity profile is quick

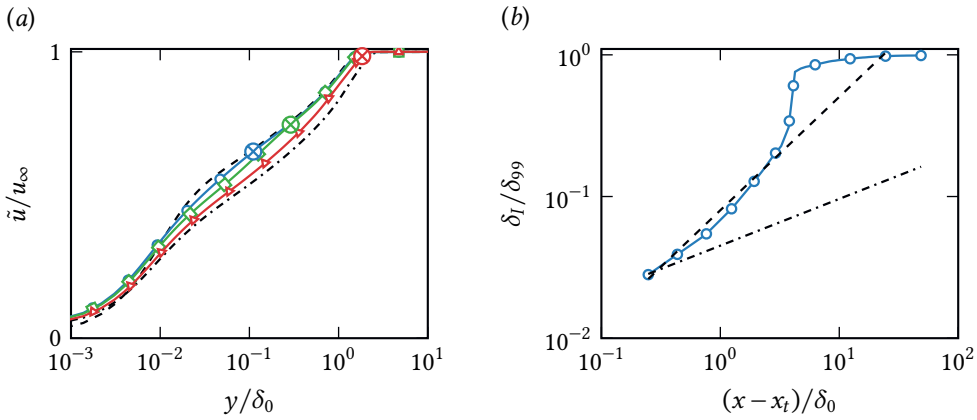

Figure 6.4: Evaluation of the internal boundary layer using the streamwise velocity as in Cheng and Castro [43]. In (*a*), the solid line with symbols represents the streamwise velocity downstream of the smooth-to-porous transition point at $(x-x_t)/\delta_0 \approx 1.25$ (circles), 5 (squares) and 25 (triangles), the dashed line represents the upstream velocity profile over the smooth wall and the dashed-dotted line represents the liner velocity profile, significantly downstream of the transition point. The red cross is used to identify the wall-normal location of the internal boundary layer. In (*b*), the growth of the internal boundary layer in the streamwise direction (circles) is compared to growth rate suggested by Elliott [42] (dashed line - $\delta_I \propto (x-x_t)^{0.8}$) and Cheng and Castro [43] (dash-dotted line - $\delta_I \propto (x-x_t)^{0.33}$).

and the height of the IBL is approximately equal to the local boundary layer thickness at a distance $10\delta_0$ downstream of the smooth-liner transition, similar to the permeable surfaces considered by Efstathiou and Luhar [34]. Compared to the growth rate suggested by Cheng and Castro [43], the present IBL grows at a quicker pace. The growth rate of the IBL matches the growth rate suggested by Elliott [42] in the immediate vicinity of the transition point. However, the growth rate for the acoustic liner is not constant and increases downstream, recovering faster than what was suggested by Elliott [42]. Figure 6.6 that shows the IBL location superimposed on top of the wall-normal gradient of the mean streamwise velocity. One could argue that the development of the Kelvin-Helmholtz-like structures cause more intense mixing and momentum transfer, leading to a quicker adjustment of the mean streamwise velocity. The recovery of the streamwise velocity is, therefore, faster over an acoustic liner than over canonical roughness.

However, the adjustment of the streamwise Reynolds stress is much slower. Efros and Krogstad [45] used profiles of the streamwise Reynolds stress to estimate the thickness of the IBL, as represented in Fig. 6.5 ***(a)***, where the IBL thickness is estimated to be at the intersection between the two linear regions in the streamwise Reynolds stress. Figure 6.5 ***(b)*** shows the height of the IBL, estimated with this method, as a function of distance downstream of the smooth-liner transition. The growth initially matches that suggested by Efros and Krogstad [45] of approximately $\delta_I \propto (x-x_t)^{0.7}$, but deviations are visible further downstream, most probably associated with the large uncertainty in accurately fitting two linear regions in the streamwise Reynolds stress. Therefore, we believe we can assume that the recovery of streamwise Reynolds stress, follows similar trends as canonical roughness. If the growth rate suggested by Efros and Krogstad [45] is extrapolated, the IBL approaches

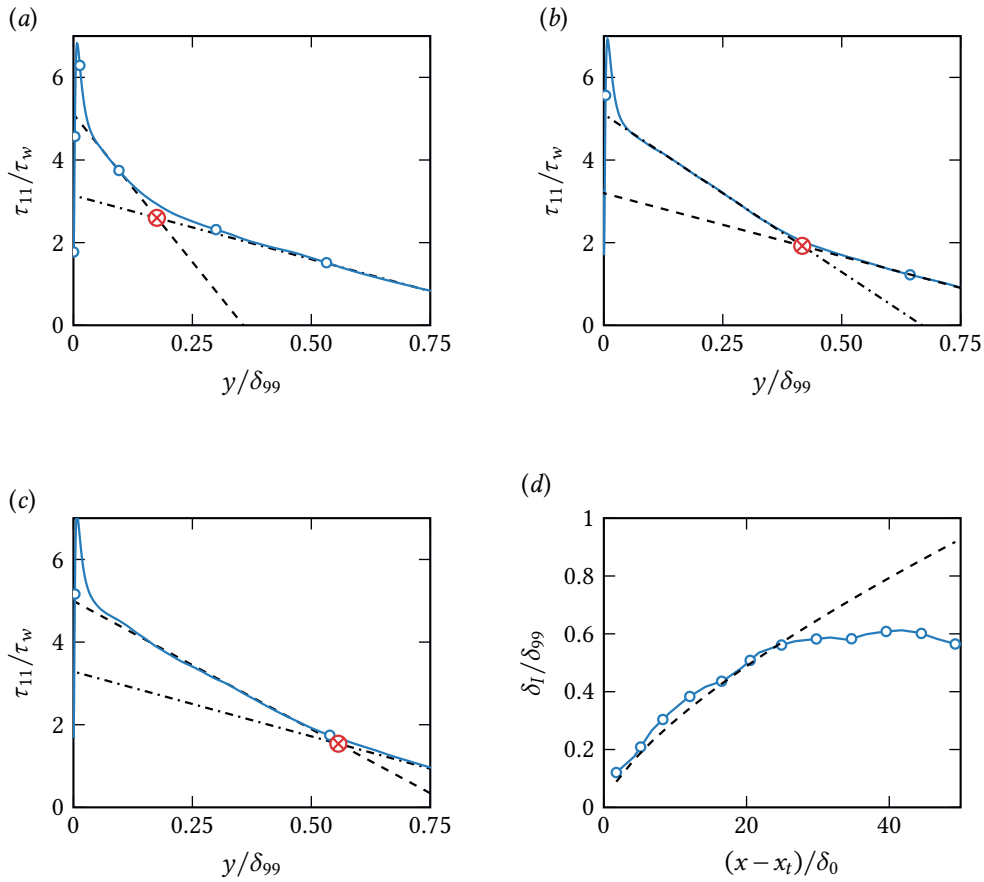

Figure 6.5: Evaluation of the internal boundary layer using the streamwise Reynolds stress as proposed by Efros and Krogstad [45]. In (*a*)–(*c*), the solid line with circles represents the streamwise Reynolds stress downstream of the smooth-to-porous transition point at $(x-x_t)/\delta_0 \approx 4$ (*a*), $(x-x_t)/\delta_0 \approx 15$ (*b*) and $(x-x_t)/\delta_0 \approx 25$ (*c*) and the dashed and dash-dotted lines are linear fits to the two straight line segments of the streamwise Reynolds stress. The intersection of the two lines shown by the red cross is the wall-normal location of the internal boundary layer. In (*d*), the growth of the internal boundary layer in the streamwise direction (circles) is compared to the growth rate suggested by Efros and Krogstad [45] (dashed line - $\delta_I \propto (x-x_t)^{0.7}$).

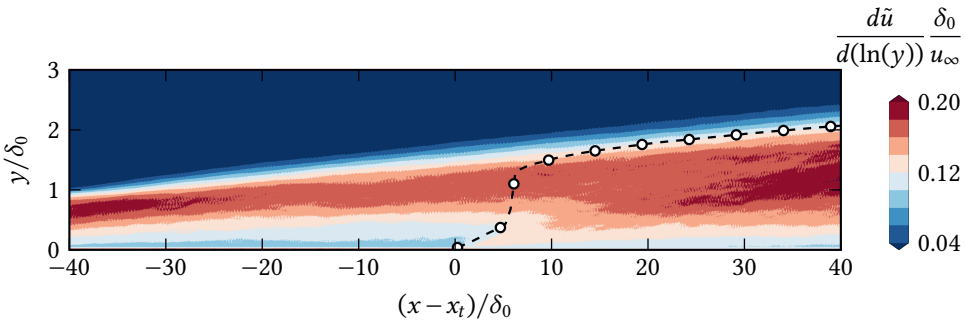

Figure 6.6: Wall-normal gradient of the streamwise velocity. The markers indicate the location of the IBL.

approximately 90% of the local boundary layer thickness towards the end of the domain, therefore, it can be safely assumed that the Reynolds stresses do not reach equilibrium in the present simulations.

6.2.3 Mean flow and skin-friction

Figure 6.7 shows the friction coefficient, C_f, and the friction Reynolds number, Re_τ, as a function of the Reynolds number based on the streamwise distance from the virtual leading edge. Both the friction Reynolds number and the friction coefficient tend to overshoot at the smooth-to-porous transition as the flow tries to adjust itself to the new flow conditions. Away from the transition location, the overshoot in the friction coefficient decreases, but drag remains higher than for the smooth wall.

The added drag is also visible in the mean streamwise velocity over the liner, shown in Fig. 6.8 **(*a*)**. Velocity profiles past the smooth-to-liner transition point show a downward shift as compared to the smooth wall. Furthermore, differences between the smooth wall and liner velocity profiles are limited to the near the wall region, and the velocity profiles are essentially parallel in the outer layer, indicating that Townsend's outer layer similarity hypothesis holds for the streamwise velocity. The streamwise velocity profiles over the liner exhibit a nearly constant ΔU^+, see Fig. 6.9 **(*a*)**, apart from a small region near the smooth-to-liner transition point.

Differences between the smooth wall and the liner are visible in the Reynolds Stresses, $\tau_{ij} = \overline{\rho}\widetilde{u_i'' u_j''}$, shown in Fig. 6.8 **(*b*)**. We compare the results of the liner case with the smooth-wall cases of Eitel-Amor et al. [131] at approximately matching friction Reynolds number. Deviations from the smooth wall Reynolds stresses are visible close to the wall. Irrespective of the velocity component, non-zero Reynolds stresses exist near the wall for the liner, which enhance momentum transfer and contribute to the added drag. The non-zero wall-normal velocity fluctuations near the wall, also evident in the instantaneous flow in Fig. 6.2 **(*b*)**, are responsible for the breakdown of the classical near-wall turbulence cycle and a reduction in the streamwise Reynolds stress peak. The peak streamwise Reynolds stress decreases over the acoustic liner and the peak spanwise and wall-normal velocity fluctuations increase with respect to the smooth wall, in contrast to our channel

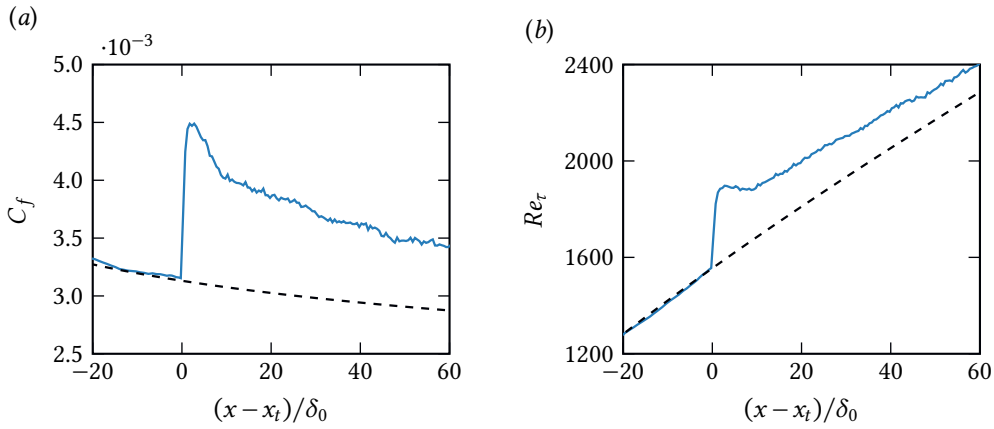

Figure 6.7: Variation of the friction Reynolds number (*a*) and the skin-friction coefficient (*b*) for the boundary layer simulation with the distance from the smooth-to-porous transition point. Solid lines show the boundary layer simulation results and the dashed lines show smooth wall Re_τ and C_f, approximated using $C_f = (2\log_{10})(Re_x) - 0.65)^(- 2.3)$ [130], where a virtual origin is used to calculate Re_x by matching DNS results for using skin friction data at the inflow.

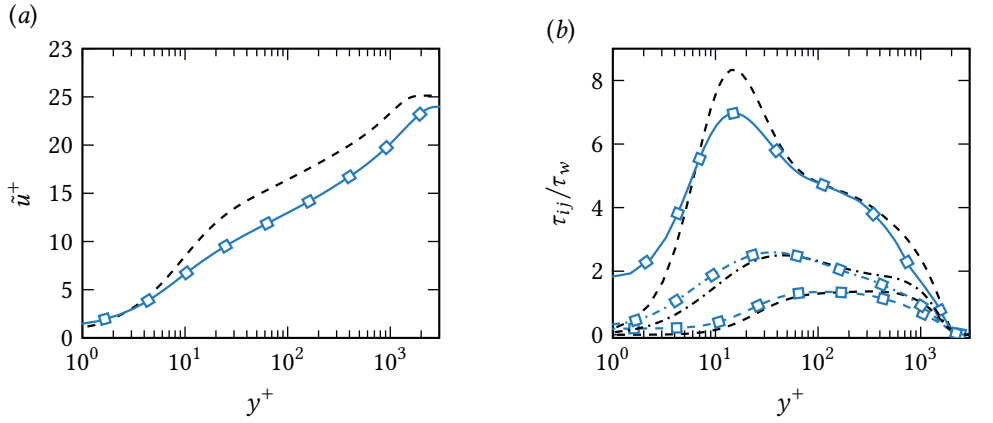

Figure 6.8: Mean streamwise velocity (*a*) as a function of the wall-normal coordinate. Different line types represent different streamwise locations in panel (*a*): triangles ($(x - x_t)/\delta_0 \approx 45$) and dashed line ($(x - x_t)/\delta_0 \approx -5$). Streamwise (solid), wall-normal (dashed) and spanwise (dashed-dotted) Reynolds stresses (*b*) over the acoustic liner (lines with triangles) compared to the smooth wall data of Eitel-Amor et al. [131] (lines) at friction Reynolds number, $Re_\tau \approx 1940$.

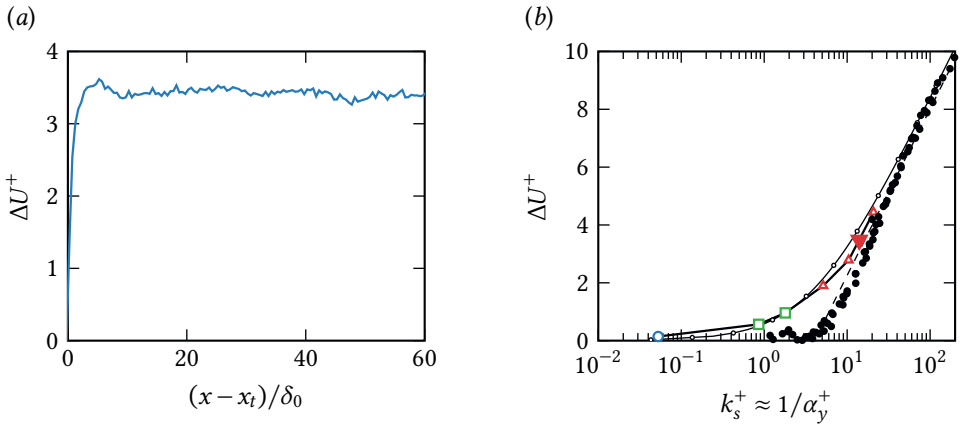

Figure 6.9: ΔU^+ as a function of the distance from the transition point (*a*) and as a function of the viscous-scaled inverse of the Forchheimer coefficient (*b*). The filled inverted triangle represents ΔU^+ of the current simulation whereas the empty symbols represent data of channel flow simulations. Filled circles are Nikuradse's data for sandgrain roughness and the dash-dotted line represents data for Colebrook type roughness [14].

flow simulations in chapter 4, for which we observed only an increase in the peak of the spanwise velocity fluctuations. Differences can be observed in the outer layer because the Reynolds stresses are not in equilibrium yet.

6.2.4 Acoustic liners as a permeable substrate

In chapter 4, we analysed several candidate length scales for acoustic liners and observed that the inverse of the viscous-scaled non-linear (Forchheimer) permeability, $1/\alpha^+$, is the relevant length scale for acoustic liners. We attribute this to the very high inertial effects that may be observed inside the orifices. The present boundary layer results also support this finding, as shown by Fig. 6.9 ***(b)*** where we report ΔU^+ as a function of the viscous-scaled inverse of the Forchheimer coefficient, which follows exactly the trend observed in the channel flow simulations, and matches remarkably well the correlation proposed for ΔU^+ in the seminal work of Colebrook [14]. The good match with our channel flow data is despite different cavity depth of, $k/\delta = 0.822$–1.267 for our boundary layer simulation as compared to $k/\delta = 0.5$ for the channel flow simulations, where δ is the local boundary layer thickness and the channel half width, respectively. The cavity depth, therefore, does not play a significant role in determining liner behaviour in the absence of sound waves.

Acoustic liner drag not being affected by cavity depth is in line with previous observations by Howerton and Jones [11], who noted that, in the absence of acoustic excitation, liner drag is not changed by changing the cavity depth. Therefore, the aerodynamic properties of acoustic liners are determined by the permeability of the facesheet and the orifice geometry. The latter was also confirmed in chapter 5.

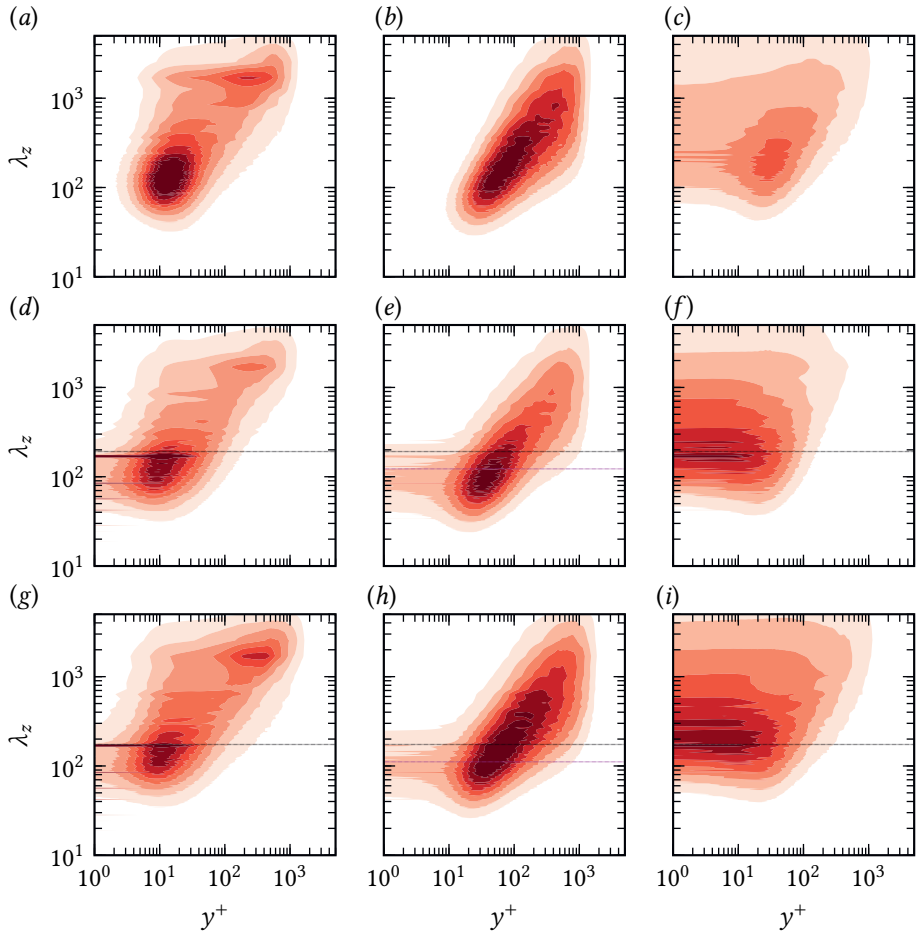

Figure 6.10: Premultiplied streamwise, $\kappa_z^+ E_{u,z}/u_\tau^2$, ((*a*), (*d*)), wall-normal, $\kappa_z^+ E_{v,z}/u_\tau^2$, ((*b*), (*e*)), and pressure, $\kappa_z^+ E_{p,z}/\tau_w^2$, ((*c*), (*f*)) spectral densities as a function of the viscous-scaled wall-normal distance for smooth wall ($(x-x_t)/\delta_0 \approx -5$) ((*a*)–(*c*)) and liner ($(x-x_t)/\delta_0 \approx 45.25$) ((*d*)–(*f*)). λ_z^+ is the viscous-scaled spanwise wavelength and κ_z is the spanwise wavenumber.

6.2.5 Spectral Densities

The instantaneous flow showed significant differences between the smooth wall and the liner, indicating, a difference in the organisation of turbulence. Spectral analysis can provide further insight and a more quantitative view into how the acoustic liner influences the turbulent flow organisation. Figure 6.10 shows the pre-multiplied spanwise spectral densities of the streamwise, $\kappa_z^+ E_{u,z}/u_\tau^2$, and wall-normal velocity, $\kappa_z^+ E_{v,z}/u_\tau^2$, components as a function of the wall-normal distance from the virtual origin and the spanwise wavelength λ_z, for flow cases *L-L*$_{32}$, *L-M*$_{32}$ and *L-H*$_{32}$. The spectral densities are defined such that,

$$\widetilde{f''^2} = \int_{-\infty}^{+\infty} E_f(\kappa_z)\mathrm{d}\kappa_z, \tag{6.3}$$

where κ_z is the spanwise wavenumber.

Differences between the smooth wall spectral densities and liner spectral densities are clearly visible. Unlike the broadband nature of the smooth wall streamwise spectral density, the streamwise spectral densities for the liner show a tonal concentration of energy at wavelengths close to the orifice spacing (dashed black). These wavelengths near the orifice spacing contain a significant proportion of the energy and the near wall peak at $y^+ \approx 10-30$ is lower than for the smooth wall. This is consistent with the disruption of the near-wall cycle observed in the instantaneous velocity field in Fig. 6.2. A similar trend is observed for the pressure fluctuations. Pressure fluctuations are significantly enhanced downstream of the point of transition. This was easily observed in contours of the pressure fluctuations in an $x-y$ plane, shown in Fig. 6.3 ***(b)*** and can also be seen in the spectral densities. The wavelength of the maximum pressure fluctuations shifts closer to the orifice spacing. Furthermore, whereas the energy in the pressure fluctuations over the smooth wall is concentrated away from the wall, energy in pressure fluctuations resides primarily near the wall for the case of the acoustic liner. Figure 6.3 shows how high-pressure fluctuations exist near the wall, towards the downstream edge of the orifices. The trend of the wall-normal velocity fluctuations, while similar to the streamwise velocity and pressure, have more energy concentrated at wavelengths smaller than the orifice spacing. Most of the energy is concentrated at wavelengths more comparable to the orifice diameter.

The influence of the smooth-liner transition can also be seen in the spectral densities. The influence of the rough wall appears to extend into the outer layer of the turbulent flow. The streamwise velocity spectra immediately after the transition point bears similarity to the spectra further downstream, albeit with less energy in the outer layer and a higher tonal concentration of energy near the orifice wavelength spacing, hinting at the very high fluctuations near the wall exhibited by the flow immediately after encountering the rough wall, as shown in figure 6.3 and 6.2. The wall-normal velocity spectra, on the other hand, is more distinct from the smooth wall region and also further downstream of the transition point. The outer layer, compared to both the smooth wall and further downstream of the transition point, differs and contains a significantly smaller proportion of the energy.

The spectral densities have important differences and similarities with the channel flow simulations, where we reported an influence of acoustic liners on the inner-outer scale interaction in the turbulent flow. We noted that the footprint of the larger structures on the smaller scales closer to the wall increased. There is no clear evidence of any such behaviour in the current results. The difference could be due to the small domain size used

in the channel flow simulations, which arguably has some effect on the dynamic of the large scale structures.

6.3 Flow with acoustic forcing

Figure 6.11 **(*a*)-(*f*)** shows the instantaneous flow over an acoustic liner that is subjected to incoming acoustic waves. The acoustic waves have maximum intensity at the outflow and they are progressively damped, at least in the liner vicinity, as they travel upstream. The action of the selective frequency damping is also visible starting at $(x-x_t)/\delta_0 \approx 10$, quenching the acoustic waves on the smooth wall, before they reach the recycling station used to generate the inflow turbulent fluctuations. In addition to the fluctuations inside the orifice and cavity that result from the turbulent boundary layer, the acoustic wave leads to pressure fluctuations inside the cavity, particularly evident in the cavities closest to the outflow where the acoustic waves are introduced. Further upstream, however, the flow below the surface of the facesheet, in particular, and the boundary layer, in general, appears to be relatively unaffected by the grazing sound wave, evidenced by the wall-normal velocity fluctuations shown in Fig. 6.11 **(*c*)** bearing similarity to the turbulent grazing flow without sound waves. In a very similar fashion to flow in the absence of acoustic waves, and our channel flow results, an asymmetric distribution of the flow inside the orifice is observed with high wall-normal velocity fluctuations primarily at the downstream edge of the orifice, superimposed on top of the vortex that resides within the orifice due to the grazing turbulent flow, possibly hinting at a more subdued reaction to the acoustic waves as compared to the turbulent grazing flow.

Zhang and Bodony [7] showed how the asymmetric flow inside the orifice becomes more symmetric due to the action of acoustic waves, and noted a significant influence of the acoustic liner on the drag if the acoustic fluctuations were higher than or of a comparable magnitude as the turbulent fluctuations, i.e at high SPL. Figure 6.11 **(*g*)** shows the SPL of the pressure fluctuations at the cavity bottom as a function of the frequency at two different streamwise locations: the middle of the first cavity upstream of the outflow at $(x-x_t)/\delta_0 = 69.75$ and further upstream at $(x-x_t)/\delta_0 = 67.25$. The cavity closest to the outflow, where we introduce a $150dB$ acoustic wave, experiences high-pressure fluctuations at the frequency corresponding to the resonance frequency and its harmonics. However, fluctuations at these frequencies decrease rapidly in the upstream direction. Already cavities only slightly upstream, have significantly decreased energy contained in this frequency band. Slightly further upstream, the tonal component of the pressure fluctuations is indistinguishable from the broadband the turbulent fluctuations. The rapid decrease in acoustic fluctuations in the cavity, and by extension, in the region near the wall, is primarily due to the acoustic liners. The frequency of the acoustic wave is tuned to the acoustic liner resonance frequency and there is significant dissipation of energy in the region close to the wall. Acoustic liners further upstream do not experience the high acoustic fluctuations.

As a result, the aerodynamic performance of acoustic liners appears to be largely independent of the acoustic forcing. Figure 6.12 shows the streamwise velocity and the Hama roughness function in the domain for the case with acoustic forcing. We note that the ΔU^+ is almost the same as in the absence of acoustic waves (dashed line). This is in line with what was observed in experiments of acoustic liners in the GFIT by Howerton

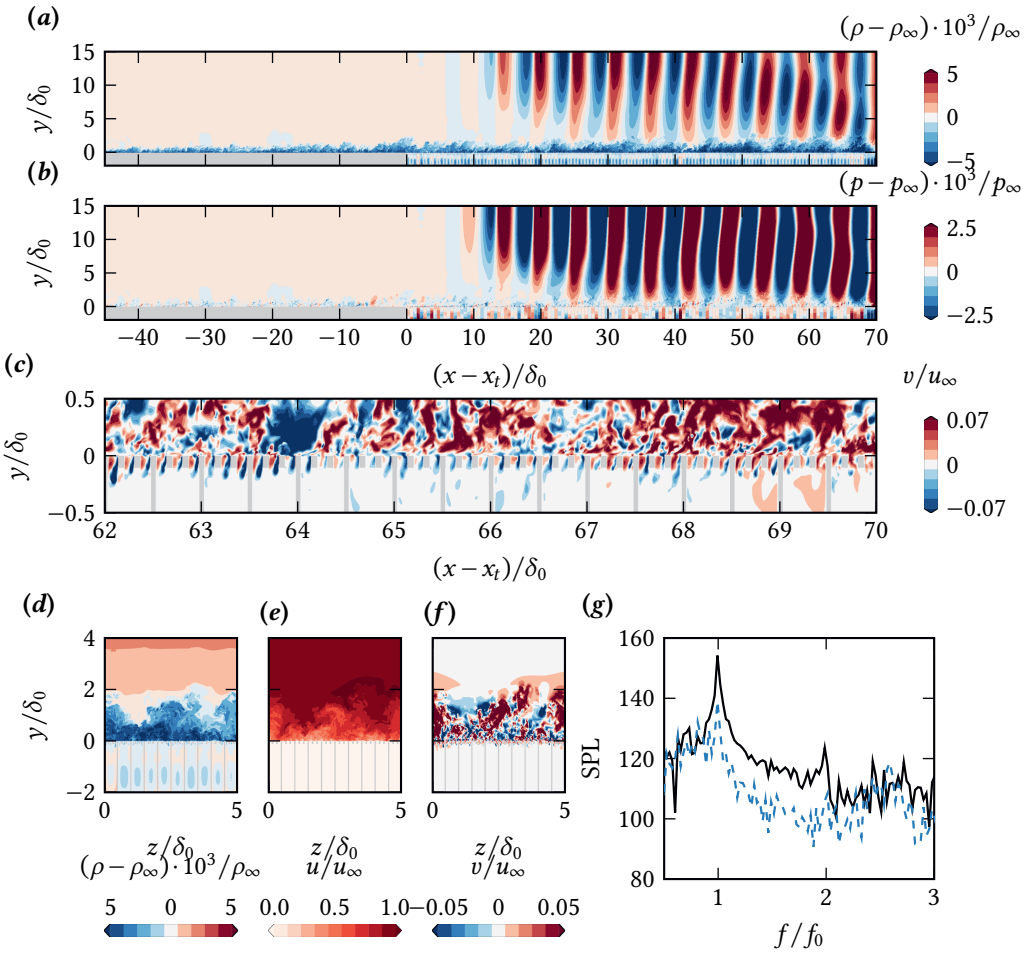

Figure 6.11: Instantaneous density (*a*), pressure (*b*) and wall-normal velocity (*c*) fields in a longitudinal plane and instantaneous density (*d*), streamwise velocity (*e*) and wall-normal (*f*) velocity in a cross-stream plane for acoustic liners interacting with grazing flow and acoustic forcing. The sound pressure level at the bottom of a cavity as a function of the frequency is shown in (*g*), where the solid line is for the first cavity upstream from the outflow at $(x-x_t)/\delta_0 = 69.75$ and the dashed line is for a cavity slightly further upstream at $(x-x_t)/\delta_0 = 67.25$.

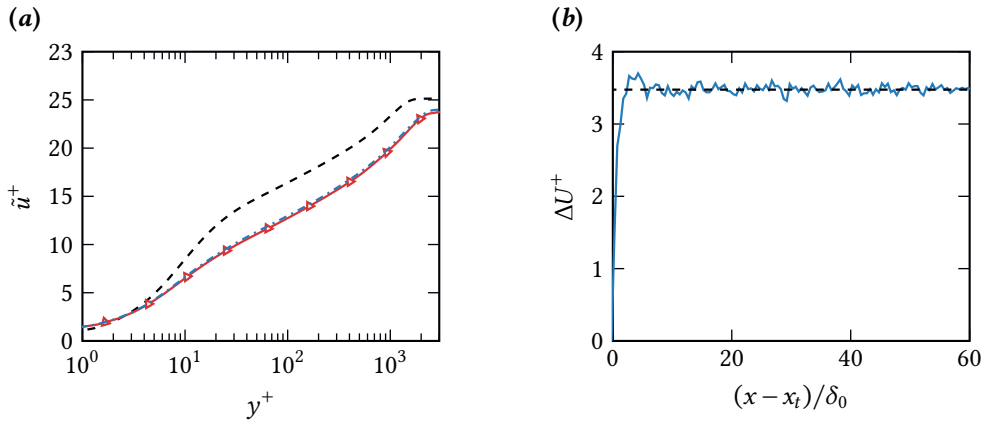

Figure 6.12: Mean streamwise velocity (a) for case L_2 as a function of the wall-normal coordinate. Different line types represent different streamwise locations in panel (a): triangles ($(x - x_t)/\delta_0 \approx 45$) and dashed line ($(x - x_t)/\delta_0 \approx -5$). ΔU^+ as a function of the distance from the transition point (b) for case L_2. The dash-dotted line in (a) shows the streamwise velocity for case L_1 at the same streamwise location. The dashed line in (b) shows the average ΔU^+ in the absence of acoustic waves.

and Jones [11], who observed no change in drag due to acoustic fluctuations. In contrast, Zhang and Bodony [7] saw a marked increase in drag as the SPL of the acoustic waves was increased in their simulations. Differences with Zhang and Bodony [7] can be explained by the manner in which the acoustic wave was introduced. Whereas we introduce a grazing acoustic wave and the region near the wall dissipates the acoustic fluctuations, Zhang and Bodony [7] introduced acoustic fluctuations from the top freestream boundary and the liners were constantly subjected to high SPL acoustic fluctuations.

6.4 Conclusion

We performed unprecedented Direct Numerical Simulation (DNS) of a turbulent boundary layer over a permeable surface that closely resembles acoustic liners that are used on the inside of aircraft engines for noise attenuation. Our work represents the first ever fully resolved DNS of a turbulent acoustic liner flow. In a broader sense, our work adds to the body of literature on turbulent flows interacting with permeable surfaces. Our boundary layer simulation confirm the main findings of our channel flow simulations with fully resolved acoustic liner geometries: acoustic liners lead to an increase in drag as compared to the smooth wall and the added drag scales very well with the inverse of the Forchheimer permeability coefficient. Our simulation, therefore, provides supporting evidence for acoustic liners behaving as a permeable substrate and evidence of a fully rough regime for such permeable surfaces, in similar fashion to canonical rough wall turbulent boundary layers.

However, we also find important differences with canonical rough surfaces, particularly, in the return to equilibrium conditions after a smooth-to-liner transition. The internal boundary layer grows at a much higher rate as compared to canonical rough surfaces,

possibly because the latter generally protrude into the flow, leading to a slower recovery. From a practical perspective, this means that one can neglect the spatial adjustment region in the estimation of the aerodynamic drag for acoustic liners. The Reynolds stresses, on the other hand, recover at approximately the same rate as known for canonical rough surfaces.

Grazing acoustic waves were observed to not influence the aerodynamic performance of the acoustic liner. This agrees with the results reported by Howerton and Jones [11] who found the same added drag in flow cases with and without incoming acoustic waves. We believe, however, that this can, at least in part, be chalked down to the manner in which the acoustic wave is introduced. In real operating conditions, acoustic forcing is not necessarily a monochromatic planar grazing wave as we assumed, and the question of the combined influence of turbulent grazing flow and acoustic waves remains, to some extent, unanswered. Another important point is that even if noise was not influencing the aerodynamic performance, this does not imply the inverse. In fact, recent studies confirmed that grazing flow substantially alters the acoustic impedance [126]. In summary, much remains to be done to understand the interplay between acoustics and aerodynamics. Assuming that modeling the engine noise as a monochromatic acoustic wave is a valid assumption, one would need to run several simulations with different frequencies, amplitudes and angles with respect to the liner. Considering that the simulations here presented have about 16 Billion mesh points, developing such dataset remains a visionary task.

7

Broadband Acoustic Liners

The discussion so far has centered around conventional acoustic liner geometries. Conventional acoustic liner geometries consist of solid cavity walls and facesheet perforations. All cavities act independently of each other and due to the locally reacting nature of the liners, they are only effective against tonal sources of noise. Their noise absorption spectrum typically only exhibits several sharp peaks corresponding to their resonance frequency and higher harmonics. As of late, with a combination of the increase in bypass ratio of fans and conventional acoustic liners effectively damping tonal noise, the interest is now towards designing acoustic liners to dampen broadband noise effectively. The following chapter departs from the remainder of the thesis, in that it attempts to provide an initial assessment of the impact of broadband acoustic liner geometries on drag, and also helps qualify our hypothesis of the Forchheimer coefficient as the relevant roughness length scale.

7.1 Broadband acoustic liner geometries

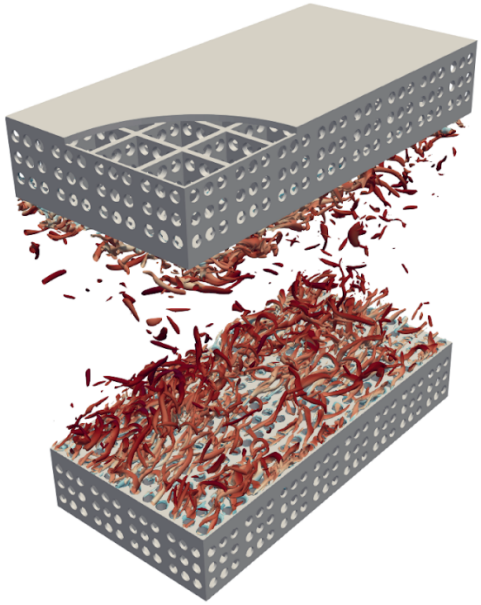

Figure 7.1: Instantaneous flow field over broadband acoustic liner. The instantaneous flow visualisation is for a simulation showing maximum permeability in the streamwise and spanwise direction (for representation purposes only). Vortical structures are visualised using the Q-Criterion, coloured by the streamwise velocity.

Several broadband acoustic liner concepts exist. The simplest form of a broadband acoustic liner array is one that exhibits several resonance frequencies, such as a variable depth or variable porosity liner. Such acoustic liner arrays exhibit several resonance frequency peaks, providing absorption over a greater frequency spectrum, but do not provide broadband noise absorption, because the individual Helmholtz resonators still act independently. More broadband acoustic liners typically depart from the locally reacting nature of acoustic liners. Metal foams, for example, represent highly permeable surfaces, permeable in both the streamwise and spanwise directions, that dissipate noise over a large

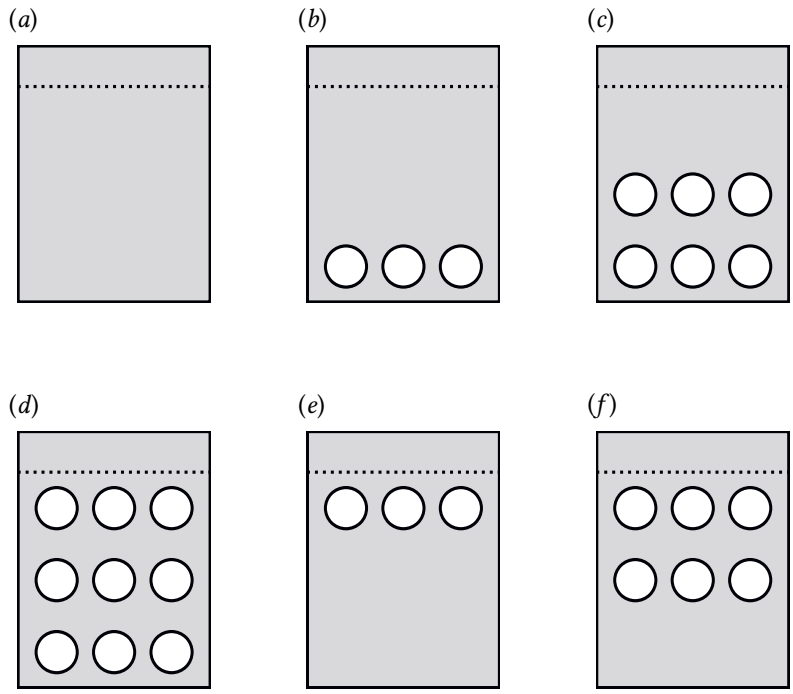

Figure 7.2: Orifice configurations considered. The dashed line indicates the thickness of the facesheet.

bandwidth and without a single discernible resonance frequency [132]. Metal foams have been successfully used around the fan to dissipate noise by as much as 4 dB [133].

Metal foam geometry, however, is difficult to replicate, particularly from a numerical perspective. On the other hand, small modifications to conventional acoustic liner geometries can also be made to bring about a more broadband dissipative nature, in a similar fashion to metal foams. As an example, by simply perforating the cavity walls that separate the individual resonators (see figure 7.1), dissipation over a much wider frequency range can be obtained [10,11]. These concepts typically depart from the concept of a locally reacting liner, and like metal foams, introduce permeability in the streamwise and spanwise direction. Such acoustic liners provide broadband noise absorption at the cost of slightly lower tonal noise absorption as compared to their locally reacting acoustic liner counterparts.

Albeit useful from a noise absorption perspective, such broadband acoustic liners may be detrimental from an aerodynamic perspective. Chapter 4 showed how only the wall-normal permeability is the defining characteristic of acoustic liners, with the non-linear Forchheimer coefficient in the wall-normal direction sufficient to define the aerodynamic behaviour. However, such a simplistic view of acoustic liner geometries may not necessarily carry over to more complex ones that exhibit both streamwise and spanwise permeability in addition to wall-normal permeability. Kuwata and Suga [37] studied permeable surfaces

and progressively relaxed the wall-normal, streamwise and spanwise permeability, noting that while relaxing only the wall-normal permeability had a very minor influence on the flow, relaxing the streamwise or spanwise permeability had a much more profound influence on the flow. Experimental investigations, such as the those of Manes et al. [41] have also shown a degradation of aerodynamic performance with increasing permeability. Evidence suggests, therefore, that broadband acoustic liners would behave in a similar manner and would lead to substantially different flow physics as compared to baseline tonal acoustic liners.

The following sections investigate the influence of successively relaxing the streamwise and spanwise permeability on the aerodynamic performance of acoustic liners, and investigate the extent of the validity of our hypothesis of the wall-normal Forchheimer coefficient as the defining parameter for acoustic liner aerodynamic behaviour. We begin by defining the geometries under investigation and the cases studied, followed by a comparison with conventional acoustic liner geometries.

7.2 Methodology

7.2.1 Test Setup

We solve the compressible Navier–Stokes equations for a calorically perfect gas using the solver STREAmS [70, 114] in a plane channel flow configuration. The computational domain is a rectangular box of size $L_x \times L_y \times L_z = 3\delta \times 2(\delta + h) \times 1.5\delta$, similar to other channel flow simulations. We carry out all simulations at bulk Mach number $M_b = u_b/c_w = 0.3$. The upper and lower walls of the channel are covered by an array of 8×4 acoustic liner cavities, as illustrated in Fig. 7.1. Each cavity has a square cross-section with a side length $\lambda_c = 0.335\delta$ and depth $h = 0.5\delta$. The cavity walls have a thickness of 0.02δ. We use uniform mesh spacing in the streamwise and spanwise directions. In the wall-normal direction, the mesh is clustered towards the wall and coarsened towards the backplate and the channel centre. A minimum of 26 mesh points are used to resolve the orifice diameter. This resolution is well within the viscous spacing typically accepted in DNS, as shown in section 3.5.3.

We wish to study the influence of streamwise and spanwise permeability on conventional acoustic liner geometries and compare it to the baseline configuration with only wall-normal permeability. For the baseline reference case, see Fig. 7.2 (*a*) we consider the geometries studied in chapter 4, more specifically the case with porosity $\sigma = 0.322$, $t/d = 1$ and $d = 0.08\delta$. The three friction Reynolds numbers considered are $Re_\tau = 500$, 1000 and 2000, corresponding to baseline cases *L*-L_{32}, *L*-M_{32} and *L*-H_{32} (see chapter 4 for details). We chose the baseline liner geometry to be representative of acoustic liners in operating conditions, while also keeping a reasonable computational cost to perform a parametric study using DNS. The orifice size and facesheet thickness are in the range found on engine-mounted acoustic liners when scaled with the local boundary layer thickness in landing conditions, as discussed in chapter 2.

To compare the result of liner simulations with the smooth wall data, we take into account the effect of the virtual origin ℓ_T, namely, the distance below the plate at which the flow perceives the equivalent smooth wall, see figure 4.7. All simulations are advanced forward in time until they reach a statistically stationary state, after which statistics are collected for at least $T_{\mathrm{av}} u_\tau/\delta \approx 16$, where T_{av} is the averaging interval.

	Re_b	Re_τ	d^+	σ	σ_{st}	σ_{sp}	Top/Bot	ΔU^+	Δx^+	Δy^+_{min}	Δz^+	N_x	N_y	N_z
S-L	9268	506.1	0	0	0	0	-	-	5.1	0.80	5.1	300	350	150
S-M	21180	1048	0	0	0	0	-	-	5.2	0.80	5.2	600	600	300
S-H	45240	2060	0	0	0	0	-	-	5.2	0.80	5.2	1200	800	600
L-L_{32}	8264	505.3	40.4	0.322	0	0	-	1.90	1.0	0.81	1.0	1500	500	750
L-M_{32}	17810	1026	82.1	0.322	0	0	-	2.78	2.1	0.82	2.1	1500	800	750
L-H_{32}	35470	2044	164.0	0.322	0	0	-	4.44	4.1	0.82	4.1	1500	1400	750
St_{A-9}-L_{32}	6624	499.2	39.9	0.322	0.322	0	-	5.30	1.5	0.80	1.5	1000	500	500
St_{T-3}-L_{32}	7241	491.1	39.3	0.322	0.107	0	T	3.65	1.5	0.79	1.5	1000	500	500
St_{B-3}-L_{32}	7521	494.5	39.6	0.322	0.107	0	B	3.23	1.5	0.79	1.5	1000	500	500
St_{T-6}-L_{32}	6593	482.3	38.6	0.322	0.214	0	T	4.73	1.5	0.77	1.5	1000	500	500
St_{B-6}-L_{32}	6777	488.8	39.1	0.322	0.214	0	B	4.64	1.5	0.78	1.5	1000	500	500
Sp_{A-9}-L_{32}				0.322	0	0.322	-	3.10				1000	500	500
St_{A-9}-M_{32}	15050	1045	83.6	0.322	0.322	0	-	6.21	3.1	0.84	3.1	1000	800	500
St_{T-3}-M_{32}	16730	1000	80.0	0.322	0.107	0	T	3.18	3.0	0.80	3.0	1000	800	500
St_{B-3}-M_{32}	17400	1025	82.0	0.322	0.107	0	B	2.94	3.1	0.82	3.1	1000	800	500
St_{T-6}-M_{32}	15720	995	79.6	0.322	0.214	0	T	4.22	3.0	0.80	3.0	1000	800	500
St_{B-6}-M_{32}	16050	971	77.7	0.322	0.214	0	B	3.82	2.9	0.78	2.9	1000	800	500
St_{A-9}-H_{32}	27860	1987	159.0	0.322	0.322	0	-	8.11	6.0	0.79	6.0	1000	1400	500
St_{T-3}-H_{32}	35060	2021	161.7	0.322	0.107	0	T	4.45	6.1	0.81	6.1	1000	1400	500
St_{B-3}-H_{32}	35060	2032	162.6	0.322	0.107	0	B	4.43	6.1	0.81	6.1	1000	1400	500
St_{T-6}-H_{32}	32880	2087	166.9	0.322	0.214	0	T	6.13	6.3	0.83	6.3	1000	1400	500
St_{B-6}-H_{32}	32880	1991	159.2	0.322	0.214	0	B	5.57	6.0	0.80	6.0	1000	1400	500

Table 7.1: DNS dataset comprising smooth (S-Re), baseline liner L-$Re_{\sigma(\%)}$ and streamwise/spanwise permeable $St_{\chi-N}$-$Sp_{\chi-N}$-$Re_{\sigma(\%)}$ cases where $Re = \{L, M, H\}$ correspond to the three Reynolds numbers $Re \approx 500$ (Low), $Re \approx 1000$ (Medium), and $Re \approx 2000$ (High) and σ is the porosity of the liner case. K_y and α_y are the Darcy and Forchheimer wall-normal permeabilities. ΔU^+ is the Hama roughness function measured at $y^+ + \ell_T^+ = 100$, where ℓ_T is the virtual origin shift. Simulations are performed in a computational box with dimensions $L_x \times L_y \times L_z = 3\delta \times 2(\delta + h) \times 1.5\delta$. Δx^+ and Δz^+ are the viscous-scaled mesh spacing in the streamwise and spanwise direction, and Δy^+_{min} is the minimum mesh spacing in the wall-normal direction. $T_{\text{av}} u_\tau / \delta$ is the time averaging interval. Top/Bot, indicates the configuration of the holes and whether they are closer to the top facesheet (T) or closer to the bottomplate (B), see figure 7.2.

7.2.2 Broadband Acoustic Liner Configurations

The baseline acoustic liner configurations exhibit rigid cavity walls (figure 7.2 (*a*)). The standard liner configuration is then increasingly perforated in the streamwise or spanwise direction to relax the permeability tensor, while making sure that the resulting geometry is as close as possible to the baseline case for the purposes of comparison. The facesheet thickness and the cavity dimensions remain unchanged for all cases considered. We perforate the cavity walls such that the streamwise or spanwise facing walls, have a porosity of $\sigma_{st/sp} = 0.322$, where σ_{st} and σ_{sp} are the porosities of the streamwise and spanwise facing walls respectively. This results in an array of equally distributed 9×9 perforations for each cavity wall, see figure 7.2 (*d*). The array of 9×9 perforations for the cavity walls represents our most porous cases. The porous cavity walls, irrespective of whether they are porous in the streamwwise or spanwise direction, are then modified by:

- Maintaining the geometric configurations of the 9×9 perforation array but progressively closing off the top row or the top two rows, such that only the bottom row or the bottom two rows remain open. See figure 7.2 (*b*) and (*c*).
- Maintaining the geometric configurations of the 9×9 perforation array but progressively closing off the bottom row or the bottom two rows, such that only the top row or the top two rows remain open. See figure 7.2 (*e*) and (*f*).

The geometries considered are shown in figure 7.2, and details of all flow cases are reported in Table 7.1. The influence of the streamwise permeability is primarily considered, with the exception of case Sp_{A-9}-L_{32}, which exhibits spanwise permeability. The naming of the flow cases for the baseline cases is as in chapter 4. Streamwise and spanwise permeable flow cases are named either $St_{\chi-N}$-$Re_{\sigma(\%)}$ or $Sp_{\chi-N}$-$Re_{\sigma(\%)}$, where St and Sp are the cases with streamwise and spanwise permeability, $\chi = A$, T or B for cases with the full 9×9 cavity perforations, cavity perforations towards the top (close to the facesheet) or cavity perforations towards the bottom of the cavity (away from the facesheet), and N is the number of cavity perforations in the St or Sp directions. This is followed by the Reynolds number, low (L) for $Re_\tau \approx 500$, medium (M) for $Re_\tau \approx 1000$ and high (H) for $Re_\tau \approx 2000$.

7.3 Flow over Broadband Acoustic Liners

7.3.1 Instantaneous Flow

We previously showed how acoustic liners influence the instantaneous flow over them. High-intensity wall-normal fluctuations alter the near-wall flow and a periodic pattern emerges, due to the imprint of the orifices, particularly visible in the wall-normal fluctuations (see chapter 4). With knowledge of how a conventional acoustic liner influences the flow, we begin our analysis of broadband acoustic liner geometries by investigating how such modified acoustic liners alter the instantaneous flow over them. Figure 7.3 shows the streamwise velocity of a wall-parallel plane for the cases at $Re_\tau = 2000$. The addition of streamwise permeability may completely alter the instantaneous flow, depending upon the porosity of the streamwise-facing walls. For case St_{A-9}-H_{32}, which exhibits the highest streamwise permeability, there is a very clear spanwise organisation of the instantaneous flow, resembling Kelvin-Helmholtz-like structures. This clear spanwise organisation of

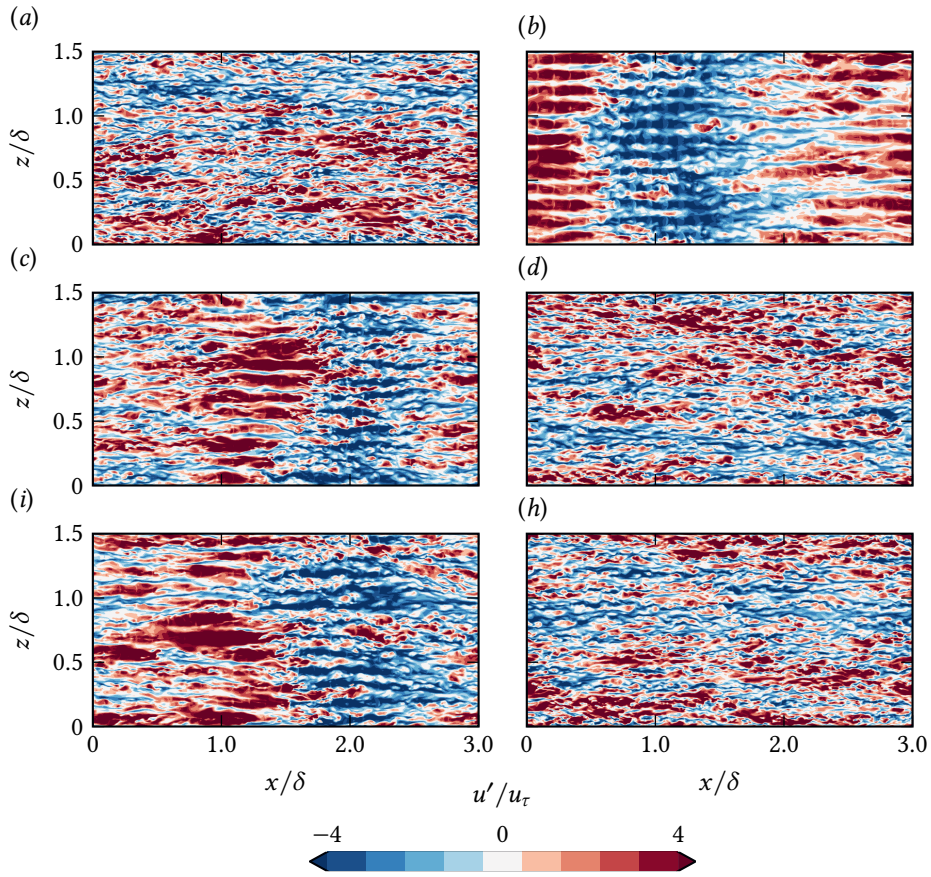

Figure 7.3: Instantaneous streamwise velocity fluctuations in a wall-parallell plane at $y^+ \approx 10$ for flow cases L-L_{32} (*a*), St_{A-9}-H_{32} (*b*), St_{T-6}-H_{32} (*c*), St_{T-3}-H_{32} (*d*), St_{B-6}-H_{32} (*e*), St_{B-3}-H_{32} (*f*).

these structures that we see for case St_{A-9}-H_{32} is weaker for cases St_{B-6}-H_{32} and St_{T-6}-H_{32}, and appears to disappear completely for cases St_{B-3}-H_{32} and St_{T-3}-H_{32}, indicating a clear correlation between the permeability of the streamwise-facing walls and the occurrence of these rollers.

Our observations are in line with the work of Kuwata and Suga [37], who report the appearance of Kelvin-Helmholtz-like structures as the permeability is increased. Our work is also in line with prior work on acoustic liners of Scalo et al. [50], who used an impedance boundary condition to model acoustic liners, and noted that particular cases brought about Kelvin-Helmholtz like structures. Scalo et al. [50] noted that acoustic liner flow cases that showed evidence of large-scale spanwise structures also corresponded to the cases that exhibited the highest added drag, due to the intense mixing that was associated with them.

Figure 7.4 shows the instantaneous wall-normal velocity for the baseline case and case

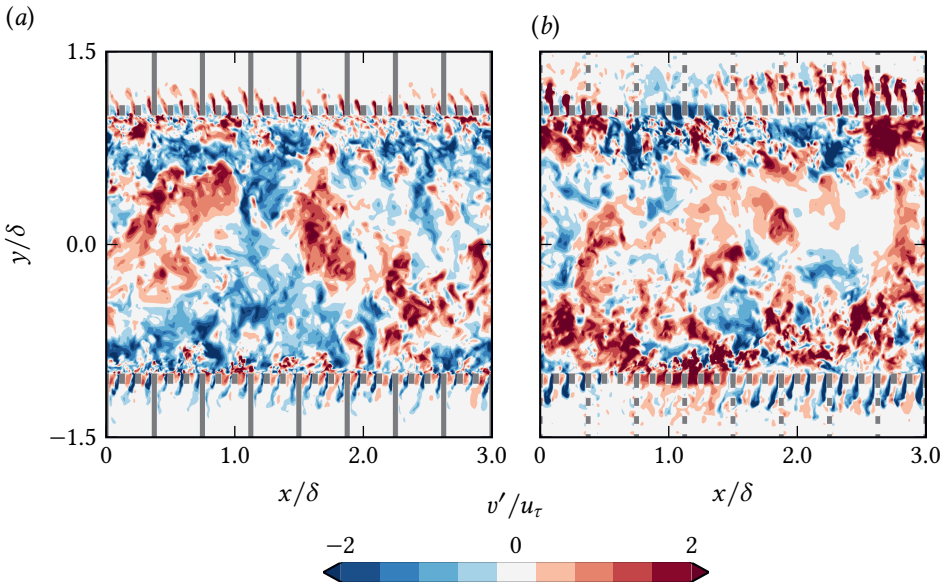

Figure 7.4: Instantaneous wall-normal velocity fluctuations in an $x-y$ for flow cases L-L_{32} (a) abd St_{A-9}-H_{32} (b).

St_{A-9}-H_{32}. The jet-like flow that was observed for the baseline cases in chapter 4, is further amplified in the case of a permeable streamwise facing wall, due to the less restrictive nature of the cavity underneath the facesheet. Figure 7.4 also shows how flow from one cavity may spill over into the other cavity. The permeable cavity walls allow "communication" of the flow below the surface of the facesheet over larger streamwise wavelengths. The impermeable acoustic liner cavities restrict coherent flow structures below the wall that are larger than their cavity length. By removing this restriction, permeable acoustic liners provide the necessary conditions that can bring about Kelvin-Helmholtz like structures. The more permeable the wall, the easier the communication and the higher the likelihood of Kelvin-Helmholtz-like structures, along with an increase in the intensity of the jet-like flow into the cavities which was directly correlated with an increase in drag in chapter 4.

7.3.2 Drag increase and the role of permeability

We continue our analysis by looking at the statistics of the flow. After accounting for the virtual origin, as in the remainder of the thesis, the mean streamwise velocity for the cases considered is shown in Figure 7.5. Irrespective of the case considered, we see an increase in drag, quantified with the aid of the ΔU^+, i.e. the downward shift of the mean streamwise velocity profile with respect to the smooth wall in the log layer. More recently, several investigations with modelled boundary conditions have highlighted how permeable surfaces can be exploited to reduce drag [134, 36]. For the cases considered, however, any additional permeability added to the surface tends only to increase drag, and in the case of permeable cavity walls, the increase in drag is always higher than for the conventional

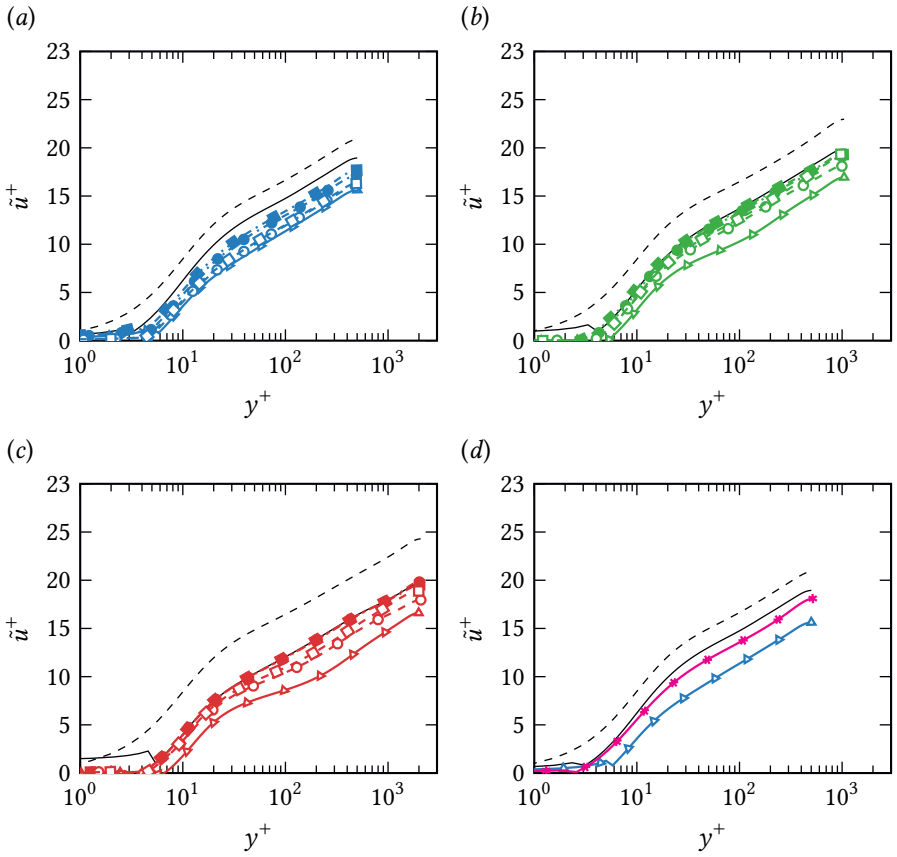

Figure 7.5: Mean wall-normal velocity for the smooth wall cases (dashed line), baseline liner cases (solid line without symbols), cases St_{A-9} (empty triangles), cases St_{T-6} (empty circles), cases St_{B-6} (empty squares), cases St_{T-3} (filled circles), cases St_{B-3} (filled squares) and case Sp_{A-9}-L_{32} (stars), at friction Reynolds numbers $Re_\tau = 500$ (*a*) and (*d*), 1000 (*b*) and 2000 (*c*).

baseline liner; i.e. any additional relaxation of permeability, irrespective of the direction, increases drag.

The cases with the highest streamwise permeability also call into question the validity of the outer-layer similarity hypothesis. Figure 7.5 (*c*) shows that the velocity profile for case St_{A-9}-H_{32} is not parallel to the smooth wall streamwise velocity profile and also the baseline acoustic liner, that exhibits outer layer similarity for the velocity profile, streamwise velocity profile in the log layer. Some evidence of the change in the gradient of the log layer is also visible for case St_{A-9}-L_{32} in figure 7.6, that shows the slope of the mean velocity profile for cases *S*-*H*, *L*-H_{32} and St_{A-9}-H_{32} and the Reynolds stress for cases *S*-*H* and St_{A-9}-H_{32}. Differences in the Reynolds stress in the outer layer were already seen for conventional acoustic liner geometries in our channel flow simulations. The breakdown of the outer layer similarity hypothesis for the streamwise velocity in the presence of

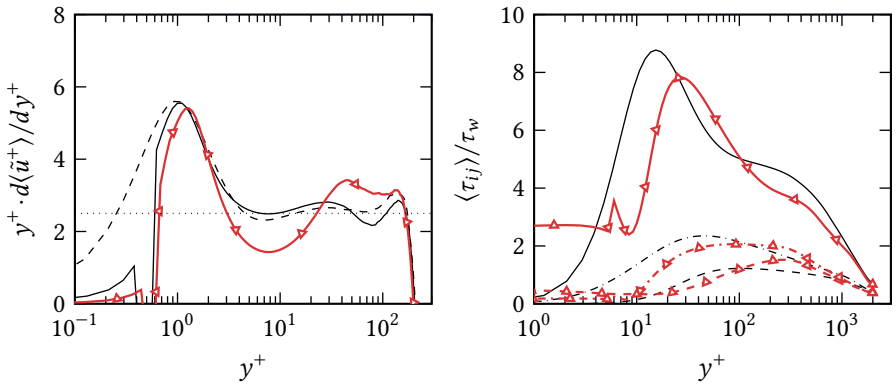

Figure 7.6: Wall-normal gradient of the streamwise velocity (*a*) and Reynolds stresses (*b*) as a function of the viscous-scaled wall-normal location. Symbols and lines are as in figure 7.5.

permeability, however, is a significant departure from how conventional acoustic liners behave. This is more in line with the work of Breugem et al. [39] and Kuwata and Suga [101], who reported different values of κ over permeable surfaces. Nevertheless, it can not be ruled out that the change in κ for our current simulation is an artefact of the small domain size considered, and the change in κ in the work of Breugem et al. [39] and Kuwata and Suga [101] is an artifact of the low Reynolds numbers considered in their studies

7

Albeit strictly only valid for cases that exhibit outer layer similarity, we nevertheless quantify the added drag of our streamwise permeable cases using ΔU^+, in a similar manner to our previous cases, by measuring it at $y^+ \approx 100$. Figure 7.7 shows the results of our streamwise permeability simulations superimposed on top of our channel flow results for the conventional acoustic liners. It is clear that the wall-normal Forchheimer coefficient is not sufficient to capture the aerodynamic influence of all geometries. Introducing permeability in other directions increases the ΔU^+. However, with increasing Reynolds number, the aerodynamic penalty gradually approaches the case of an acoustic liner with purely wall-normal permeability. Cases St_{T-3}-H_{32} and St_{B-3}-H_{32} exhibit almost the same aerodynamic penalty as case L-H_{32} and the ΔU^+ approaches the curve $k_s^+ = 1/\alpha_y^+$. The evidence suggests, a possible correlation of the effective sandgrain roughness length scale with the permeability of the form:

$$k_s^+ = \frac{C_1}{\alpha_y^+} + \frac{C_2}{Re}\frac{f(P_x)}{f(P_y)}, \tag{7.1}$$

where C_1 and C_2 are some constants and $f(P_x)$ and $f(P_y)$ are functions of the permeability of the medium in the streamwise and wall-normal direction respectively, which can be a combination of the linear Darcy and the non-linear Forchheimer permeability in their respective directions. The inverse Reynolds correlation suggests that as the Reynolds number is increased, the influence of the streamwise permeability decreases and the wall-normal Forchheimer coefficient becomes increasingly more important.

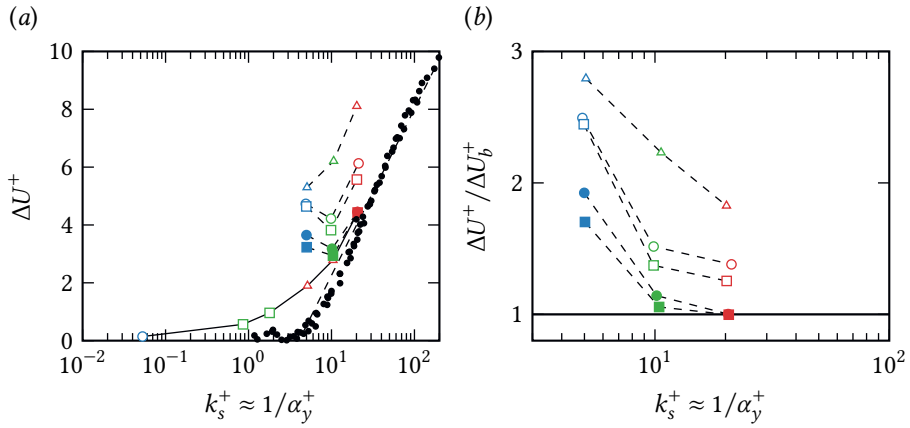

Figure 7.7: ΔU^+ (*a*) and the ratio of the ΔU^+ and the baseline ΔU^+ (*b*) as a function of the inverse of the wall-normal Forchheimer coefficient. Dashed lines with symbols show streamwise permeable cases and are as in figure 7.5.

What is interesting to note is that it is not solely the permeability that influences the added drag but rather the distribution of permeability also influences the behaviour. The averaged permeability, itself, is independent of the distribution of the orifices, and by extension, cases St_{T-3}-L_{32} and St_{B-3}-L_{32} and St_{T-6}-L_{32} and St_{B-6}-L_{32} exhibit equal permeability in the streamwise direction. However, cases St_{T-3}-L_{32} and St_{T-6}-L_{32} exhibit a higher drag increase than cases St_{B-3}-L_{32} and St_{B-6}-L_{32}. As the flow below the facesheet surface is driven by the flow in the core of the channel, perforations closer to the surface will have a much larger influence than perforations away from the facesheet surface. In that regard, $f(P_x)$ and $f(P_y)$ are not simply functions of the absolute values of the permeability, but rather a complex function that not only takes into account the entire permeability tensor but also the geometrical distribution of the permeability. In essence, what matters is not the global permeability tensor, but the local permeability in regions of high shear.

The drag increase is much lower for the same permeability of the spanwise facing walls, compared to the streamwise facing walls, as shown in figure 7.5 (*d*). The marginal increase in drag could be down to the increase in the jet-like flow into the cavity due to the relaxed permeability. However, the rigid streamwise facing walls prevent, as shown in the following section, the development of the spanwise invariant structures, and consequently, the drag increase is much lower.

7.3.3 Spectral Densities

To gain further insight into the organisation of turbulence, we continue our analysis with the spectral analysis of the turbulent flow. Figures 7.8 shows the pre-multiplied spectral densities of the wall-normal velocity of a subset of the cases considered at $Re_\tau = 500$. The spectrograms show important similarities and differences with the baseline configurations. While the concentration of energy at the orifice spacing exists, cases St_{A-9}-L_{32} and St_{T-6}-L_{32} show a large concentration of energy at wavelengths of the order $\lambda_x \geq \mathcal{O}\delta$, in the

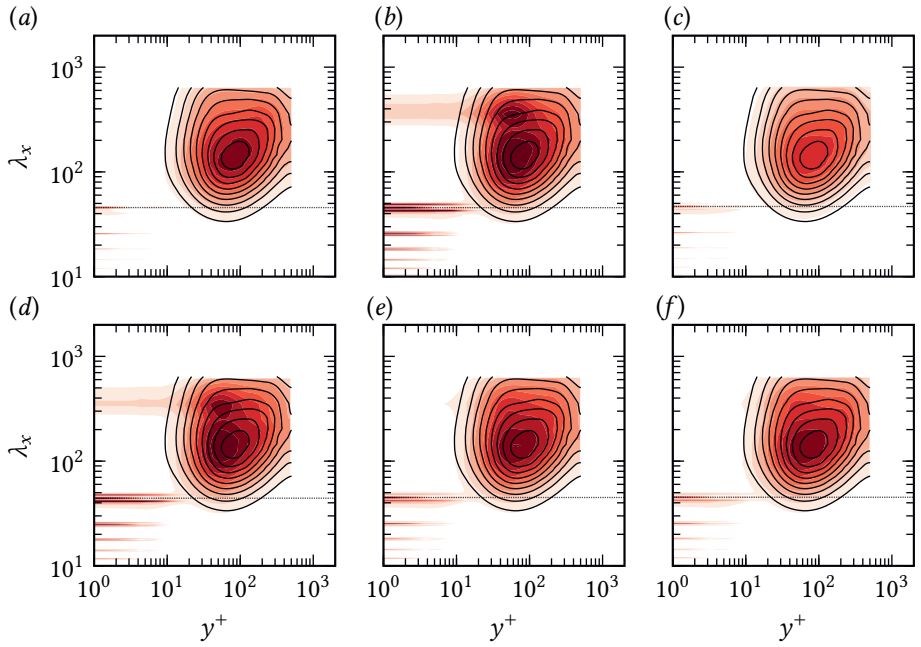

Figure 7.8: Premultiplied wall-normal velocity spectra in the streamwise direction as a function of the viscous-scaled wall-normal location for cases L-L_{32} (*a*), St_{A-9}-L_{32} (*b*), Sp_{A-9}-L_{32} (*c*), St_{T-6}-L_{32} (*d*), St_{T-3}-L_{32} (*e*) and St_{B-3}-L_{32} (*f*).

wall-normal velocity spectra (see figure 7.8 (*b*) and (*d*)), indicating the presence of the Kelvin-Helmholtz-like structures in the flow. The strength of the Kelvin-Helmholtz like rollers decreases for case St_{T-3}-L_{32}, correlating very well with the trends observed for the drag increase. No evidence of streamwise rollers is present for case Sp_{A-9}-L_{32} (see figure 7.8 (*c*)), i.e the case with only wall-normal and spanwise permeability, indicating the need for an extended region of communication above and below the facesheet surface as a necessary prerequisite for the appearance of such structures, and lending further evidence to our hypothesis that these spanwise-oriented structures are one of the reasons for the massive drag increase we see for our cases with streamwise permeability.

7.4 Conclusion

We investigated the drag penalty associated with relaxing the permeability tensor in acoustic liner geometries. Conventional acoustic liners are only permeable in the wall-normal direction, and their behavior has been extensively elaborated upon in the previous chapters. Modern aircraft require broadband noise attenuation, and many broadband acoustic liner concepts exhibit permeability in the streamwise and/or spanwise directions. Using our conventional acoustic liner geometry as a reference, we progressively relaxed permeability in the streamwise and spanwise directions and quantified the resulting drag

penalty. On a more fundamental level, our work contributes to the broader understanding of how complex permeable surfaces interact with turbulent flows.

Determining the sensitivity of a permeable surface is to small geometric changes is difficult, and our brief foray into streamwise and spanwise permeable surfaces ultimately raises more questions than it answers. It is almost universally accepted—except in some very specific fringe cases—that increasing permeability in any direction amplifies its influence on turbulent flow, leading to a higher drag penalty. However, prior research has almost exclusively focused on low Reynolds number simulations, which are more tractable and affordable. In contrast, our high Reynolds number simulations across a range of geometries reveal that increased permeability does not always result in a greater drag penalty. Surfaces that are permeable in the streamwise and spanwise directions, in addition to the wall-normal direction, do not necessarily experience higher aerodynamic drag. Instead, drag is influenced by the roughness Reynolds number and the distribution of permeability. The dependence on the Reynolds number itself is counterintuitive. While drag penalty generally increases with Reynolds number—as expected due to an increase in the roughness Reynolds number—our results reveal an unexpected trend: the drag penalty asymptotes towards that of the reference conventional acoustic liner case as Reynolds number increases. In other words, the influence of permeability in the streamwise and spanwise directions diminishes at higher Reynolds numbers, and the lower the streamwise permeability, the faster this regression toward the facesheet-normal permeable case occurs.

At a fixed Reynolds number, permeability distribution plays a significant role. Permeability concentrated near the surface of the facesheet has a greater impact than an equally porous geometry where permeability is concentrated near the backplate. This aligns with our findings in previous chapters, which indicate that the depth of acoustic liners, at least within the parameter space of our simulations, has a negligible effect. The region near the orifice openings in the facesheet experiences high-amplitude turbulent fluctuations, and the jet-like flow observed in conventional acoustic liners has a limited extent in the wall-normal direction. As a result, the bottom of the cavity remains relatively insulated from high-velocity turbulent fluctuations, and perforations in this region contribute less to drag penalty. Conversely, perforations closer to the jet-like flow into the cavities contribute more to drag, highlighting an opportunity for a very simple optimization of broadband acoustic liners while maintaining the drag penalty of conventional designs: perforations in acoustic liners should be placed as far from the surface of the facesheet as possible.

8

Conclusion

Our work represents the first ever DNS of turbulent flows over surfaces that closely resemble the geometry of acoustic liners in aircraft engines in realistic operating conditions, and adds to the limited body of literature on permeable surfaces interacting with turbulent flow. This numerical methodology provided us with unprecedented high-fidelity data, allowing us to address several aspects of the flow physics towards a better understanding of why acoustic liners behave the way they do and why they increase aircraft drag.

On a more fundamental level, our work highlights the similarities and differences between permeable surfaces and canonical rough surfaces. Porous surfaces have been studied considerably less than rough surfaces, and our work constitutes one of the few examples of pore-resolved simulations at high Reynolds numbers. Acoustic liners are, by the strictest definition, not permeable surfaces as the bottomplate is impermeable and restricts flow through it. In general, however, much like other permeable surfaces, the depth of the cavity is such that the turbulent flow does not feel its influence. The flow, therefore, perceives the top facesheet as a permeable surface, in a very similar fashion to a turbulent flow interacting with a perforated plate.

Despite the simplicity of their geometry, the interactions of perforated plates with turbulent grazing flow are not very well understood. A characteristic of canonical rough surfaces is that if scaled with the proper characteristic length scale, the induced drag tends to approach a fully rough regime, where the added drag becomes independent of the Reynolds number. We analysed several possible characteristic length scales for acoustic liner-type perforated plate geometries and the dependence of the added drag on both the viscous-scaled diameter and the porosity pointed towards the importance of the permeability. We analysed the correlation between wall-normal permeability and drag in turbulent flows over perforated plates. Permeability has been identified as an important characteristic of permeable surfaces in general in prior work. However, prior work on permeable surfaces focused on the Darcy permeability and its correlation with the added drag.

Perforated plates are different from other types of permeable surfaces because their porosity does not exceed $\sigma \approx 0.3$ in most engineering applications, as higher values would substantially affect the structural integrity of the plate. Another main difference to other porous surfaces is that the pore Reynolds number can be large, and in many applications, $Re_p \sim \mathcal{O}(10^2)$ or higher. Darcy permeability is only applicable within the regime of Stokes flow and as the pore Reynolds number increases, the applicability of Darcy permeability becomes increasingly more suspect. Our simulations also showed significant inertial effects inside the cavity, with jet-like flow emanating from the downstream end of the orifices. It is because of this inertia-dominated flow inside the orifices, that the Forchheimer permeability, and not the Darcy permeability, is the characteristic length scale for our perforated plate-type surfaces resembling acoustic liners. This aspect is particularly interesting and novel as it means that the Darcy law may not be valid for moderate pore sizes. Darcy-type models have been used extensively to avoid resolving the porous surface geometry, whereas the present findings reveal that this modelling assumption is inaccurate if the viscous-scaled pore size is large, and nonlinear corrections for the pressure drop are needed.

High-pressure fluctuations at the downstream edge of the orifice force high wall-normal velocity fluctuations i.e. normal to the facesheet of the acoustic liner. The high r.m.s wall-normal velocity is immediately noted in the instantaneous flow visualisations, with

high values of the pore Reynolds number based on the wall-normal velocity fluctuations $Re_p = 50–500$. These very high wall-normal velocity fluctuations show an almost perfect correlation with the drag increase which we express in the form of the Hama roughness function ΔU^+.

That is not to say that the Forchheimer permeability perfectly encapsulates the influence of acoustic liners into a single parameter. The fact that changing the thickness leads to a slightly different asymptote for the fully rough regime indicates that there is, in fact, an additional roughness influence of the permeable surface. The influence of roughness on a permeable surface has been observed recently in the work of Esteban et al. [40], who associated the changes in height of the permeable surface as an additional roughness influence. In the case of our perforated plates, changing the thickness acts similarly. However, for a known family of geometries, which in the case of perforated plates means that the thickness-to-diameter ratio is the same, the Forchheimer permeability alone determines the added drag of these geometries. Furthermore, our boundary layer simulation helps confirm the findings of our channel flow simulations with fully resolved acoustic liner geometries: providing supporting evidence for acoustic liners behaving as a permeable substrate and evidence of a fully rough regime for such permeable surfaces.

The determination of the Forchheimer permeability does not require expensive fully resolved simulations. Accurate calculation of the Forchheimer coefficient for perforated plates is still challenging, however, and discrepancies up to 50% are common in the literature, both from numerical and experimental sources. We calculate the Forchheimer coefficient using numerical simulations, and our results are in good agreement with a subset of the available data and engineering correlations. Semi-empirical relations for estimating the Forchheimer coefficient often show a complex dependence on the plate geometry. However, we note that in the limit of small porosity all correlations return the same functional dependence $\alpha_y \sim 1/\sigma^2 t$, which can be used as a first-order approximation. Future efforts should be directed towards an accurate numerical characterization of this length scale, both experimentally and computationally. An error of $\approx 50\%$ in determining the Forchheimer coefficient can lead to almost a 20-30% error in the estimated ΔU^+

From an engineering perspective, the existence of a fully rough regime together with outer layer similarity is good news; together, they form a solid background for wall models and, in principle, we can give up the detailed representation of the surface pattern because the mean velocity profile presents universal features that can be modelled. Moreover, these results tell us that it is possible to use simulations and experiments to estimate the drag variation at higher Reynolds numbers, typical of practical configurations. Our estimate, based on the present DNS, is that a typical acoustic liner produces about 70% higher drag per plane area as compared to a hydraulically smooth wall.

Acoustic liners approaching a fully rough regime is in line with what is usually expected for canonical rough surfaces, indicating possible similarities between canonical rough surfaces and permeable surfaces. However, unlike canonical rough surfaces, we see evidence of a breakdown in outer-layer similarity for the Reynolds stresses. Whereas the rough mean velocity profiles are parallel to the smooth velocity profiles in the outer layer, indicating outer layer similarity holds for the mean velocity profile, there are significant differences observed for the Reynolds stresses in the outer layer. The larger the viscous-scaled permeability, the more pronounced the differences between the smooth and

permeable wall Reynolds stresses, and the differences appear also in the velocity spectra. The velocity spectra for our channel flow simulations of baseline liners even indicated an increase in the footprint of large-scale structures compared to the smooth wall in the region close to the facesheet.

The differences in the Reynolds stress in the outer layer observed in the channel flow simulations may also be traced back to the small box size used for the simulations. In principle, the boundary layer simulation was performed with a box size that was sufficiently large to confirm, without uncertainty, the applicability of outer layer similarity for the Reynolds stresses for acoustic liner-type permeable surfaces. However, in a very similar manner to canonical rough surfaces, the Reynolds stresses adjusted to the smooth-to-rough transition and the new surface conditions slowly at approximately the same rate as canonical rough surfaces, and the height of the IBL based on the streamwise Reynolds stress had not reached the edge of the boundary layer by the end of the domain. The growth of the IBL based on the streamwise velocity, appears to grow much faster for acoustic liner-type permeable surfaces, and the mean streamwise velocity more quickly reacts to the change in surface roughness. This could be because canonical rough surfaces generally tend to protrude into the flow, leading to a more pronounced influence on the flow near the smooth-to-rough transition, necessitating a wall-normal shift of momentum and a larger streamwise region over which the flow adjusts.

Identification of the mechanisms for drag increase helped us propose several novel orifice geometries for acoustic liners, some of which reduce aerodynamic drag without compromising the acoustic performance. Novel orifice geometries had been explored by other authors before but the geometries were more based on trial and error. Our channel flow simulations of standard acoustic liner geometries led us to investigate aerodynamically optimized geometries based on flow physics, which restricted the vast parameter space that one could explore. The aerodynamic performance of the novel geometries was scrutinised based on the DNS of fully resolved acoustic liner arrays in a turbulent channel flow. We find that tapered circular orifices minimized drag compared to a baseline acoustic liner by reducing the apparent porosity at the surface of the facesheet, whereas replacing the circular holes with elliptical slots can lead to a substantially lower drag if the minor axis of the ellipse is sufficiently thin in viscous units. We found that despite the very different configurations tested, all optimised geometries worked by reducing the interaction of the flow above and below the surface of the facesheet, which is confirmed by the reduced wall-normal velocity fluctuations in the proximity of the facesheet.

We also test the acoustic performance of the proposed liner configurations and find that the thin elliptical slots have a substantially reduced acoustic performance compared to a baseline liner; therefore, the improved aerodynamic benefit comes at the cost of lower noise reduction. The tapered hole configuration has slightly better noise attenuation properties than the baseline liner while offering substantially lower aerodynamic drag, and it is therefore superior both from an aerodynamic and acoustic perspective. In addition, tapered holes are easy to manufacture and therefore represent a viable modification to be implemented in existing designs.

Our work is among the very few fully resolved studies on permeable surfaces interacting with turbulent flow, and has helped verify that some permeable surfaces interact with the turbulent flow in a very similar manner to roughness. However, the parameter

space for permeable surfaces is very vast. Even if we restrict our domain to permeable surfaces that are only permeable in the wall-normal direction, such as the perforated plate-type permeable surfaces that we have studied in this work, many variables were not considered. We restricted our domain to geometries that would represent realistic acoustic liner surfaces, where the diameter is less than 10% of the boundary layer thickness. This may not necessarily be true for other perforated plate-type permeable surfaces and pore diameters can be larger. Larger pore diameters would typically lead to the development of a shear layer instability and significantly altered flow dynamics - perhaps even to the extent that the pore diameter and not the permeability is the defining characteristic length scale of the roughness. Furthermore, permeability alone may not define the dynamics of permeable surfaces as permeable surfaces also exhibit an inherent roughness component, inseparable from the permeable component.

We saw that changing the thickness of the acoustic liner shifted the ΔU^+ curve towards a different asymptote. That alone indicates that the non-linear Forchheimer permeability is not the only parameter influencing the flow, and the total influence of a perforated plate-type permeable surface is a combination of its permeability and additional roughness effects and it is not possible to estimate the extent to which the effect of roughness factors in into the permeable surface a priori. For our thick facesheet, we found $k_s^+ \approx 1/\alpha^+$, but in general one could have a proportionality relation $k_s^+ = C/\alpha^+$, similarly to what happens for different roughness geometries.

Our boundary layer simulation helped us verify that many of the assumptions we made to reduce the computational cost of our channel flow simulations, such as reducing the height of the cavity were justified. The influence of the cavity depth is, at least within the range of parameters studied, negligible. That is not to say that the cavity does not influence the flow, however. It is the wall-normal permeability that is the defining characteristic because the streamwise and spanwise permeabilities are zero due to the presence of the cavity walls. In the absence of cavity walls, or equivalently in the presence of perforated cavity walls, the situation changes considerably. Perforated cavity walls (or no cavity walls) introduce streamwise and/or spanwise permeability, which we saw introduce Kelvin-Helmholtz-like instabilities in the flow, a more pronounced effect and a higher drag increase. The streamwise and spanwise permeabilities can compete with the wall-normal one for the role of relevant length scale for the flow. To that extent, even having very large cavities that mimic the influence of having streamwise permeability by allowing flow underneath the perforated plate over distances of the order of magnitude of the boundary layer thickness is also expected to lead to a breakdown of the Forchheimer permeability as the sole determining characteristic of the permeable surface.

Considering the vast parameter space, we also believe, that the existence of a fully rough regime should not be taken for granted for all porous surfaces, as several different geometries fall into this classification, and not all of them might give rise to the same flow physics. In that regard, while we have demonstrated that many aspects of rough surfaces, such as the existence of a fully rough regime and outer layer similarity, may exist for permeable surfaces too, but we have not demonstrated their universality.

References

[1] I. J. Hughes and A. P. Dowling. The absorption of sound by perforated linings. *J. Fluid Mech.*, 218:299, September 1990. doi: 10.1017/S002211209000101X.

[2] A. P. Dowling and I. J. Hughes. Sound absorption by a screen with a regular array of slits. *J. Sound Vib.*, 156(3):387–405, August 1992. doi: 10.1016/0022-460X(92)90735-G.

[3] R. Kirby and A. Cummings. The Impedance of perforated plates subjected to grazing gas flow and backed by porous media. *J. Sound Vib.*, 217(4):619–636, November 1998. doi: 10.1006/jsvi.1998.1811.

[4] D. Casalino, A. Hazir, and A. Mann. Turbofan broadband noise prediction using the Lattice Boltzmann method. *AIAA Journal*, 56(2):609–628, February 2018. doi: 10.2514/1.J055674.

[5] M. Shur, M. Strelets, A. Travin, T. Suzuki, and P. R. Spalart. Unsteady simulation of sound propagation in turbulent flow inside a lined duct using a broadband time-domain impedance model. In *AIAA paper 2020-2535*, June 2020. doi: 10.2514/6.2020-2535.

[6] C. K. W. Tam, H. Ju, M. G. Jones, W. R. Watson, and T. L. Parrott. A computational and experimental study of resonators in three dimensions. *J. Sound Vib.*, 329(24):5164–5193, November 2010. doi: 10.1016/j.jsv.2010.06.005.

[7] Q. Zhang and D. J. Bodony. Numerical investigation of a honeycomb liner grazed by laminar and turbulent boundary layers. *J. Fluid Mech.*, 792:936–980, April 2016. doi: 10.1017/jfm.2016.79.

[8] L. J. Sivian. Acoustic Impedance of Small Orifices. *J. Acoust. Soc*, 7(2):94–101, 1935.

[9] U. Ingård and H. Ising. Acoustic Nonlinearity of an Orifice. *J. Acoust. Soc. Am.*, 42(1):6–17, July 1967. doi: 10.1121/1.1910576.

[10] S. Wilkinson. Influence of wall permeability on turbulent boundary-layer properties. In *AIAA paper 1983-294*, January 1983. doi: 10.2514/6.1983-294.

[11] B. M. Howerton and M. G. Jones. Acoustic liner drag: a parametric study of conventional configurations. In *AIAA paper 2015-2230*, 2015. doi: 10.2514/6.2015-2230.

[12] C. Jasinski and T. Corke. Mechanism for increased viscous drag over porous sheet acoustic liners. *AIAA Journal*, 58(8):3393–3404, August 2020. doi: 10.2514/1.J059039.

[13] J. Nikuradse. Strömungsgesetze in rauhen Rohren. *VDI-Forschungsheft*, 361, 1933.

[14] Cyril Frank Colebrook. Turbulent flow in pipes, with particular reference to the transition region between the smooth and rough pipe laws. *J. Inst. Civ. Eng.*, 12(8): 393–422, 1939.

[15] Lewis F Moody. Friction factors for pipe flow. *Tran. ASME*, 66(8):671–678, 1944.

[16] P. Orlandi, S. Leonardi, and R. A. Antonia. Turbulent channel flow with either transverse or longitudinal roughness elements on one wall. *J. Fluid Mech.*, 561: 279–305, August 2006. doi: 10.1017/S0022112006000723.

[17] Mauro De Marchis and E Napoli. Effects of irregular two-dimensional and three-dimensional surface roughness in turbulent channel flows. *Int. J. Heat Fluid Flow*, 36: 7–17, 2012.

[18] H. Choi, P. Moin, and J. Kim. Direct numerical simulation of turbulent flow over riblets. *J. Fluid Mech.*, 255:503–539, October 1993. doi: 10.1017/S0022112093002575.

[19] M. MacDonald, A. Ooi, R. García-Mayoral, N. Hutchins, and D. Chung. Direct numerical simulation of high aspect ratio spanwise-aligned bars. *J. Fluid Mech.*, 843: 126–155, May 2018. doi: 10.1017/jfm.2018.150.

[20] S. Leonardi, P. Orlandi, and R. A. Antonia. Properties of d- and k-type roughness in a turbulent channel flow. *Phys. Fluids*, 19(12):125101, December 2007. doi: 10.1063/1.2821908.

[21] C. Manes, D. Poggi, and L. Ridolfi. Turbulent boundary layers over permeable walls: scaling and near-wall structure. *J. Fluid Mech.*, 687:141–170, November 2011. doi: 10.1017/jfm.2011.329.

[22] D. Modesti, S. Endrikat, N. Hutchins, and D. Chung. Dispersive stresses in turbulent flow over riblets. *J. Fluid Mech.*, 917:A55, 2021. doi: 10.1017/jfm.2021.310.

[23] Kwing-So Choi. Near-wall structure of a turbulent boundary layer with riblets. *J. Fluid Mech.*, 208:417–458, 1989. doi: 10.1017/S0022112089002892.

[24] J. Jiménez, M. Uhlmann, A. Pinelli, and G. Kawahara. Turbulent shear flow over active and passive porous surfaces. *J. Fluid Mech.*, 442:89–117, September 2001. doi: 10.1017/S0022112001004888.

[25] Karen A. Flack and Michael P. Schultz. Review of Hydraulic Roughness Scales in the Fully Rough Regime. *J. Fluids Eng.*, 132(4):041203, 04 2010. doi: 10.1115/1.4001492.

[26] Ricardo Garcia-Mayoral and Javier Jiménez. Hydrodynamic stability and breakdown of the viscous regime over riblets. *J. Fluid Mech.*, 678:317–347, 2011.

[27] Yun Kyung Choi, Hyeon Gyu Hwang, Young Mo Lee, and Jae Hwa Lee. Effects of the roughness height in turbulent boundary layers over rod-and cuboid-roughened walls. *Int. J. Heat Fluid Flow*, 85:108644, 2020.

[28] E.M. Laws and A.K. Ouazzane. A further investigation into flow conditioner design yielding compact installations for orifice plate flow metering. *Flow Meas. Instrum.*, 6 (3):187–199, 1995. doi: 10.1016/0955-5986(95)00007-9.

[29] C. F. Kutscher. Heat Exchange Effectiveness and Pressure Drop for Air Flow Through Perforated Plates With and Without Crosswind. *J. Heat Transf.*, 116(2):391–399, 05 1994. doi: 10.1115/1.2911411.

[30] Haiqiao Wei, Dongzhi Gao, Lei Zhou, Dengquan Feng, and Rui Chen. Different combustion modes caused by flame-shock interactions in a confined chamber with a perforated plate. *Combust. Flame*, 178:277–285, 2017. doi: 10.1016/j.combustflame.2017.01.011.

[31] Alejandro Rubio Carpio, Francesco Avallone, Daniele Ragni, Mirjam Snellen, and Sybrand van der Zwaag. Mechanisms of broadband noise generation on metal foam edges. *Phys. Fluids*, 31(10):105110, 2019. doi: 10.1063/1.5121248.

[32] D. Casalino, A. Hazir, and A. Mann. Turbofan broadband noise prediction using the lattice Boltzmann method. *AIAA J.*, 56(2):609–628, 2018.

[33] M. Shur, M. Strelets, A. Travin, T. Suzuki, and P. Spalart. Unsteady simulations of sound propagation in turbulent flow inside a lined duct. *AIAA J.*, 59(8):3054–3070, 2021.

[34] Christoph Efstathiou and Mitul Luhar. Mean turbulence statistics in boundary layers over high-porosity foams. *J. Fluid Mech.*, 841:351–379, 2018. doi: 10.1017/jfm.2018.57.

[35] M. E. Rosti, L. Brandt, and A. Pinelli. Turbulent channel flow over an anisotropic porous wall - Drag increase and reduction. *J. Fluid Mech.*, 842:381–394, February 2018. arXiv: 1802.00477.

[36] Qingxiang Li, Ming Pan, Quan Zhou, and Yuhong Dong. Turbulent drag modification in open channel flow over an anisotropic porous wall. *Physics of Fluids*, 32(1):015117, January 2020. doi: 10.1063/1.5130647.

[37] Y. Kuwata and K. Suga. Direct numerical simulation of turbulence over anisotropic porous media. *J. Fluid Mech.*, 831:41–71, November 2017. doi: 10.1017/jfm.2017.619.

[38] Garazi Gómez-de Segura and Ricardo García-Mayoral. Turbulent drag reduction by anisotropic permeable substrates - analysis and direct numerical simulations. *J. Fluid Mech.*, 875:124–172, September 2019. doi: 10.1017/jfm.2019.482. arXiv: 1902.08554.

[39] W. P. Breugem, B. J. Boersma, and R. E. Uittenbogaard. The influence of wall permeability on turbulent channel flow. *J. Fluid Mech.*, 562:35–72, September 2006. doi: 10.1017/S0022112006000887.

[40] L. B. Esteban, E. Rodríguez-López, M. A. Ferreira, and B. Ganapathisubramani. Mean flow of turbulent boundary layers over porous substrates. *Phys. Rev. Fluids*, 7:094603, Sep 2022. doi: 10.1103/PhysRevFluids.7.094603.

[41] C. Manes, D. Pokrajac, I. McEwan, and V. Nikora. Turbulence structure of open channel flows over permeable and impermeable beds: A comparative study. *Phys. Fluids*, 21(12):125109, December 2009. doi: 10.1063/1.3276292.

[42] William P Elliott. The growth of the atmospheric internal boundary layer. *Trans. Am. Geophys. Union*, 39(6):1048–1054, 1958.

[43] H Cheng and Ian P Castro. Near-wall flow development after a step change in surface roughness. *Boundary-Layer Meteorol.*, 105:411–432, 2002.

[44] Amirreza Rouhi, Daniel Chung, and Nicholas Hutchins. Direct numerical simulation of open-channel flow over smooth-to-rough and rough-to-smooth step changes. *J. Fluid Mech.*, 866:450–486, 2019. doi: 10.1017/jfm.2019.84.

[45] Vladislav Efros and Per-Åge Krogstad. Development of a turbulent boundary layer after a step from smooth to rough surface. *Exp. fluids*, 51:1563–1575, 2011.

[46] F. Avallone, P. Manjunath, D. Ragni, and D. Casalino. Lattice-Boltzmann Very large eddy simulation of a multi-orifice acoustic liner with turbulent grazing flow. In *AIAA paper 2019-2542*, May 2019. doi: 10.2514/6.2019-2542.

[47] P. Tanner, J. Gorman, and R. Sparrow. Flow–pressure drop characteristics of perforated plates. *Int. J. Numer. Methods Heat Fluid Flow*, 29(11):4310–4333, November 2019. doi: 10.1108/HFF-01-2019-0065.

[48] Y. Bae and Y. I. Kim. Numerical modeling of anisotropic drag for a perforated plate with cylindrical holes. *Chem. Eng. Sci.*, 149:78–87, July 2016. doi: 10.1016/j.ces.2016.04.036.

[49] Seong-Hyun Lee and Jeong-Guon Ih. Empirical model of the acoustic impedance of a circular orifice in grazing mean flow. *J. Acoust. Soc. Am.*, 114(1):98–113, July 2003. doi: 10.1121/1.1581280.

[50] C. Scalo, J. Bodart, and S. K. Lele. Compressible turbulent channel flow with impedance boundary conditions. *Phys. Fluids*, 27(3):035107, March 2015. doi: 10.1063/1.4914099.

[51] H. Shahzad, S. Hickel, and D. Modesti. Permeability and turbulence over perforated plates. *Flow. Turbul. Combust.*, 109(4):1241–1254, 2022. doi: 10.1007/s10494-022-00337-7.

[52] M. Jones, W. R. Watson, T. Parrott, and C. Smith. Design and evaluation of modifications to the nasa langley flow impedance tube. In *AIAA paper 2004-2837*, May 2004. doi: 10.2514/6.2004-2837.

[53] B. M. Howerton and M. G. Jones. Acoustic liner drag: measurements on novel facesheet perforate geometries. In *AIAA paper 2016-2979*, May 2016. doi: 10.2514/6.2016-2979.

[54] B. M. Howerton and M. G. Jones. A conventional liner acoustic/drag interaction benchmark database. In *AIAA paper 2017-4190*, June 2017. doi: 10.2514/6.2017-4190.

[55] J. Gustavsson, Y. Zhang, L. N. Cattafesta, and J. R. Kreitzman. Acoustic liner drag measurements. In *AIAA paper 2019-2683*, 2019. doi: 10.2514/6.2019-2683.c1.

[56] Q. Zhang and D. J. Bodony. Numerical simulation of two-dimensional acoustic liners with high-speed grazing flow. *AIAA Journal*, 49(2):365–382, February 2011. doi: 10.2514/1.J050597.

[57] M. G. Jones, W. R. Watson, M. B. Tracy, and T. L. Parrott. Comparison of two waveguide methods for educing liner impedance in grazing flow. *AIAA Journal*, 42 (2):232–240, February 2004. doi: 10.2514/1.9092.

[58] C. K. W. Tam and L. Auriault. Time-domain impedance boundary conditions for computational aeroacoustics. *AIAA Journal*, 34(5):917–923, May 1996. doi: 10.2514/3.13168.

[59] S. Olivetti, R. D. Sandberg, and B. J. Tester. Direct numerical simulation of turbulent flow with an impedance condition. *J. Sound Vib.*, 344:28–37, May 2015. doi: 10.1016/j.jsv.2015.01.039.

[60] R. Sebastian, D. Marx, and V. Fortuné. Numerical simulation of a turbulent channel flow with an acoustic liner. *J. Sound Vib.*, 456:306–330, September 2019. doi: 10.1016/j.jsv.2019.05.020.

[61] K. Y. Fung, H. Ju, and B. Tallapragada. Impedance and its time-domain extensions. *AIAA Journal*, 38(1):30–38, January 2000. doi: 10.2514/2.950.

[62] K. Y. Fung and H. Ju. Time-domain impedance boundary conditions for computational acoustics and aeroacoustics. *Int. J. Comput. Fluid Dyn.*, 18(6):503–511, August 2004. doi: 10.1080/10618560410001673515.

[63] C. K. W Tam, N. N. Pastouchenko, M. G. Jones, and W. R. Watson. Experimental validation of numerical simulations for an acoustic liner in grazing flow: Self-noise and added drag. *J. Sound Vib.*, 333(13):2831–2854, June 2014. doi: 10.1016/j.jsv.2014.02.019.

[64] I E Idelchik. *Handbook of hydraulic resistance: Second edition.* CRC, Boca Raton, FL., 1994.

[65] Werner Kast, Hermann Nirschl, Edward S. Gaddis, Karl-Ernst Wirth, and Johann Stichlmair. *L1 Pressure Drop in Single Phase Flow.* Springer Berlin Heidelberg, Berlin, Heidelberg, 2010. doi: 10.1007/978-3-540-77877-6_70.

[66] Stefano Malavasi, Gianandrea Messa, Umberto Fratino, and Alessandro Pagano. On the pressure losses through perforated plates. *Flow Meas. Instrum.*, 28:57–66, 2012. doi: 10.1016/j.flowmeasinst.2012.07.006.

[67] D.S. Miller. *Internal Flow Systems*. BHRA (Information Services), Cranfield, Bedford, 1990.

[68] G. J. Holt, D. Maynes, and J. Blotter. Cavitation at Sharp Edge Multi-Hole Baffle Plates. ASME IMECE, pages 401–410, 11 2011. doi: 10.1115/IMECE2011-64203.

[69] H. Shahzad, S. Hickel, and D. Modesti. Turbulence and added drag over acoustic liners. *J. Fluid Mech.*, 965:A10, 2023. doi: 10.1017/jfm.2023.397.

[70] M. Bernardini, D. Modesti, F. Salvadore, and S. Pirozzoli. STREAmS: a high-fidelity accelerated solver for direct numerical simulation of compressible turbulent flows. *Comput. Phys. Commun.*, 263:107906, 2021.

[71] S. Pirozzoli. Generalized conservative approximations of split convective derivative operators. *J. Comput. Phys.*, 229(19):7180–7190, 2010.

[72] Sergio Pirozzoli and Matteo Bernardini. Direct Numerical Simulation Database for Impinging Shock Wave/Turbulent Boundary-Layer Interaction. *AIAA Journal*, 49(6): 1307–1312, June 2011. doi: 10.2514/1.J050901.

[73] P. R. Spalart, R. D. Moser, and M. M. Rogers. Spectral methods for the Navier-Stokes equations with one infinite and two periodic directions. *J. Comput. Phys.*, 96(2): 297–324, October 1991. doi: 10.1016/0021-9991(91)90238-G.

[74] Antony J Musker. Explicit expression for the smooth wall velocity distribution in a turbulent boundary layer. *AIAA Journal*, 17(6):655–657, 1979.

[75] You-Sheng Zhang, Wei-Tao Bi, Fazle Hussain, and Zhen-Su She. A generalized reynolds analogy for compressible wall-bounded turbulent flows. *J. Fluid Mech.*, 739: 392–420, 2014. doi: 10.1017/jfm.2013.620.

[76] S. Pirozzoli, M. Bernardini, and F. Grasso. Direct numerical simulation of transonic shock/boundary layer interaction under conditions of incipient separation. *J. Fluid Mech.*, 657:361–393, August 2010. doi: 10.1017/S0022112010001710.

[77] Thomas S. Lund, Xiaohua Wu, and Kyle D. Squires. Generation of turbulent inflow data for spatially-developing boundary layer simulations. *J. Comput. Phys.*, 140(2): 233–258, 1998. doi: 10.1006/jcph.1998.5882.

[78] Sergio Pirozzoli and Tim Colonius. Generalized characteristic relaxation boundary conditions for unsteady compressible flow simulations. *J. Comput. Phys.*, 248:109–126, September 2013. doi: 10.1016/j.jcp.2013.04.021.

[79] T.J Poinsot and S.K Lelef. Boundary conditions for direct simulations of compressible viscous flows. *Journal of Computational Physics*, 101(1):104–129, 1992. doi: 10.1016/0021-9991(92)90046-2.

[80] Espen Åkervik, Luca Brandt, Dan S. Henningson, Jérôme Hœpffner, Olaf Marxen, and Philipp Schlatter. Steady solutions of the Navier-Stokes equations by selective frequency damping. *Phys. Fluids*, 18(6):068102, 06 2006. doi: 10.1063/1.2211705.

[81] Bastien E. Jordi, Colin J. Cotter, and Spencer J. Sherwin. Encapsulated formulation of the selective frequency damping method. *Phys. Fluids*, 26(3):034101, 03 2014. doi: 10.1063/1.4867482.

[82] Jordi Casacuberta, Koen J. Groot, Henry J. Tol, and Stefan Hickel. Effectivity and efficiency of selective frequency damping for the computation of unstable steady-state solutions. *J. Comput. Phys.*, 375:481–497, 2018. doi: 10.1016/j.jcp.2018.08.056.

[83] Myoungkyu Lee and Robert D. Moser. Direct numerical simulation of turbulent channel flow up to $Re_\tau \approx 5200$. *J. Fluid Mech.*, 774:395–415, 2015. doi: 10.1017/jfm.2015.268.

[84] A. Piquet, O. Roussel, and A. Hadjadj. A comparative study of Brinkman penalization and direct-forcing immersed boundary methods for compressible viscous flows. *Comput. Fluids*, 136:272–284, September 2016. doi: 10.1016/j.compfluid.2016.06.001.

[85] F. D. Vanna, F. Picano, and E. Benini. A sharp-interface immersed boundary method for moving objects in compressible viscous flows. *Comput. Fluids*, 201:104415, April 2020. doi: 10.1016/j.compfluid.2019.104415.

[86] The CGAL Project. *CGAL User and Reference Manual*. CGAL Editorial Board, 5.4 edition, 2022.

[87] D. Modesti, S. Sathyanarayana, F. Salvadore, and M. Bernardini. Direct numerical simulation of supersonic turbulent flows over rough surfaces. *J. Fluid Mech.*, 942: A44, 2022.

[88] Lucas Schroeder, André M. Spillere, Lucas A. Bonomo, Andrey R. da Silva, Francesco Avallone, and Julio A. Cordioli. Numerical investigation of acoustic liners experimental techniques using a lattice-boltzmann solver. In *AIAA paper 2021-2144*, 2021. doi: 10.2514/6.2021-2144.

[89] A. Lozano-Durán and J. Jiménez. Effect of the computational domain on direct simulations of turbulent channels up to re τ= 4200. *Phys. Fluids*, 26(1):011702, 2014.

[90] Daniel Chung, Leon Chan, Michael MacDonald, Nicholas Hutchins, and Andrew Ooi. A fast direct numerical simulation method for characterising hydraulic roughness. *J. Fluid Mech.*, 773:418–431, 2015.

[91] M. MacDonald, D. Chung, N. Hutchins, L. Chan, A. Ooi, and R. García-Mayoral. The minimal-span channel for rough-wall turbulent flows. *J. Fluid Mech.*, 816:5–42, 2017.

[92] S. Di Giorgio, S. Leonardi, S. Pirozzoli, and P. Orlandi. On the relationship between drag and vertical velocity fluctuations in flow over riblets and liquid infused surfaces. *International Journal of Heat and Fluid Flow*, 86:108663, December 2020. doi: 10.1016/j.ijheatfluidflow.2020.108663.

[93] Jiasheng Yang, Alexander Stroh, Daniel Chung, and Pourya Forooghi. Direct numerical simulation-based characterization of pseudo-random roughness in minimal channels. *J. Fluid Mech.*, 941:A47, 2022. doi: 10.1017/jfm.2022.331.

[94] P. Orlandi and S. Leonardi. DNS of turbulent channel flows with two-and three-dimensional roughness. *J. Turbul.*, 7:N73, 2006.

[95] Y. Kuwata and K. Suga. Extensive investigation of the influence of wall permeability on turbulence. *Int. J. Heat Fluid Flow*, 80:108465, December 2019. doi: 10.1016/j.ijheatfluidflow.2019.108465.

[96] N. Abderrahaman-Elena, C. T. Fairhall, and R. García-Mayoral. Modulation of near-wall turbulence in the transitionally rough regime. *J. Fluid Mech.*, 865:1042–1071, April 2019. doi: 10.1017/jfm.2019.41.

[97] P. Orlandi and S. Leonardi. DNS of turbulent channel flows with two- and three-dimensional roughness. *Journal of Turbulence*, 7:N73, January 2006. doi: 10.1080/14685240600827526.

[98] P. S. Jackson. On the displacement height in the logarithmic velocity profile. *J. Fluid Mech.*, 111:15–25, October 1981. doi: 10.1017/S0022112081002279.

[99] J. I. Ibrahim, G. Gómez-de Segura, D. Chung, and R. García-Mayoral. The smooth-wall-like behaviour of turbulence over drag-altering surfaces: a unifying virtual-origin framework. *J. Fluid Mech.*, 915:A56, May 2021. doi: 10.1017/jfm.2021.13.

[100] D. Chung, N. Hutchins, M. P. Schultz, and K. A. Flack. Predicting the drag of rough surfaces. *Annu. Rev. Fluid Mech.*, 53(1):439–471, January 2021. doi: 10.1146/annurev-fluid-062520-115127.

[101] Y. Kuwata and K. Suga. Transport mechanism of interface turbulence over porous and rough walls. *Flow Turbulence Combust*, 97(4):1071–1093, December 2016. doi: 10.1007/s10494-016-9759-9.

[102] S. L. Lee and J. H. Yang. Modeling of Darcy-Forchheimer drag for fluid flow across a bank of circular cylinders. *Int. J. Heat Mass Transf.*, 40(13):3149–3155, September 1997. doi: 10.1016/S0017-9310(96)00347-X.

[103] M. R. Raupach, R. A. Antonia, and S. Rajagopalan. Rough-wall turbulent boundary layers. *Appl. Mech. Rev.*, 44(1):25, 1991.

[104] L. Chan, M. MacDonald, D. Chung, N. Hutchins, and A. Ooi. Secondary motion in turbulent pipe flow with three-dimensional roughness. *J. Fluid Mech.*, 854:5–33, 2018.

[105] Y. Kuwata and K. Suga. Lattice Boltzmann direct numerical simulation of interface turbulence over porous and rough walls. *Int. J. Heat Fluid Flow*, 61:145–157, October 2016. doi: 10.1016/j.ijheatfluidflow.2016.03.006.

[106] J. Yuan and U. Piomelli. Roughness effects on the Reynolds stress budgets in near-wall turbulence. *J. Fluid Mech.*, 760:R1, December 2014. doi: 10.1017/jfm.2014.608.

[107] N. Hutchins and I. Marusic. Evidence of very long meandering features in the logarithmic region of turbulent boundary layers. *J. Fluid Mech.*, 579:1–28, 2007.

[108] X. Chu, W. Wang, G. Yang, A. Terzis, R. Helmig, and B. Weigand. Transport of turbulence across permeable interface in a turbulent channel flow: interface-resolved direct numerical simulation. *Transp. Porous Med*, 136:165–189, January 2021. doi: 10.1007/s11242-020-01506-w.

[109] J. Finnigan. Turbulence in plant canopies. *Annu. Rev. Fluid Mech.*, 32(1):519–571, 2000.

[110] R. Mathis, N. Hutchins, and I. Marusic. Large-scale amplitude modulation of the small-scale structures in turbulent boundary layers. *J. Fluid Mech.*, 628:311–337, 2009.

[111] T. Kim, G. Blois, J. L. Best, and K. T. Christensen. Experimental evidence of amplitude modulation in permeable-wall turbulence. *J. Fluid Mech.*, 887:A3, March 2020. doi: 10.1017/jfm.2019.1027.

[112] S. Wu, K. T. Christensen, and C. Pantano. Modelling smooth- and transitionally rough-wall turbulent channel flow by leveraging inner–outer interactions and principal component analysis. *J. Fluid Mech.*, 863:407–453, March 2019. doi: 10.1017/jfm.2018.899.

[113] H. G. Weller, G. Tabor, H. Jasak, and C. Fureby. A tensorial approach to computational continuum mechanics using object-oriented techniques. *Comput. Phys.*, 12(6):620–631, 1998. doi: 10.1063/1.168744.

[114] Matteo Bernardini, Davide Modesti, Francesco Salvadore, Srikanth Sathyanarayana, Giacomo Della Posta, and Sergio Pirozzoli. Streams-2.0: Supersonic turbulent accelerated navier-stokes solver version 2.0. *Comput. Phys. Commun.*, 285:108644, 2023. doi: 10.1016/j.cpc.2022.108644.

[115] S. Endrikat, D. Modesti, R. García-Mayoral, N. Hutchins, and D. Chung. Influence of riblet shapes on the occurrence of kelvin–helmholtz rollers. *J. Fluid Mech.*, 913:A37, 2021. doi: 10.1017/jfm.2021.2.

[116] JWS Baron Rayleigh. On the theory of resonance. *Philos. Trans. R. Soc. A*, 161:77–118, 1871. doi: 10.1098/rstl.1871.0006.

[117] U. Ingård. On the Theory and Design of Acoustic Resonators. *J. Acoust. Soc. Am.*, 25 (6):1037–1061, November 1953. doi: 10.1121/1.1907235.

[118] AW Guess. Calculation of perforated plate liner parameters from specified acoustic resistance and reactance. *J. Sound Vib.*, 40(1):119–137, 1975. doi: 10.1016/S0022-460X(75)80234-3.

[119] Q. Zhang and D. J. Bodony. Numerical investigation and modelling of acoustically excited flow through a circular orifice backed by a hexagonal cavity. *J. Fluid Mech.*, 693:367–401, February 2012. doi: 10.1017/jfm.2011.537.

[120] James Cardillo, Yi Chen, Guillermo Araya, Jensen Newman, Kenneth Jansen, and Luciano Castillo. Dns of a turbulent boundary layer with surface roughness. *J. Fluid Mech.*, 729:603–637, 2013. doi: 10.1017/jfm.2013.326.

[121] Xiaofei Liu, Hui Zhao, Kun Luo, and Jianren Fan. Direct numerical simulation of turbulent boundary layer over hemispherical rough walls. *Int. J. Multiph. Flow*, 83: 128–141, 2016. doi: 10.1016/j.ijmultiphaseflow.2016.03.009.

[122] A. Ceci, A. Palumbo, J. Larsson, and S. Pirozzoli. Numerical tripping of high-speed turbulent boundary layers. *Theor. and Comput. Fluid Dyn.*, 36(6):865–886, 2022. doi: 10.1007/s00162-022-00623-0.

[123] Ricardo Vinuesa, Cezary Prus, Philipp Schlatter, and Hassan M Nagib. Convergence of numerical simulations of turbulent wall-bounded flows and mean cross-flow structure of rectangular ducts. *Meccanica*, 51:3025–3042, 2016. doi: 10.1007/s11012-016-0558-0.

[124] Leandro Rego, Francesco Avallone, Daniele Ragni, Damiano Casalino, and Hervé Denayer. Acoustic liners for jet-installation noise reduction. *J. Sound Vib.*, 537: 117189, 2022. doi: 10.1016/j.jsv.2022.117189.

[125] Lijun Li, Yiran Liu, Fan Zhang, and Zhenyong Sun. Several explanations on the theoretical formula of helmholtz resonator. *Adv. Eng. Softw.*, 114:361–371, 2017. doi: 10.1016/j.advengsoft.2017.08.004.

[126] L.M. Pereira, L.A Bonomo, N.T. Quintino, da A.R. Silva, J. A. Cordioli, and F. Avallone. Validation of high-fidelity numerical simulations of acoustic liners under grazing flow. *AIAA Paper*, pages 2023–3503, 2023. doi: 10.2514/6.2023-3503.

[127] Gwénaël Gabard. Boundary layer effects on liners for aircraft engines. *J. Sound Vib.*, 381:30–47, 2016. doi: 10.1016/j.jsv.2016.06.032.

[128] Kazuhiko Suga, Yuka Nakagawa, and Masayuki Kaneda. Spanwise turbulence structure over permeable walls. *J. Fluid Mech.*, 822:186–201, July 2017. doi: 10.1017/jfm.2017.278.

[129] S. Endrikat, D. Modesti, R. García-Mayoral, N. Hutchins, and D. Chung. Influence of riblet shapes on the occurrence of Kelvin–Helmholtz rollers. *J. Fluid Mech.*, 913:A37, 2021. doi: 10.1017/jfm.2021.2.

[130] H. Schlichting. *Boundary layer theory*, volume 121. Springer, 1968.

[131] Georg Eitel-Amor, Ramis Örlü, and Philipp Schlatter. Simulation and validation of a spatially evolving turbulent boundary layer up to re_θ=8300. *Int. J. Heat Fluid Flow*, 47:57–69, 2014. doi: 10.1016/j.ijheatfluidflow.2014.02.006.

[132] Hua Ding, Nengyin Wang, Sheng Qiu, Sibo Huang, Zhiling Zhou, Chengcheng Zhou, Bin Jia, and Yong Li. Broadband acoustic meta-liner with metal foam approaching causality-governed minimal thickness. *Int. J. Mech. Sci.*, 232:107601, 2022.

[133] Michael Jones, Tony Parrott, Daniel Sutliff, and Christopher Hughes. Assessment of soft vane and metal foam engine noise reduction concepts. In *AIAA paper 2009-3142*, page 3142, 2009.

[134] M. E. Rosti, L. Cortelezzi, and M. Quadrio. Direct numerical simulation of turbulent channel flow over porous walls. *J. Fluid Mech.*, 784:396–442, December 2015. doi: 10.1017/jfm.2015.566.